AN ALTERNATE MECHANISM FOR CREATING FUNCTIONAL SUB-MICROMETER SUPERCONDUCTING QUANTUM INTERFERENCE DEVICES

A Dissertation

by

ARLENE CELESTE FORD

Submitted to the Office of Graduate Studies of
Texas A&M University
in partial fulfillment of the requirements for the degree of

DOCTOR OF PHILOSOPHY

May 2010

Major Subject: Physics

AN ALTERNATE MECHANISM FOR CREATING FUNCTIONAL SUB-MICROMETER SUPERCONDUCTING QUANTUM INTERFERENCE DEVICES

A Dissertation

by

ARLENE CELESTE FORD

Submitted to the Office of Graduate Studies of
Texas A&M University
in partial fulfillment of the requirements for the degree of

DOCTOR OF PHILOSOPHY

Approved by:

Chair of Committee,	Winfried Teizer
Committee Members,	Joseph H. Ross, Jr.
	Glenn Agnolet
	Yue Kuo
Head of Department,	Edward S. Fry

May 2010

Major Subject: Physics

ABSTRACT

An Alternate Mechanism for Creating Functional
Sub-Micrometer Superconducting Quantum Interference Devices. (May 2010)
Arlene Celeste Ford, B.S., Midwestern State University;
M.S., Texas A&M University
Chair of Advisory Committee: Dr. Winfried Teizer

Localized detection of very small regularly placed magnetic systems, such as an array of tiny magnetic islands, has been of great interest to scientists for years because of their applications to data storage media. One such detection device, the micro-SQUID (microscopic superconducting quantum interference device), can be used to detect very small changes in magnetic flux. Most low T_c micro-SQUIDs (LTS) are made from aluminum or niobium. While an aluminum SQUID is relatively easy to fabricate, one often needs a low temperature system than can be cooled to 1K to see the critical current phenomenon. As a contrast, niobium which has a higher critical temperature, and a more complicated fabrication procedure due to its need to be fabricated in a extremely clean environment to achieve a reproducible value for its critical temperature, which is about 9.25 K. Such a SQUID will only need to be immersed in a helium bath for the superconducting transition to occur. Alternatives such as tin, indium and lead, which are soft superconductors, do not wet a silicon/silicon dioxide surface as easily as niobium and aluminum. However, the benefits of a successful implementation of these soft superconductors as SQUIDs could greatly outweigh their drawbacks in terms of reducing the amount of time necessary for fabrication and measurement as well as the low temperature system requirements.

In this dissertation, the successful development of functional square and rect-

angular tin sub-microscopic SQUIDs for use as magnetometers is reported. The application of a germanium pre-nucleation layer, as a means of creating a electrically continuous path, offers an alternative to micro-SQUIDs fabricated under more involved methods as used in niobium SQUIDs. An image of the device surface showed that the roughness consisted of defects such as holes which gives rise to critical current fluctuations and vortex pinning due to magnetic hysteresis. However, the oscillations observed from several of these devices, were found to be smooth with sharp edges but with a diminished period of oscillation. Several devices were tested and their fabrication, measurement and characterization methods are described.

Another important study incorporated in our analysis of these tin germanium SQUID included its reduction from the micrometer regime to its lowest functional geometry. Moreover, to avoid the operational breakdown of a SQUID due to magnetic hysteresis and a diminution in sensitivity, the condition $2I_cL \lessapprox \Phi_0$ had to be satisfied, where I_c is the critical current and L is the inductance of the device and Φ_0 is one flux quantum $\Phi_0 = \frac{h}{2e} = 20.86$ gauss μm^2. Experimental measurements showed that all of these devices had magnetic hysteresis and operated outside of this constraint. In addition, several devices exhibited extremely high critical currents when the temperature was lowered a few milli-Kelvin past the transition temperature. Furthermore, unstable regions were present in the minima of the modulations indicating that additional quantum effects were incorporated into the device as a result of screening currents and magnetic hysteresis behavior.

To my Parents, Ethlyn and Keith.

ACKNOWLEDGMENTS

I would like to thank my advisor, Dr. Winfried Teizer, for the freedom to explore my research interests here at Texas A&M University. I would also like to thank my committee members, Dr. Glenn Agnolet, Dr. Joseph H. Ross, Jr and Dr. Yue Kuo for serving on my committee. Special thanks go to Dr. Daya Rathnayaka, Dr. Kyongwan Kim and Dr. Venkateshwarlu Goruganti for having many troubleshooting discussions with me.

I would also like to acknowledge my current and former lab mates for helping with all the heavy lifting and lending a spare hand with my low temperature experiments when necessary, Tracey Wellington, Dr. Raj Srivastava, Dr. Joel Means, Dr. John Noel, Dr. Dongmin Seo, Dr. Luohan Peng, Dr. Huachun Xu, Bing Bai, Kyongjin Lee, Sung Oh Woo, Jinseon Park, Kelley Reaves and Esma. Also, I would like to thank my family, both in the United States and in Antigua, for all their love and support.

TABLE OF CONTENTS

CHAPTER Page

LIST OF TABLES

LIST OF FIGURES

FIGURE Page

FIGURE Page

FIGURE Page

FIGURE Page

FIGURE Page

FIGURE Page

FIGURE Page

FIGURE Page

FIGURE Page

FIGURE Page

FIGURE Page

CHAPTER I

INTRODUCTION

A. A History of SQUIDs

Superconducting quantum interference devices (SQUIDs) has been one of the most well known and widely used applications of superconductivity. The most attractive feature of a micro-SQUID is its ability to detect extremely weak magnetic fields, which makes it an excellent tool to aid in the study of nano-magnetic systems. Micro-SQUIDs can be used as magnetometers, gradiometers, susceptometers, current comparators, quantum bits, flux meters, rf amplifiers, flux transistors, scanning microscopes and voltmeters provided that the appropriate input circuit configurations are used to connect to the SQUID's input signal. Other uses for these micro-sensors include, making localized measurements in small spin systems and investigating the magnetic response of mesoscopic structures [1]. The first SQUIDs were developed by R. Jaklevic, A. Silver, J. Lambe, J. Mercereau, J. Zimmerman, and M. Nisenoff [2, 3, 4, 5, 6, 7] using the theories of F. London [8], B.D. Josephson [9] and the BCS Theory trio, J. Bardeen, L. Cooper and J.R. Schrieffer [10] who created the first comprehensive understanding of superconductivity. London's work predicted that the flux through a superconducting ring would be quantized in units of $\frac{h}{2e}$ when a transport current was circulating through it and Josephson's work showed that electrons would tunnel through a barrier connecting two superconductors leading to events we now call the ac and dc Josephson effects.

This dissertation is written in the *Journal of Applied Physics* format.

There are two types of SQUIDs, the dc SQUID and the rf SQUID. The dc SQUID was created by Jaklevic, Silver and Lambe [2] at Ford Research Labs, and consists of two Josephson junctions (bridges) connected in parallel within a superconducting loop. The rf SQUID, which consists of a single Josephson junction in a superconducting loop and operated with a radio frequency flux bias, was created by Zimmerman, Silver, Mercereau and Nisenoff [4, 3] also at the Ford Research Labs. The construction of both the dc and rf SQUIDs came quickly after J. Rowell and P. Anderson [11] successfully created the first working Josephson junction at Bell Labs and the flux quantization was experimentally observed in superconducting cylinders and rings by B. Deaver, W. Fairbank, R. Doll and M. Nabauer [12, 13].

Not long after the fabrication of SQUIDs at the Ford Research Labs, optimization studies on both low T_c and high T_c SQUIDs were conducted at the University of California at Berkley by J. Clarke, M. Ketchen, F. Wellstood and J. Koch [14, 15, 16]. The studies made by Clarke's group included investigations into the SQUID performance in the presence of noise and the SQUID resolution with an ac flux modulation. Ketchen and Koch then went on to develop the micro-susceptometer SQUID configuration with J. R. Kirthley at the IBM T. J. Watson Research Center which made great advances to the understanding of scanning SQUID sensor technology.

While experiments were undertaken to improve the device performance at Berkeley, there was growing interest in studying systems within the microscopic regime. This became possible with the development of several thin film deposition techniques and soon after miniaturized SQUIDs were developed from these processes to measure microscopic particles. Today, with the improvements made to these fabrication procedures, micro-SQUIDs have been able to measure particles well into the nanometer regime and their use has been expanded to areas such as medicine, cosmology and geophysics.

B. Overview of Micro-SQUIDs

A typical micro-SQUID device, which was first introduced by Chapelier, et. al. [17] and utilized by Wernsdorfer and Hasselbach [18, 1], had a superconducting loop that was joined by two constrictions (Dayem Bridges). The outer length and width of the loop were between 1.3 μm and 1.5 μm and the inner area of the hole was 1 μm by 1 μm. The junction width was approximately 50 nm, the junction length approximately 300 nm and the thickness of the device between 20 nm and 50 nm (see Fig. 1). The micro-SQUID exhibited periodic oscillations of its critical current which was modulated by a magnetic flux inside the loop. Moreover, the period of these oscillations was one flux quantum $\Phi_0 = \frac{h}{2e} = 20.86$ gauss μm^2. These flux sensors also exhibited non-linear current-voltage characteristics due to the generation of heat induced by the energy dissipated in the weak links and loop.

Other micro-SQUID designs such as the hot phonon controlled junctions micro-SQUIDs [19] and the resistively shunted nano-SQUID [20] offer some insights as to the complications that occur with the noise sensitivity and characteristic lengths of reduced geometry devices. During the measurements with the hot phonon controlled junctions, the devices (made from niobium) were observed to be extremely sensitive to external high frequency noise and effects due to flux pinning and de-pinning within the superconducting film. The flux pinning effects were found to occur soon after the device was inserted into liquid helium. The SQUID was found to be stable and the trapped flux in the superconducting film was removed after sweeping the current through the device a few times. In the case of the resistively shunted miniature SQUID, which was also made from niobium (Nb), the flux noise of the device was $5 - 7 \times 10^{-6}\Phi_0/Hz^{1/2}$ at 1 Hz and 4.2 K. This was much lower than the flux noise reported by Wernsdorfer et al [18], which was $1 \times 10^{-4}\Phi_0/Hz^{1/2}$ or Hasselbach et al

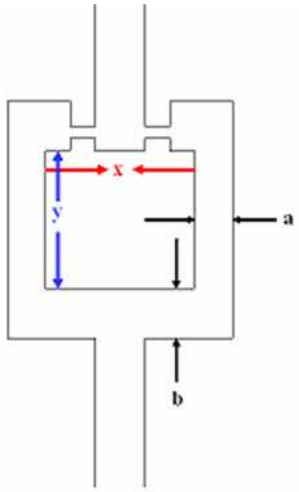

Fig. 1. An Outline of a Micro-SQUID Device Showing Its Critical Dimensions. The Typical Outer Length and Width of the Loop Are between 1.4 μm and 1.5 μm with a = b = 0.4 μm - 0.5 μm and the Inner Area of the Hole Was x = 1 μm by y = 1 μm. The Typical Junction Width Was Approximately 50 nm, the Typical Junction Length Was Approximately 300 nm and the Typical Thickness of the Device between 30 nm and 40 nm.

[21] which had a flux noise of $3.7 \times 10^{-5}\Phi_0/Hz^{1/2}$ for their aluminum micro-SQUIDs. Therefore by incorporating an amplified signal, screen rooms and vibration isolation mechanisms, better results when recording data can be achieved.

C. Motivation

Research is underway to increase the data density of storage media which are currently made from continuous films of magnetic material. One method proposed to

increase the data density is to create disks of tightly packed isolated magnetic islands (magnetic nanoparticles) instead of using a continuous film [22]. Magnetic sensors such as Hall probes (sensitivity in the mT range), flux gate sensors (sensitivity in the nT range) and the SQUID (sensitivity in the fT range), which are commonly used for detection of small magnetic fields, are some of the ways in which these tiny changes in magnetic fields could be measured and recorded [23]. However, a major drawback to using these densely packed magnetic islands would be that the thermal energies surrounding the system would overwhelm lower magnetic energies associated with each island cause some regions to lose their magnetism [22].

It has been shown that for a specific geometry the best combination of field sensitivity and spatial resolution occurs when the sample to sensor distance is at a minimum, more specifically, when the sample is overlapping a junction [24]. However, if this is not possible, the SQUID sensor measures the integrated magnetic flux over the sensing area and as a result scales as $\frac{1}{a^2}$, where a is the diameter of the sensing area, which suggest that it can measure small systems near to it as well. The source of the magnetic system determines the signal fall off rate. For example, a current carrying wire would scale as $\frac{1}{r}$ and a magnetic dipole would scale as $\frac{1}{r^3}$, where r is the distance to the source. Thus, the best combination of field sensitivity and spatial resolution would occur at $r = a$. In addition to this distribution, it was also shown that the signal to noise ratio also scales as $\frac{1}{a}$ [25]. Therefore, alternative strategies may have to be employed to map out these small systems if they are masked by noise.

By reducing a SQUID's dimensions to its smallest operational geometry, one could produce arrays of closely packed sensors under the isolated magnetic islands creating localized detection systems. The ultimate goal would be to have one SQUID sensor for each island and hence detect which regions exhibit changes in their behaviors due to external effects by the change in the SQUID's response. Furthermore, the

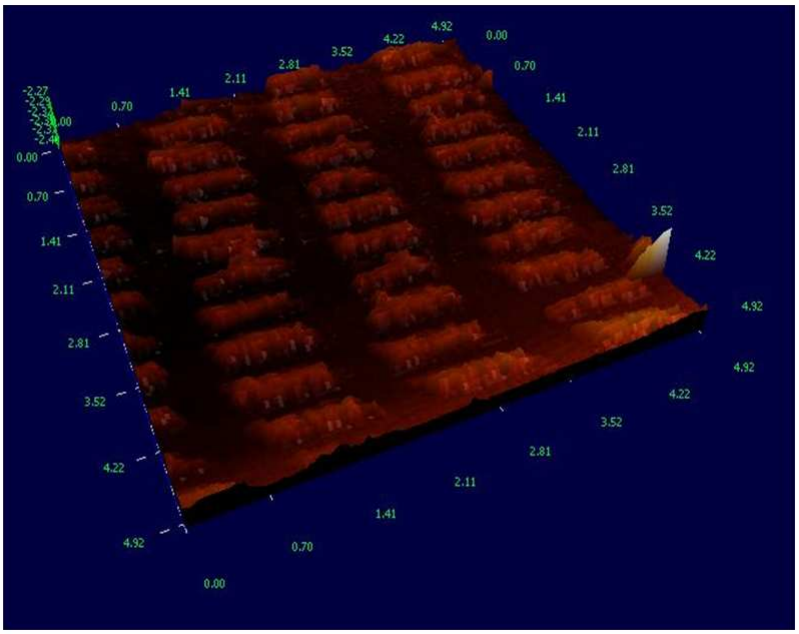

Fig. 2. A Scanning Tunneling Microscope Image of Cobalt Bromide Islands. These Islands Were Fabricated Using Electron Beam Lithography and a Subsequent Lift Off and Metalization Step. These Processes (Electron Beam Lithography, Metalization and Lift-Off) Will Be Discussed in More Detail in Chapter IV. These Islands were Approximately 100 to 200 nm Apart. Eventually These Islands Will Be Placed On Top of a System of SQUIDs for Analysis.

calibration of these miniaturized SQUID sensors to systematically record and report external disruptions and to map the spatial distributions of the nano-particles, would move us one step closer to understanding how to construct these densely packed isolated islands for optimal data storage. Configurations that have been considered for investigation of these magnetic islands (made of iron, cobalt, cobalt oxide, cobalt bromide as seen in Fig. 2 or nickel) include tightly packed arrays of different shapes (dots, triangles, stars, and squares) and sizes (below 50 nm).

D. Organization of Thesis

The remainder of this thesis is organized as follows: Chapter II briefly introduces the topic of superconductivity and its characteristic behavior, along with the importance of its associated parameters such as the coherence length and penetration depth. A brief introduction to Josephson tunnel junctions is given and the resistively and capacitively shunted junction model is described which is necessary for understanding SQUID behavior. Once the SQUIDs approach the sub-micrometer regime, their size becomes comparable to the characteristic lengths (coherence length, London penetration depth and Pearl penetration depth) of the superconducting material from which they were made [1, 26]. Recent studies also have shown that the modulation of the critical current oscillations were dependent on the size of the junctions relative to the coherence length. One particular benefit to minimizing the SQUID geometries is the improved spatial sensitivity, but a drawback would be an increased thermal noise sensitivity.

Chapter III provides and overview of the DC SQUID which is the device used to carry out the experimental measurements for this thesis. The basic operating parameters such as the bias or transport current, the voltage transfer function, the screening parameter, and magnetic hysteresis are discussed. These topics have been discussed at great length by Tinkham and Gallop. For further reading on these topics, see [27, 28].

Chapter IV gives a detailed description of the device fabrication using the electron beam lithography technique and a brief background of the scanning electron microscope system operation. In this thesis, the micro-SQUID design used by Wernsdorfer and Hasselbach [18, 21] will be employed to investigate the modulation of the critical current in the presence of a changing magnetic field as its dimensions are

reduced to the sub-micrometer(nanometer) regime. The superconducting materials used in fabrication is presented along with potential issues observed in the fabrication process. Thin film deposition of the two dimensional SQUID by a metalization and lift-off process of the superconducting material is also discussed.

Chapter V describes the experimental methods used to obtain the data for the superconducting devices. Three low temperature systems were utilized over the course of the experimental investigation of the SQUID behavior and a brief overview of each system's operation is discussed. The bias current used to generate the critical current was introduced very slowly to minimize the thermal effects on the device and to obtain measurements. An outline of the SQUID's characterization process is also described in this chapter.

Chapter VI and Chapter VII offer insights into the results obtained and observations seen throughout the experimental analysis process. The overall observations and results of preceding chapters are summarized. Some interesting observations included the SQUID's ability to carry relatively large currents before losing their superconductivity (the thermal hysteresis effect), and the presence of loosely pinned vortices in the rough superconducting film [29, 30].

Another interesting observation was the distorted interference pattern created once the SQUID elements were connected in series. This distortion was generated by the coupling effects of their induced currents. Previous experiments have shown that when SQUIDs have equal critical currents, the SQUID modulations superimpose, with their modulation periods staying the same and the amplitude of the modulated signal being enhanced [31, 32]. The problem arises when the coupling inductances of the SQUIDs are dissimilar and the resultant interference pattern becomes unpredictable. However, there is evidence that (depending on how dissimilar the critical currents) a periodic beat (pattern within a pattern) will be created. It is important to note that a

portion of the SQUID inductance is generated from the presence of induced circulating currents which masks the modulated signal when the currents in the SQUID reaches a certain threshold.

CHAPTER II

SUPERCONDUCTIVITY

Superconductivity was first discovered in 1911 by Heike Kamerlingh Onnes [33] when he observed the resistance of mercury vanish just below liquid helium temperatures [34]. More superconductors were discovered in the years that followed at various transition temperatures. In 1933, another important discovery about superconducting properties was made by Walter Meissner and Robert Ochsenfeld [35] when they discovered that applied magnetic fields are expelled from a superconductor once it enters its superconducting state [36]. Nearly two decades later, the macroscopic properties of superconductors were explained by the theories of Vitaly Ginzburg and Lev Landau [27]. Later, Alexei Abrikosov was able to show that the Ginzburg-Landau theory predicted the classification of superconductors into two groups now referred to as Type I and Type II superconductors [27, 28]. A complete macroscopic theory of superconductivity was then proposed by John Bardeen, Leon Cooper and John Schrieffer, in 1957 which was later shown to reduce to the Ginzburg-Landau theory at the transition temperature of the superconductor [37, 38]. Five years later Brian Josephson theorized that electrons could tunnel through two superconductors separated by an insulating barrier, a phenomenon now known as the Josephson effect [28]. In this chapter, the concepts of superconductivity are further discussed along with its application to SQUIDs.

A. Metals as Superconductors

The resistance in all clean metals decreases if they are cooled from room temperature (300 K) to temperatures approaching absolute zero (0 K). In some of these metals however, there is a unique temperature value above absolute zero, called

the critical temperature or the transition temperature, where the resistance of the metal falls quickly and sharply to zero, that is, the metal loses all resistance at that point. Below this critical threshold temperature the metal continues to exhibit no resistance. Metals that exhibit this characteristic are called superconductors and this critical temperature is different for each metal.

We can envision the structure of a metal to be a periodic lattice of positive ions that is surrounded by an almost free flow of electrons. These electrons exist as plane waves and propagate in the direction of the current flow. The metal has no resistance if the electron waves can pass straight through it. However, this is extremely difficult to achieve at temperatures above absolute zero (0 K), due to small displacements of the lattice structure from its equilibrium position by the thermal vibrations of the ions in it. The lattice may also contain embedded impurities (ions of other elements) and other defects which disrupt the periodicity of the lattice.

Both the thermal vibrations and the defects will interfere with the electron wave's ability to pass straight through the lattice. As a result, the electron waves would be scattered. This scattering of the electrons causes the metal to have resistance. Therefore if we lower the temperature of the metal we can reduce the lattice vibrations which will in turn lower the resistance of the metal. In addition, if we can reduce the impurities that occur in the lattice structure we can also cause the resistance of the metal to decrease. Impurities in the lattice of a metal are not affected by temperature. The only way for the resistance of the metal to be reduced to zero is for all of the impurities to be removed. A real sample will have some impurities, since it is extremely difficult for a metal to be perfectly pure. This results in there always being some residual resistance even at absolute zero.

A superconductor loses all of its resistance at the transition temperature because the electrons are no longer scattered by the lattice vibrations or the defects

of the lattice. At temperatures below the critical temperature the electrons in the superconductor become coupled (paired with each other) because the force of attraction between them will exceed their force of repulsion. The coupled state is called a Cooper pair and is an indirect interaction of the two electrons, where one of the electrons interacts with the lattice and the lattice in turn interacts with the other electron. This interaction occurs when an electron moves through the crystal lattice of the superconductor and as it passes the surrounding positive ions in the lattice are attracted to the electron and thus move towards it, briefly deforming the lattice and thus slightly increasing the concentration of positive charge in that region.

The deformed region is then propagated through the lattice as a vibrational wave (that is emitting a phonon which is just the quantized vibration of the lattice) which attracts a second electron. This causes the two electrons to have an attractive interaction due to the emission of a phonon in the lattice. These electrons, that form the bound pair, will have opposite spins (one up and the other down) and linear momentum that is equal in magnitude but opposite in direction, so the net spin and net momentum is zero. Each Cooper pair can be seen as one particle with a mass $2m$ and charge $2e$, with a center of mass velocity. Like other particles, these Cooper pairs can be described by a single wave form. These pairs do not act independently. In fact, they act as one unit, that is, they behave like a correlated system. This system is a superposition of all the Cooper pair waves and can be treated as a single wave function. The wave function will describe the motion of all the electron pairs in the superconductor. This collective wave is known as the electron pair wave, and travels along the superconductor as a resistance-less current or super-current.

B. Theory of Josephson Junctions

This section describes the theories behind the Josephson tunnel junctions which were the typical junctions used in early DC SQUIDs, although our Josephson junctions are weak links (Dayem bridges), the discussions in this section closely relates to the behavior of the micro-SQUIDs constructed for analysis in this dissertation.

A Josephson tunnel junction consists of two superconducting electrodes connected by an insulating region through which the Cooper pair electrons tunnel from one electrode to the other. The resistively and capacitively shunted junction (RCSJ) model [28] has been used to describe many of the characteristics of tunnel junctions, such as the hysteretic current-voltage relationship. The model is made up of four basic elements, a current source, an ideal junction, a shunting resistor and a shunting capacitor which are shown in Fig. 3. The total current through the resistively and capacitively shunted junction is the sum of the current through the capacitor I_ϵ, the current through the resistor I_R and the current through the junction I_J and is given by

$$I = \frac{C\Phi_0}{\pi}\frac{d^2\gamma}{dt^2} + \frac{\Phi_0}{2\pi R}\frac{d\gamma}{dt} + I_c \sin\gamma, \tag{2.1}$$

where γ is the gauge invariant phase difference between the superconducting electrodes and I_c is the critical current of the junction. The gauge invariant is also discussed in more detail in chapter III, section B. The other parameters in equation 2.1 are defined as follows, the parallel plate capacitance C, of the junction is given by

$$C = \frac{\varepsilon A}{d} \tag{2.2}$$

with thickness d, area A and permittivity ε with the current through the capacitor

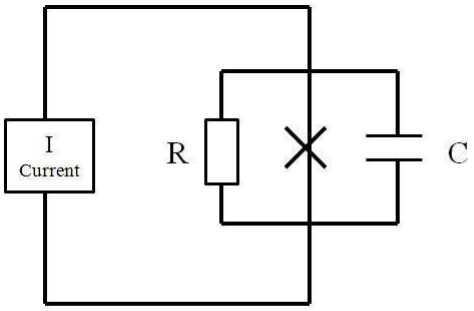

Fig. 3. A Resistively and Capacitively Shunted Junction (RCSJ) Circuit. The Circuit Has Four Basic Elements, a Current Source, Ideal Josephson Junctions, a Shunting Resistor and a Shunting Capacitor.

being

$$I_\epsilon = C\frac{dV}{dt}. \tag{2.3}$$

The ac Josephson relation shows that the voltage through the resistor is

$$V = \frac{\Phi_0}{\pi}\frac{d\gamma}{dt}, \tag{2.4}$$

where $\Phi_0 = \frac{h}{2e} = 2.0678 \times 10^{-15}\ Wb$ is the flux quantum, with the current through the resistor being

$$I_R = \frac{V}{R}. \tag{2.5}$$

In addition, the dc Josephson relation establishes the current through the junction to be

$$I_J = I_c \sin\gamma. \tag{2.6}$$

Equation 2.1 can also be represented in a dimensionless form by

$$\iota = \beta_c \ddot{\gamma} + \dot{\gamma} + \sin\gamma \tag{2.7}$$

with dimensionless parameters for the time given by

$$\tau = \frac{2\pi R I_c t}{\Phi_0} \tag{2.8}$$

and for the current being

$$\iota = \frac{I}{I_c}. \tag{2.9}$$

The parameter β_c is called the Stewart-McCumber parameter and is equal to

$$\beta_c = \frac{2\pi C R^2 I_c}{\Phi_0}. \tag{2.10}$$

It has been reported by Tinkham, Tesche and Clarke [27, 15, 14] that if the Stewart-Mccumber parameter is greater than 1 ($\beta_c > 1$), the I-V curve of an ideal resistively and capacitively shunted Josephson junction would become hysteretic, but if $\beta_c < 1$ then the I-V curve would be non-hysteretic.

When $\beta_c \ll 1$, the dynamics of the junction are determined simply by the shunting resistance and the Josephson junction. The dimensionless equation of motion for the RCSJ model then becomes

$$\iota = \dot{\gamma} + \sin\gamma. \tag{2.11}$$

If I $< I_c$, then all the current flows through the junction and the voltage is zero, giving the dimensionless voltage across the junction

$$v = \frac{V}{I_c R} = \dot{\gamma} = 0, \tag{2.12}$$

and if I $> I_c$, the current flows through the Josephson junction and the resistor. Therefore equation 2.11 can be rewritten as

$$\tau = \frac{d\gamma}{\iota - \sin\gamma}. \tag{2.13}$$

Integrating over both sides of equation 2.13 gives the solution of τ in term of γ and ι, which is

$$\tau = \frac{2}{\sqrt{\iota^2 - 1}} \tan^{-1}\left(\frac{\iota \tan(\frac{\gamma}{2}) - 1}{\sqrt{\iota^2 - 1}}\right) \tag{2.14}$$

thus, the phase difference γ as a function of τ is

$$\gamma(\tau) = 2\tan^{-1}\left(\frac{1 + \sqrt{\iota^2 - 1}\tan(\frac{\tau\sqrt{\iota^2-1}}{2})}{\iota}\right) \tag{2.15}$$

which is a periodic function with period

$$\tau_T = \frac{2\pi}{\sqrt{\iota^2 - 1}}. \tag{2.16}$$

The time averaged dimensionless voltage is given by

$$u = \frac{2\pi}{\tau_T} = \sqrt{\iota^2 - 1} \tag{2.17}$$

Thus for I $> I_c$ the relation between I and V is just

$$V = uI_cR = I_cR\sqrt{\iota^2 - 1} = R\sqrt{I^2 - {I_c}^2}. \tag{2.18}$$

Hence, if we combine equation 2.18 and equation 2.12 we get the full I-V characteristics for $\beta_c \ll 1$ and for $I \ll I_c$ one finds ohmic behavior and the I-V curve

is non-hysteric because the effect of the capacitance is negligible in this limit. For $\beta_c \gg 1$, several resistances may be present, the shunt resistance R_s, a sub-gap resistance R_g, a normal resistance, R_n along with the resistance R. For this region, the smallest one will dominate for the appropriate voltage range.

C. Superconductivity Parameters

The micro-SQUID current phase relationship can be obtained by solving the Ginzburg-Landau equation and the supercurrent density for the full geometry of the device. The Ginzburg-Landau equation is given by

$$\alpha\psi + \beta|\psi|^2\psi + \frac{1}{2m^*}(\frac{\hbar}{i}\nabla - \frac{e^*\mathbf{A}}{c})^2\psi = 0 \tag{2.19}$$

and the supercurrent density is given by

$$\mathbf{J} = \frac{e^*\hbar}{2m^*i}(\psi^*\nabla\psi - \psi\nabla\psi^*) - \frac{e^{*2}}{m^*c})^2\psi^*\psi\mathbf{A} = 0 \tag{2.20}$$

where $m^* = 2m$ and $e^* = 2e$ is the mass and charge of the cooper pair, ψ is the wave function describing the superconducting state, and $\mathbf{A}$ is the vector potential.

A superconductor which is normally Type I in bulk form tends to behave like a type II superconductor in thin film form [39, 27] because several of its properties depends on its thickness, such as its penetration depth, coherence length and Ginzburg-Landau parameter (which are all functions of film thickness) [39]. The limit for this behavior is given by the Ginzburg-Landau parameter $\kappa = \Lambda/\xi$, with ξ being the coherence length. For $\kappa < 1/\sqrt{2}$, the superconductor is type I and for $\kappa > 1/\sqrt{2}$, the superconductor is type II [39, 40, 38, 36]. Under this limit, where there is a transition from type I to type II, the superconducting vortices form in the thin film. The vortex interactions of these thin films are mainly governed by the coherence

length ξ [39],

$$\xi(T) = 0.855\sqrt{\frac{\xi_0 l}{1 - \frac{T}{T_c}}} \tag{2.21}$$

in the sense that one can observe the transition of the vortices from a single object state where the vortices act independently of each other (small ξ and low temperature away from T_c) to a collective object state where the vortices interact with each other ($T \to T_c$, $\xi \to +\infty$) [39]. Equation 2.21 represents the dirty limit expression for the coherence length, which is the most commonly used expression for estimating the temperature dependent coherence length of a micro-SQUID [21, 1], l represents the mean free path of the superconducting film and ξ_0 represents the natural coherence length of the superconductor(see table I for examples of these coherence length values).

The effective area of the SQUID loop has been shown to be $(1 + \Lambda/\rho)\rho$, where ρ is the radius of the SQUID loop and $\Lambda = \lambda^2/d$ is the Pearl penetration depth and λ is the London penetration depth [41]. If the coherence length of the superconductor is greater than the penetration depth, the superconductor will be type I. Most pure metals, such as aluminum, lead and tin are superconductors. The values of the coherence lengths and penetration depths of aluminum, lead, and tin are shown in table I [36]. For a more extensive list of the coherence lengths and penetration depths of other superconductors, see reference [36]. For superconducting films of these materials, the temperature dependent coherence length was found to decrease and the penetration depth was found to increase as the temperature moves further below the critical temperature of the superconductor [1]. In addition to this, the thermal noise limit restrictions set by the Josephson junctions and the uncertainty principle when finding the minimum detectable change in magnetic field $\delta \mathrm{B} \approx 4^5 {\mu_0}^3 C/\beta^{5^{1/4}}$ (C being

Table I. Values for the Coherence Length and Penetration Depth of Aluminum, Lead and Tin. These Three Superconductors Were Used for the Fabrication and Analysis of Micro-SQUIDs.

Superconductor	Coherence Length (nm)	Penetration Depth (nm)
Aluminum (Al)	1600	16
Lead (Pb)	83	37
Tin (Sn)	230	34

the capacitance of the junctions) must also be considered [41].

The critical current created by a SQUID sensor produces periodic oscillations with respect to the applied magnetic flux [1, 26, 41]. The modulation depth is maximized if the coherence length is greater than or equal to the length of the junction bridge length. A high spatial resolution can be achieved if the Pearl depth is minimized by ensuring that the two dimensional thickness, d, of the superconductor is greater than or equal to the London depth [41]. The spatial resolution β is set by the larger of the two effective SQUID loop radii ρ and the closest distance of approach of the Pearl depth to London depth [41, 39].

CHAPTER III

DC-SQUID OVERVIEW

A. Introduction

In a superconducting quantum interference device (SQUID), the unique properties of superconductors are utilized. For a superconductor, the critical current is described as the amount of current that can pass through it before regaining a resistance. Hence, the critical current of the weak links in the superconducting state limits the amount of current that flows around the loop. Furthermore, any super-current (resistance-less current) that flows through the SQUID cannot exceed this critical current value. As described in chapter I, the basic structure of this device consists of a superconducting loop interrupted by two extremely thin junctions or bridges (in parallel with each other) known as weak links or Dayem bridges (see Fig. 4). The net flux enclosed by the loop Φ is the sum of the flux attributed to the applied magnetic field Φ_X and the flux created by the circulating super-current in the loop Φ_S. If we take out the weak links from the superconducting loop, so that it is without any impediments, and cool it below its transition temperature in the presence of a changing magnetic field applied perpendicular to the plane of the loop, a current would be induced (see Fig. 5). This induced current usually circulates along a path that generates flux which has a tendency to cancel out the flux produced by the changing magnetic field. In addition, a phase difference is created on either side of the junctions when in the superconducting state because the weak links have a smaller critical current than the critical currents in the larger sections of the loop.

As the electron pair wave travels along the superconductor, it splits up into two components and these wave components in turn travel along the two sections of

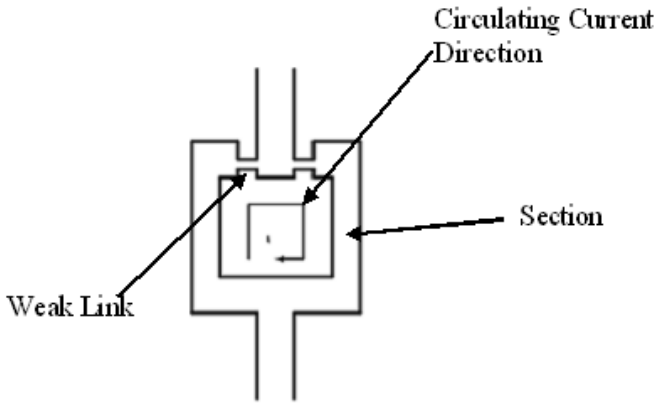

Fig. 4. Diagram of a Superconducting Quantum Interference Device Which Shows the Circulating Current Direction. The Basic Structure of This Device Consists of Two Extremely Thin Junctions Weak Links or Dayem Bridges Connecting the Two Sections or Arms of the Superconducting Loop Together.

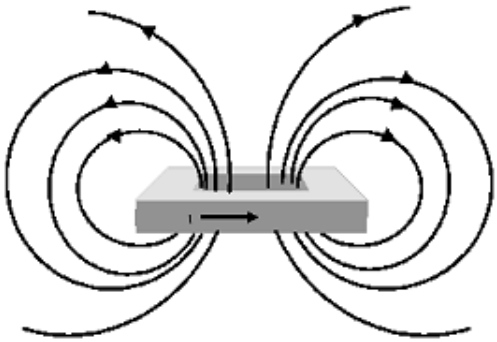

Fig. 5. Flux Through Superconducting Loop. A Current Would Be Induced If We Take Out the Weak Links From the Superconducting Loop and Cool It Below Its Transition Temperature in the Presence of a Changing Magnetic Field Applied Perpendicular to the Plane of the Loop.

the loop. The two waves then encounter the junctions that obstruct their path and impede their progression before recombining into the original wave. One can then measure the phase difference of the waves due to the varying conditions in the two paths. This splitting and recombining of the electron pair wave results in the creation of an interference pattern [40, 27, 28]. The current of paired electrons increases as the phase difference of the electron pair wave across the junctions increases and the super-current reaches its critical value when the phase difference is $\frac{n\pi}{2}$, where n is an integer.

In the presence of a magnetic field, there are two distinct phase differences that occur in the SQUID loop, one that occurs across the superconducting sections and one that occurs across the weak links due to a circulating super-current [40]. The first occurs once the magnetic field is applied perpendicular to the plane of the loop where it produces a phase difference due to the progression of the electron pair wave around the sections of the loop and the phase difference due to the weak links is very small and considered negligible. However, for the second instance where a small circulating

super-current I_s is produced around the loop, there will be a phase difference across the weak links and a negligible amount across the sections. Conversely, in the absence of an applied magnetic field, the phase is the same at any point on the loop. There is also very little phase difference between the sections (arms of the loop). This is because of the long wavelength of the electron pair wave which results from the small Cooper pair momentum and the low superconductor current density.

For a flux cancellation to occur, the magnitude of the circulating super-current I_s must satisfy the condition that $L|I_s| = \Phi_X$, where L is the inductance of the loop and $\Phi_X = AB$ is the flux of the applied magnetic field B through a hole with area A. The circulating super-current causes the net flux $\Phi = \Phi_X + \Phi_S$ that encloses the area of the loop to be quantized by adjusting the value of the flux Φ_S as the flux of the applied magnetic field Φ_X changes. These quantized values exist as multiples of a flux quantum or fluxon $\Phi_0 = 20.678$ gauss μm^2.

The introduction of the weak links into the superconducting loop will cause any circulating super-current to be limited to the critical current value generated by the bridges. Moreover, these bridges usually generate very small critical current values which usually limit the value of the circulating super-current to an even smaller value. As a result of this limitation, the applied magnetic field must be very small if the flux through the loop is to be maintained at zero. For the analysis that follows, we will discuss the behavior of a SQUID constructed such that the critical current values of the weak links (Dayem bridges) I_c and the inductance of the loop L are small enough so that the flux generated by the circulating super-current around the loop is negligible and very much smaller than one flux quantum $I_s L \leq I_c L \ll \Phi_0$, but still cause a significant change in phase across the weak links.

A considerably small circulating super-current I_s would not be able to generate a flux that is close to one fluxon, and the net flux enclosed by the loop would be

approximately the same as the flux generated by the applied magnetic field $\Phi \cong \Phi_X$. If the weak links are present, the flux inside the loop does not have to be equal to an integer number of fluxons. The circulating current will produce a significant phase difference across each weak link that would allow the total phase change around the loop to be equal to $2n\pi$.

The phase difference between two points around the loop generated by the magnetic field applied perpendicular to the loop is given by

$$\phi_2 - \phi_1 = \frac{4\pi e}{h} \oint A \cdot dl = \Delta\phi(B). \tag{3.1}$$

Note that $\oint A \cdot dl = \Phi_X$ is the flux enclosed by the loop generated by an applied magnetic field, where $\frac{h}{2e} = \Phi_0$ is one flux quantum or fluxon and this is made possible because we considered the flux produced by the circulating super-current $I_s L$ to be negligible under the condition, $I_s L \leq I_c L \ll \Phi$ and $\Phi \cong \Phi_X$. Hence we can state that the phase difference is

$$\Delta\phi(B) = 2\pi \frac{\Phi_X}{\Phi_0} \tag{3.2}$$

and is proportional to the flux generated by the applied magnetic field. In order to satisfy the condition that the phase difference around a superconducting closed path must be an integer multiple of 2π, the phase difference of the magnetic field has to be added to the phase difference of the circulating current I_s through the two weak links $2\Delta\phi(I_s)$ so that the total phase change is a multiple of 2π,

$$\Delta\phi(B) + 2\Delta\phi(I_s) = 2n\pi \tag{3.3}$$

because the magnetic field will not be strong enough to produce an integer number of fluxons by itself.

We can now formulate a relation that explains how the circulating super-current depends on the magnitude of the applied magnetic field by first looking at how the circulating super-current relates to the phase difference across the weak links $2\Delta\phi(I_s)$ by using the equation

$$\sin\Delta\phi(I_s) = \frac{I_s}{I_c}. \tag{3.4}$$

If the phase difference of the magnetic field exactly cancels out the phase across the weak links then assuming that the current is circulating in a direction that is the most energetically favorable,

$$\Delta\phi(B) + 2\Delta\phi(I_s) = 0, \tag{3.5}$$

$$\Rightarrow \Delta\phi(B) = -2\Delta\phi(I_s). \tag{3.6}$$

Thus substituting into $\sin\Delta\phi(I_s) = \frac{I_s}{I_c}$ the phase difference across the weak links becomes

$$\Delta\phi(I_s) = -\frac{\Delta\phi(B)}{2} = -\pi\frac{\Phi_X}{\Phi_0} \tag{3.7}$$

which gives

$$\sin(-\pi\frac{\Phi_X}{\Phi_0}) = \frac{I_s}{I_c} \tag{3.8}$$

which results in

$$|I_s| = I_c\sin(\pi\frac{\Phi_X}{\Phi_0}). \tag{3.9}$$

Now if the magnetic field is increased so that the flux through the loop is $\frac{\Phi_0}{2}$ then the circulating super-current would equal the critical current of the weak links and the

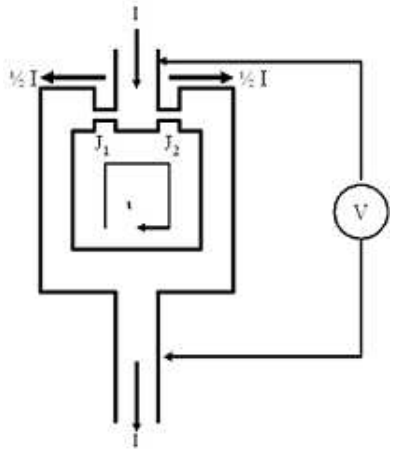

Fig. 6. Measuring Current Passing Through SQUID Device. I is Called the Transport Current or Measuring Current and Divides Equally along the Two Paths If the Device Is Symmetric. The Value of the Measuring Current Where a Voltage Drop Appears Is Called the Critical Current I_c.

junctions would become normal causing the critical current to be reduced to zero. As the magnetic field is increased further so that the applied flux is greater than $\frac{\Phi_0}{2}$, it is now more energetically favorable to bring the total phase change to 2π by adding the phase difference of the weak links due to the circulating current to the phase difference due to the applied magnetic field. As the field continues to increase the circulating super-current I_s will vary periodically with it, switching from $-I_c$ to $+I_c$ when the flux through the loop is an odd multiple of $\frac{\Phi_0}{2}$. The period of oscillation of the circulating current corresponds to one flux quantum.

If we pass a current I through the loop we can detect changes to the circulating current I_s. I is called the transport current or measuring current and divides equally along the two paths if the device is symmetric, (Fig. 6). For this current, no voltage will be detected across the SQUID circuit as long as the device is superconducting. However if the measuring current is increased enough, a voltage will be produced.

The value of the measuring current where a voltage drop appears is called the critical current I_c or maximum super-current of the loop.

To determine the value of the critical measuring current and how it varies with a changing magnetic field, we have to analyze the phase changes of the weak links and that of the applied magnetic field. In the case of the weak links we denote the phase changes across each junction by α and β, and if the loop is superconducting it must satisfy the condition that

$$\alpha + \beta + \Delta\phi(B) = 2n\pi \tag{3.10}$$

which results in

$$\alpha + \beta + 2\pi\frac{\Phi_X}{\Phi_0} = 2n\pi \tag{3.11}$$

If there is no measuring current I, the phase differences across the two junctions are equal because the same circulating current flows to each of them, thus

$$\alpha = \beta = \pi[n - \frac{\Phi_X}{\Phi_0}]. \tag{3.12}$$

If the measuring current is now allowed through the superconducting circuit, this would result in α and β being different and the current through the junctions are $I_\alpha = I_s - \frac{I}{2}$ and $I_\beta = I_s + \frac{I}{2}$ respectively. In this case, $\alpha + \beta$ must be a constant, so if α decreases then β must increase to keep the sum of the phase differences constant. If we denote increase or decrease in the phase difference by δ in the presence of the measuring current, then we can give an expression for α and β,

$$\alpha = \pi(n - \frac{\Phi_X}{\Phi_0}) - \delta \tag{3.13}$$

$$\beta = \pi(n - \frac{\Phi_X}{\Phi_0}) + \delta \tag{3.14}$$

and the currents through the junctions take on the form $I_\alpha = I_c \sin\alpha$ and $I_\beta = I_c \sin\beta$ which leads to the expressions

$$I_\alpha = I_s - \frac{I}{2} = I_c \sin[\pi(n - \frac{\Phi_X}{\Phi_0}) - \delta] \tag{3.15}$$

$$I_\beta = I_s + \frac{I}{2} = I_c \sin[\pi(n - \frac{\Phi_X}{\Phi_0}) + \delta]. \tag{3.16}$$

We can find how the measuring current relates to the flux by eliminating the critical current in the above equations using $I = I_\beta - I_\alpha$, hence we have

$$I = I_c\{\sin[\pi(n - \frac{\Phi_X}{\Phi_0}) + \delta] - \sin[\pi(n - \frac{\Phi_X}{\Phi_0}) - \delta]\} \tag{3.17}$$

Utilizing the trigonometric identity

$$\sin(A + B) = \sin(A - B) = 2\cos A \sin B \tag{3.18}$$

We get

$$I = 2I_c \cos[\pi(n - \frac{\Phi_X}{\Phi_0})] \sin\delta. \tag{3.19}$$

The value of the measuring current could either be positive or negative, depending on if the values of sine and cosine have the same or opposite signs. We will consider the direction in which the measuring current is positive, thus

$$I = 2I_c |\cos[\pi(n - \frac{\Phi_X}{\Phi_0})] \sin\delta| \tag{3.20}$$

and simplifying the terms under the cosine gives

$$\cos[\pi(n - \frac{\Phi_X}{\Phi_0})] = \cos n\pi \cos(\frac{\Phi_X}{\Phi_0}) + \sin n\pi \sin(\frac{\Phi_X}{\Phi_0}) = \pm \cos(\frac{\Phi_X}{\Phi_0}) \tag{3.21}$$

we also know that $|\sin\delta| \leq 1$, hence the measuring current is

$$I \leq 2I_c|\cos[\pi(\frac{\Phi_X}{\Phi_0})]| \tag{3.22}$$

and this condition must be satisfied for the loop to remain superconducting, hence the critical current (maximum super-current) is

$$I_m = 2I_c|\cos[\pi(\frac{\Phi_X}{\Phi_0})]| \tag{3.23}$$

which varies periodically with the magnitude of the applied magnetic field and reaches its maximum value when the flux through the loop is an integer multiple of a fluxon. This periodic variation is called an interference pattern. The pattern is created when the area of the hole and the critical current of the weak links are small, since the circulating current induced by the magnetic field has to be smaller than the critical current through the weak links and hence will not be able to generate a flux large enough to cancel the flux through the loop.

In actual experiments, the interference pattern generated may be modulated by diffraction like effects at the weak links. This is mainly due to some comparative difference in the cross sectional area of the two weak links. The pattern would then have two periodicities due to the weak links. As a result a modulated periodic pattern is produced. Hence the critical current of one weak link would vary with the applied magnetic field as

$$I_c = I_c(0)|\frac{\sin[\pi(\frac{\Phi_J}{\Phi_0})]}{\pi(\frac{\Phi_J}{\Phi_0})}| \tag{3.24}$$

where Φ_J is the flux of the applied magnetic field passing through an area of the weak link.

B. The Screening Parameter

For our analysis in section A, the difference Φ_S between the flux generated by an external applied field (external source) Φ_X and the real flux enclosed by the superconducting loop Φ was taken to be negligible. However, there are two situations that cause this difference in flux Φ_S to be non-zero, the first due to the flux coupled into the loop by a bias current and the other due to the screening current circulating around the loop. We can eliminate the flux coupling due to the bias current by attaching the leads symmetrically to the loop and we have applied this to our analysis. We will now extend our treatment of our superconducting loops interrupted by weak links discussed in section A to include the added contribution due to screening currents. For this treatment we create a more general model by introducing a gauge invariant phase quantity:

$$\gamma = \Delta\phi - \frac{2\pi}{\Phi_0}\oint \mathbf{A}\cdot\mathbf{dl}. \tag{3.25}$$

To create a more general solution for the phase change of the SQUID loop we must envision creating a line integral of $\mathbf{A}$ around a contour passing through both weak links and arms, which the flux Φ that encloses the loop. The thickness of the arms for our experiments are always thicker than the penetration depth λ thus $\mathbf{A} = \frac{\Phi_0}{2\pi}\Delta\phi$ since the super-current velocity inside the arms is zero [27]. Thus the flux enclosing the loop would be

$$\Phi = \oint \mathbf{A}\cdot\mathbf{dl} = \frac{\Phi_0}{2\pi}\int_{arms}\Delta\phi\cdot dl + \int_{links}.\mathbf{A}\cdot\mathbf{dl} \tag{3.26}$$

The phase ϕ has to be single valued (from our discussion of the Ginzburg-Landau theory) thus equation 3.26 can be represented as the sum of $\frac{\Phi_0}{2\pi}\int_{arms}\Delta\phi\cdot dl$ and the finite phase differences across the weak links must be equal to zero modulo 2π [27],

$$\frac{\Phi_0}{2\pi}\int_{arms}\Delta\phi\cdot dl+\sum_{j\ \ links}\Delta\phi_j=0\ \mathbf{mod}\ 2\pi. \tag{3.27}$$

Thus from equation 3.27 we see that the sum of the gauge invariant phase differences γ_j taken in the same direction around our contour is $\frac{2\pi\Phi}{\Phi_0}$. One can then define the gauge invariant phase change for the total measuring current or transport current by

$$\gamma_1-\gamma_2=2\pi\frac{\Phi}{\Phi_0}\ \mathbf{mod}\ 2\pi \tag{3.28}$$

Here the actual flux enclosed by the loop Φ is the sum of the external applied magnetic field Φ_X and the flux due to the screening current circulating the loop Φ_S. As we have seen in section A, the screening component of the flux is given by $\Phi_S = I_sL$, where L is the inductance of the loop,

$$\Phi=\Phi_X+\Phi_S. \tag{3.29}$$

The screening current (the current that produces the screening flux Φ_S) can thus be represented by

$$I_s=\frac{I_c}{2}(\sin\gamma_2-\sin\gamma_1) \tag{3.30}$$

and the measuring current (transport current) can also be represented by the sum of the currents through each weak link under the gauge invariant phase quantity

$$I=I_c(\sin\gamma_1+\sin\gamma_2). \tag{3.31}$$

From our previous analysis we can see that equations 3.30 and 3.31 are constrained by equation 3.28. Given the measuring current I ,the inductance of the loop L and the real flux enclosed by the loop Φ, we can determine the constituent components of the enclosed flux (Φ_S the screening flux component and Φ_X the applied flux component) by solving equation 3.28 to get one of the phase differences γ_j in terms of the other [27], then making the necessary substitutions into equations 3.30 and 3.31. For the case were the measuring current $I \approx 0$ then equation 3.28 gives $\gamma_1 = -\gamma_2$ which when substituted into 3.29 gives

$$\Phi = \Phi_X + LI_c \sin(\frac{\pi\Phi}{\Phi_0}). \tag{3.32}$$

In our analysis in A we used the case where $I_s = 0$ and $\Phi = \Phi_X$, thus we can see from our constraint equation 3.28 that $\gamma_1 = \gamma_2(\ \mathbf{mod}\ 2\pi)$ giving $\Phi = n\Phi_0$, as a consequence the periodicity of the SQUID response to the externally applied magnetic field Φ_X would be in integer multiples of Φ_0 and thus would not be affected by screening [27]. Optimization of the SQUID operation also requires that the relation between Φ and Φ_X be single valued and non-hysteretic in behavior [15]. The necessary conditions for this to occur can be derived by examining the screening component of the enclosed flux. From equation 3.30 we can see that the maximum value that would be obtained would occur when the circulating screening current is equal to the critical current $\Phi_S = I_sL = I_cL$. Moreover, one can observe that if $|\Phi_S| < \frac{\Phi_0}{2}$ the screening will be insufficient to give a multivalued relationship between Φ and Φ_X given the period Φ_0 [27].

Contrary to our analysis in section A, there may be times when the combination of the critical current of the weak links and the size of the hole are large enough for the amount of flux cancellation due to the induced circulating current to be significant

so that only a small amount of flux is coming through (net flux enclosed by the loop is small). This process is known as screening and happens when $I_cL > \frac{\Phi_0}{2}$ and the depth of modulation of the measured critical current is reduced to $\frac{\Phi_0}{L}$, due to the effects of magnetic hysteresis.

Magnetic hysteresis is a result of the displacement of vortices trapped in the superconducting structure of the SQUIDs during cooling or when an applied field is large enough to create new vortices in the superconducting structure [42, 43]. It is the response (shift) of voltage-flux $V(\Phi)$ in the SQUID as an applied magnetic field H is varied. The effective hysteresis of the SQUID loop is denoted by $\delta H = \frac{\delta\Phi}{A_E}$, where $\delta\Phi$ is the net flux change in the SQUID loop and A_E is the effective area of the SQUID loop.

The flux to voltage transfer function V_Φ of a single SQUID is given by

$$V_\Phi = \frac{\partial V}{\partial \Phi} \approxeq \pi \frac{\Delta V}{\Delta \Phi_0} \approxeq \frac{\Delta V}{\frac{\Phi_0}{2}} \approxeq \frac{R}{2L}, \tag{3.33}$$

where ΔV in equation 3.33 is the voltage modulation depth which is represented by the formula

$$\Delta V \approx \Delta I_c(\frac{R}{2}) \approx \frac{I_c R}{2} \tag{3.34}$$

where I_c is the critical current, R is the linear shunted resistance of a Josephson junction and Φ_0 is the fluxon [32]. In addition, the voltage signal of a single SQUID can be considerably enlarged by connecting identical SQUIDs in series. If N SQUIDs are connected in series and their voltages add coherently, the total array voltage modulation depth is

$$\Delta V_{SERIES} = N(\Delta V)_{SQUID} \tag{3.35}$$

with

$$V_{\Phi SERIES} = NV_{\Phi}. \tag{3.36}$$

The screening parameter is defined by $\beta \equiv \frac{2LI_c}{\Phi_0}$ and is used to determine the condition for the presence of magnetic hysteresis in our SQUID device. If $\beta \leq \frac{2}{\pi} \sim 1$, then there would be no contribution by magnetic hysteresis to our SQUID response. However, if $\beta \geq \frac{2}{\pi}$ the SQUID enters an operating regime where there is more than one induced screening current state established within the device for an applied flux.

C. Noise

The ability of a SQUID to detect small magnetic fields is ultimately limited by the noise in the SQUID itself. The noise can be separated into two distinct categories, white noise and $\frac{1}{f}$ noise [14, 15]. White noise arises from the resistive shunts in the SQUID and does not depend on the frequency of the input signal. $\frac{1}{f}$ noise or excess low frequency noise increases with the decreasing frequency of the input signal and is usually only visible below 1KHz.

Some of the sources of $\frac{1}{f}$ noise include the critical current fluctuations and vortex hopping. The critical current fluctuations occur because of the microscopic physical processes within each junction, such as an electron being trapped in the junction. Vortex hopping occurs when there is thermal activation that causes the vortices to hop randomly between pinning sites. One can reduce the noise from the critical current fluctuations by various methods. One method would be to reduce these fluctuations using a reverse bias scheme, where the bias current is reversed regularly so that the additional circulating current switches back and forth to effectively cancel itself out. The effect of vortex hopping noise, however, cannot be reduced by an electronic biasing scheme. This noise is affected by the SQUID design, the cooling

method and the film quality. It has been reported that the noise level is much lower with smaller arm widths [44].

The flux noise spectral density $S_\Phi(f)$ for a single SQUID is given by

$$S_\Phi(f) = \frac{S_V(f)}{(\frac{\partial V}{\partial \Phi})^2}, \tag{3.37}$$

where

$$S_V(f) = \frac{4k_BT}{R_n}(R_d)^2(1 + \frac{1}{2}(\frac{I_c}{I})^2) \tag{3.38}$$

is the voltage noise spectral density. Note that R_d is the dynamic resistance at the operating point, R_n is the normal resistance of the device, I is the bias current and k_B is the Boltzmann constant. For N SQUIDs connected in series

$$S_V(f)_{SERIES} = NS_V(f). \tag{3.39}$$

CHAPTER IV

DEVICE FABRICATION

Construction of the Superconducting Quantum Interference Device was carried out using the Electron Beam Lithography processing technique. An illustration of this process is shown in Fig. 7. Features produced by Electron Beam Lithography have been shown to have line widths as low as 500 Åfor the micro-SQUID nanobridges [26], which makes this technique a suitable candidate to produced devices with minute dimensions.

A. Substrate Preparation

A 1 cm by 1 cm silicon chip was cut from a commercial stock (N Type, $1 - 30\ \Omega\ cm$) of 4 inch silicon wafers and used as the substrate for the micro-SQUID device fabrication. The chip (wafer section) was then placed in an acetone bath and sonicated for 5 to 10 minutes (ultrasonic bath) to clear the substrate surface of any debris that may have been deposited on the silicon surface during cutting. After sonication, the substrate was then cleaned with acetone, then rinsed with isopropyl alcohol (IPA) then subsequently blown dry with nitrogen gas. The substrate was then baked for about 10 to 20 minutes on a hot plate to remove any residual solvents that may have been left over from the cleaning process. The sample was then taken off the hot plate and allowed to be cooled back down to room temperature.

The sample was then place in a spin coater and a 1 ml to 3 ml pipette was used to place two drops of the positive photo-resist (resin) on the substrate surface. The resist used consisted of a 2% or 3% mixture of Poly Methyl Methacrylate (PMMA) and Monochlorobenzene which had a molecular weight of 950 K. These small percentage mixtures of PMMA are known to produce extremely small pattern line widths (very

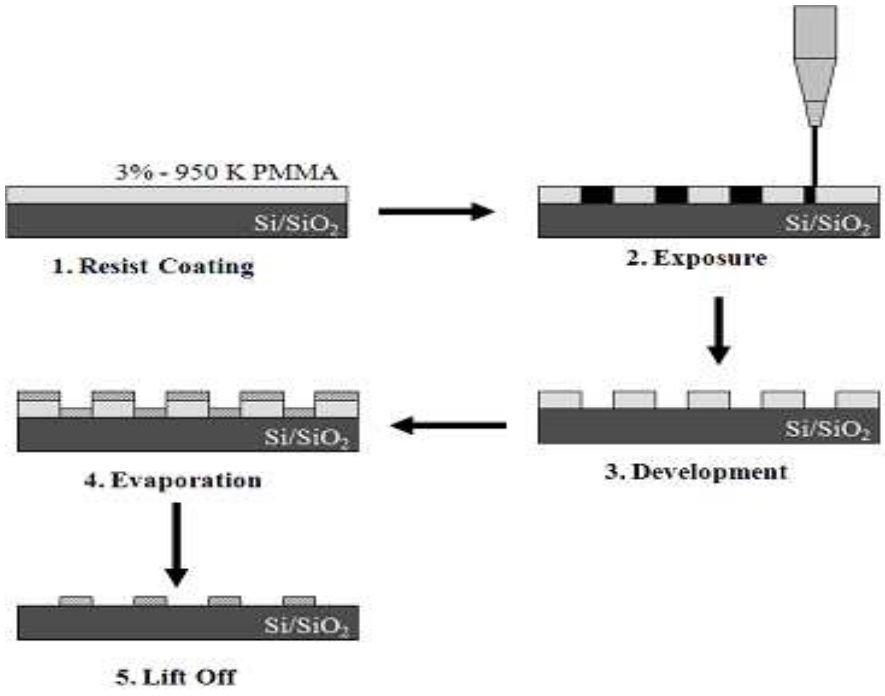

Fig. 7. The Sample Preparation Process. A Silicon Substrate Is Coated with PMMA then Irradiated with an Electron Beam to Form a Mask for Metallization. The Final Pattern Is Formed by Lift Off.

high resolutions) for the devices in question. The resin was then spun onto the surface at approximately 3000-5000 RPM for about 40-60 seconds. Spin speeds at the lower end of this range were used to produce thicker films (2000 Åto 3000 Å) of PMMA. After the substrate was coated with the PMMA resin, it was then soft baked (heated on a hot plate for a short time) for about 90 seconds at temperatures of 160-165 °C. Once the sample was cooled, it was ready to be placed in the electron beam lithography system.

B. Lithography Hardware and Software

The electron beam lithography system consists of a scanning electron microscope and a pattern generation (writing) system which are controlled by two computers that run the scanning electron microscope functions and the pattern generation software respectively. These computers control functions such as setting the exposure parameters, loading and unloading of the sample, alignment and focusing of the beam, and reading the data file with the pattern generation system for use in writing. There are also control electronics that are utilized to help with the interface between the pattern generation system and the microscope.

The scanning electron microscope used is the JEOL JSM 6460. It has a maximum accelerating voltage of 30 kV and a resolution of 3nm for viewing a sample. It can achieve magnifications of 35 X to 300,000 X for a working distance of 7 mm, which was the typical working distance used for device fabrication. It also has the ability to generate a wide range of probe currents, where 5 pA to 0.5 μA correspond to spot sizes in the range of 13 to 90 and an aperture size of 30 μm. Even though the most common aperture used was 30 μm, the JEOL JSM 6460 had three options for the objective lens aperture size, 20 μm, 30 μm and 100 μm. Inside the microscope

column are components that control the electron beam so that it projects straight down unto the sample. The column consists of an electron source, a condenser lens and objective lens, a beam deflector, a beam blanker to turn the beam on and off, a stigmator to correct any astigmatism (distortion) in the beam, an aperture to make the beam more defined and concentrated, an alignment system to center the beam down through the column and an electron detector for better viewing of images on the screen.

The electron source used in the microscope is thermionic. It consists of a V shaped tungsten wire called the filament. Tungsten is used because of its ability to fare well at high temperatures and low pressures [45]. The tungsten filament makes up the cathode of the electron gun which accelerates the electrons down the column. Thermionic emission of the electrons is caused by passing a current through the tungsten filament. The three key parameters of the source are the size, brightness and energy spread of the emitted electrons [45]. The electron lenses inside the column reduce the source beam diameter so that a spot can be created on the sample. The brightness of the source relates to the current in the electron beam, so the brighter the source the higher the current produced. The electron beam wavelength is comparable to monochromatic light and has a narrow energy spread. This monochromatic (light and dark) effect is how samples are viewed [45].

As the beam travels further down the column it encounters the condenser lens which is a two stage electro-magnetic lens that is used to reduce the beams diameter as it goes through it. The condenser lens is located in the gun region because it is usually combined with the anode that is used to accelerate the electrons from the electron gun cathode. An aperture which is usually a small circular hole is used to also limit the beam down the column. As the beam can only pass through the hole it stops any spraying of the electrons and gives it a distinct shape as it passes through.

The final lens is the objective lens. This lens is a conical electromagnetic lens because it will provide fewer aberrations (distortions) than electrostatic lens used in similar microscopes. Electrostatic lenses tend to have defects in the mirrors that cause these aberrations and so using an electromagnetic lens would lower the distortions.

Below the column is a pressurized chamber that contains a Deben motorized laser stage for loading and unloading the sample and moving the sample around in X and Y directions when patterning. The laser stage does not have a Z axis or a rotational axis. The X and Y axes are planar axes that are parallel to the plane of the sample. Below the chamber is a vacuum system that is used to maintain a suitable pressure when the chamber is loaded for use (evacuation) or unloaded for development (venting).

The pattern generation system used was the Nano Pattern Generation System (NPGS) distributed by J.C. Nabity Lithography Systems. It has a Microsoft Windows based software packaged system that incorporates a CAD program, called DesignCAD LT 2000. DesignCAD makes the patterns and utilizes an ASCII environment to communicate the pattern to nano-Pattern Generation software (NPGS), which then reads, interprets, converts (into a run file) then runs the created CAD files. Each converted pattern data was sent to the NPGS data decoder which sends the pattern generation path to the beam blanker. The beam blanker was then used to control the beam by shutting it on and off with an applied voltage which moved the beam on and off axis, a process called blanking. The microscope deflection coils (can be thought of as plates for purposes of simplicity) were then able to move the beam across the sample by applying a magnetic field to generate the pattern, (see Fig. 8).

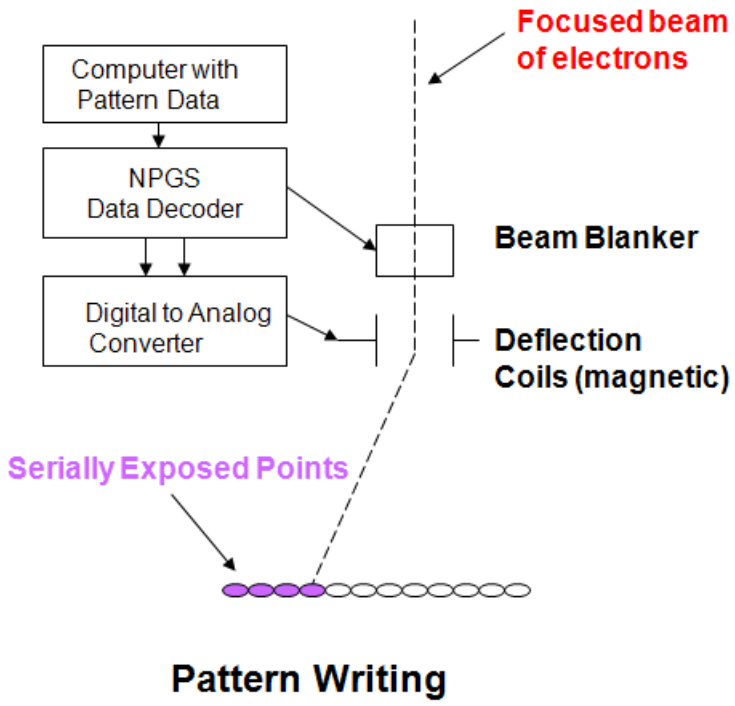

Fig. 8. Nano-Patterning Software Control of the Electron Beam. The Beam Blanker Was Used to Control the Beam by Shutting It On and Off with an Applied Voltage. The Deflection Coils Moves the Beam Across the Sample along a Specified Path.

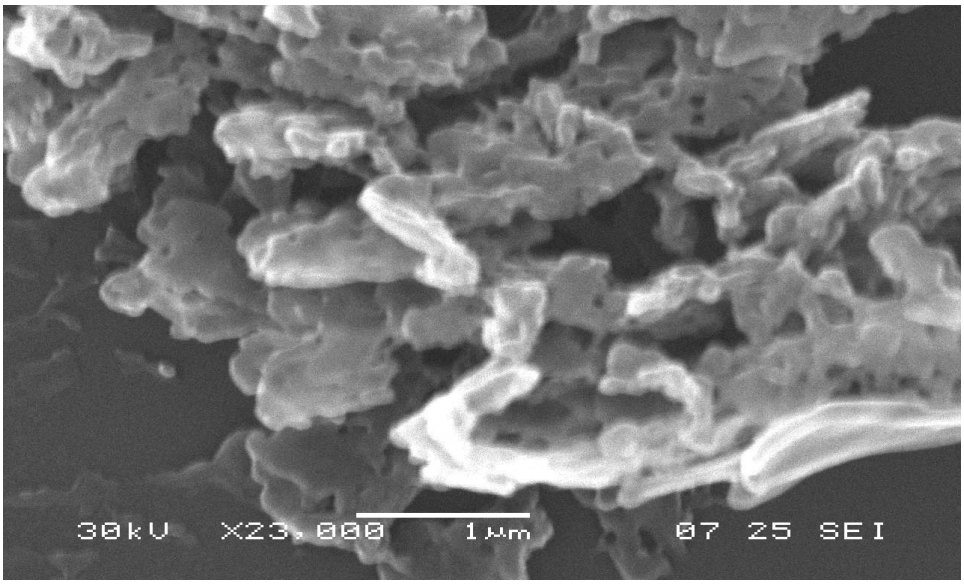

Fig. 9. Scratch on PMMA to View Fine Features at Large Magnification. It Is Placed at the Tip of the Sample before Mounting and Assists with Improving Focus on Small Features.

C. Pattern Writing and Development Process

Optimization of the microscope is done using three components, a scratch on the substrate surface (Fig. 9), a Faraday cup (Fig. 10) and a Gold Standard (Fig. 11). To create a pattern on the resist, a scratch must first be placed at the tip of the sample to act as a marker (a large target to focus on with the microscope to compare against small features) before mounting. The sample was then placed into a scanning electron microscope that has been suitably adapted to handle the lithography process. The Faraday cup and the gold standard are mounted on the stage itself in close proximity to the sample.

The Faraday cup is used along with a picoammeter to measure the actual beam current on the sample. If the picoammeter was used alone to measure the beam

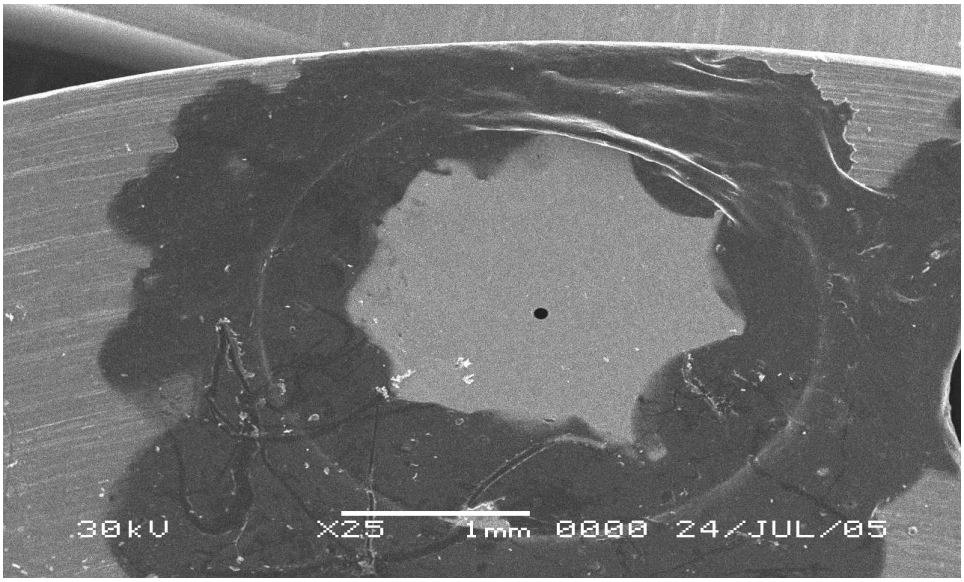

Fig. 10. Faraday Cup Used to Measure the Current on the Sample More Accurately. All of the Beam Is Captured Inside and a More Accurate Reading Obtained. Gun alignment Is Also Done in the Faraday Cup Which Allows the Beam Current Value to be Maximized.

current, the reading would be inaccurate due o scattering effects. The value of the current shown is reduced significantly from what it actually is because some of the beam is scattered across and not taken into account by the picoammeter. The Faraday cup, which is just an aperture covering a hole filled with carbon paint acts like a black hole in the sense that all of the beam can be captured inside and the correct reading can be obtained. Gun alignment is also done in the Faraday cup so that the beam current value can be maximized.

The gold standard is gold sputtered on a carbon base. This is used to obtain the best resolution for the lithography process. These clusters are brought into focus by adjusting, the objective lens aperture, the focal length and the stigmator. If when optimizing the microscope one cannot achieve a clear image at a magnification of 100

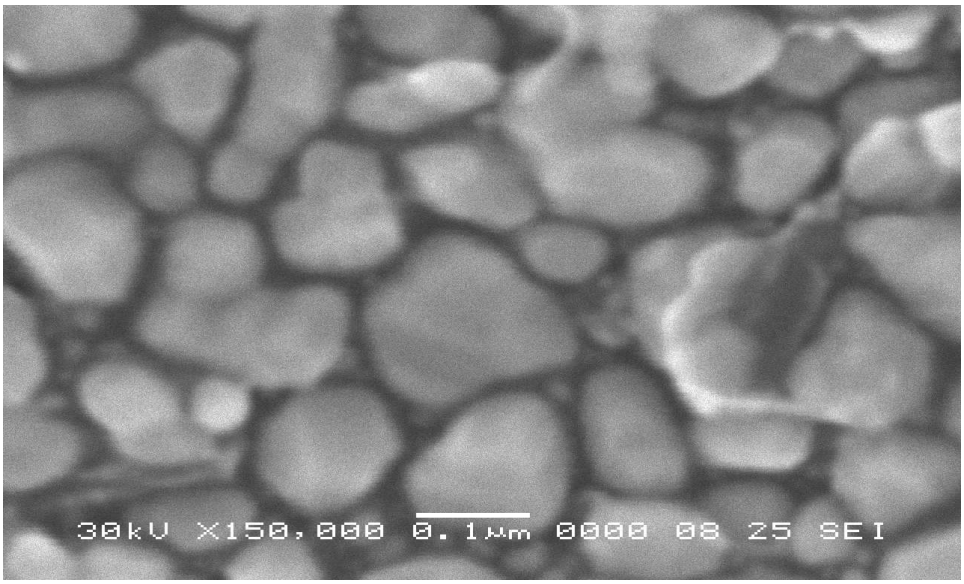

Fig. 11. Gold Clusters (Standard) Used for Optimization of the Microscope in Pattern Writing. The Size of the Clusters Are Used as a Calibration Tool to Bring the Behavior of the Microscope to a Level at Which a Pattern Can Be Written at a Size Comparable to the Cluster Size.

000 X then the possibility of creating a pattern is almost impossible. So it is crucial that one understands the electron optics system and be able to optimize accordingly. In addition to correcting the lenses for better resolution of the gold clusters, the stigmator corrects the astigmatism or distortions due to the condenser lens that may warp the shape of the clusters.

Once the beam reaches the sample it penetrates the resist causing the beam to be scattered within the resist. The beam becomes wider but continues to pass through the resist until it reaches the silicon/silicon dioxide substrate where it undergoes scattering back through the resist, this is normally called backscattering. Backscattering causes the initial dose generated by the initial electron penetration to be deposited at secondary locations close to the first. In the lithography community, this event

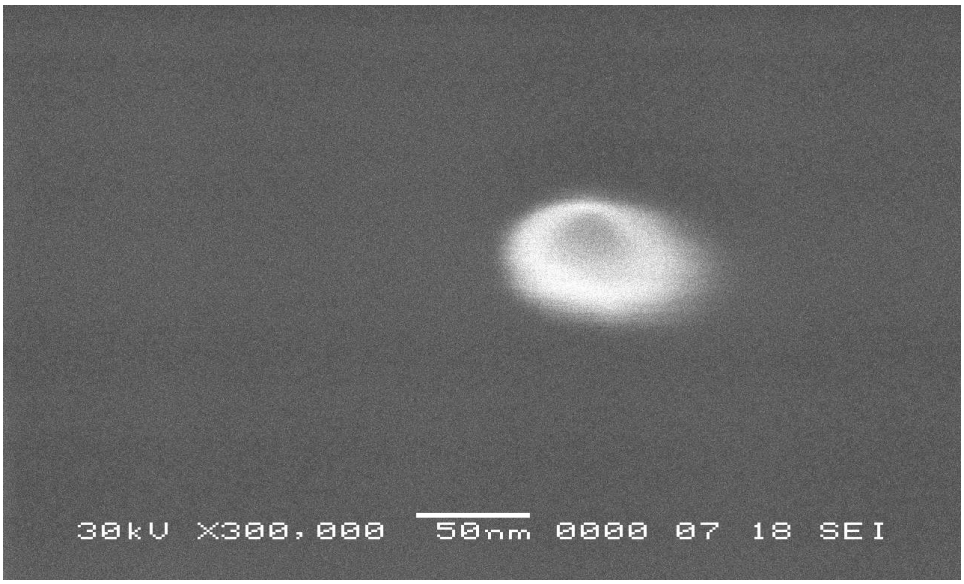

Fig. 12. Contamination Spot Created in a Beam Hold position. The Spot Is Grown on the Surface of the Resist and the Exposed Area Viewed by the Scanning Electron Microscope.

is known as the proximity effect. This effect becomes a great concern as you go to smaller and smaller features because it may cause broadening of the pattern features which may not be desirable. Care must be taken when patterning to minimize these scattering contributions when fabricating fine features because this will ultimately hinder the resolution capabilities.

One way to systematically ensure that fine features are patterned on to the resist is to create a small spot (see, Fig. 12) on the resist with an optimized fine beam. By placing the patterning software in a beam hold position, one spot can be grown on the surface of the resist and the exposed area can be viewed for an even finer adjustment of the optimized settings.

After surface irradiation, the sample is removed from the microscope and undergoes a subsequent development step. This step entails immersing the sample in a

developing solution for approximately 60 seconds, rinsing the sample with isopropyl alcohol then drying with a flow of nitrogen gas. The developer used is a mixture of one part methyl isobutyl ketone (MIBK) to three parts isopropyl alcohol. The reason for the dilution results from the MIBK being such a strong developer that it could damage the unexposed resist that holds the pattern. Therefore the dilution ratio used would produce high resolution results while reducing the chance of having the embedded pattern being destroyed by the developing solution.

D. Thin Film Deposition

To complete the fabrication process, a thin film superconductor was deposited on the patterned PMMA mask using resistive heating thermal evaporation(see Fig. 13) [45]. For this process, the superconducting material was placed under vacuum in a boat or basket (metal holder made primarily of Tungsten) and heated above its melting point (Al = 660 °C, Pb = 327.5 °C, Sn = 231.9 °C) in the presence of the silicon substrate containing the PMMA mask. To reach a vacuum state, the chamber containing the sample was pumped out with a roughing pump to about 10^{-2} Torr, then subsequently with a diffusion pump backed by a roughing pump to reach pressures of 10^{-6} Torr. Tungsten is one of the most common materials used in the boat/basket construction because of its high melting point (3410 °C). This ensures that it will not react with the superconductors undergoing testing which can be evaporated at much lower temperatures.

The heating of the superconducting material was produced when an electric current flows through the Tungsten boat/basket when a voltage is applied across it. The atoms are energized as metal vapor and drift to the sample surface where they attach themselves (through condensation of the vapor), these atoms also get

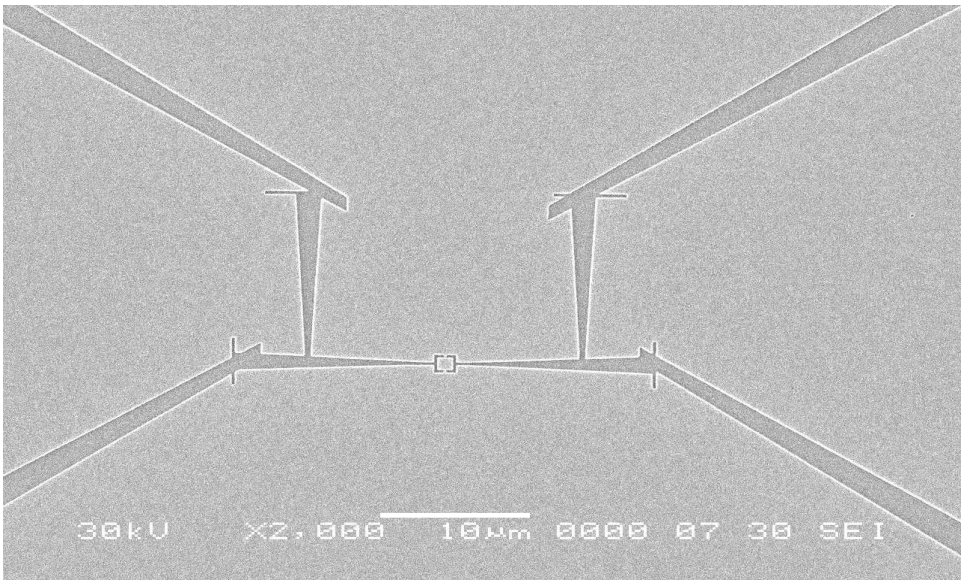

Fig. 13. Metalization of Micro-SQUID Circuit. The Darker Region Shows the Outline of the Leads and the Device Made by the Penetration of the Electron Beam into the PMMA Layer. The PMMA Was Then Developed and the Patterned Area Removed Leaving the Bare Silicon Surface. The Lighter Area Is the PMMA Layer Left Intact Which Acts As a Mask So That the Superconducting Material Can Be Evaporated on Top of It. The Darker Region Showing the Outlined Device Is at a Lower Depth Than the PMMA.

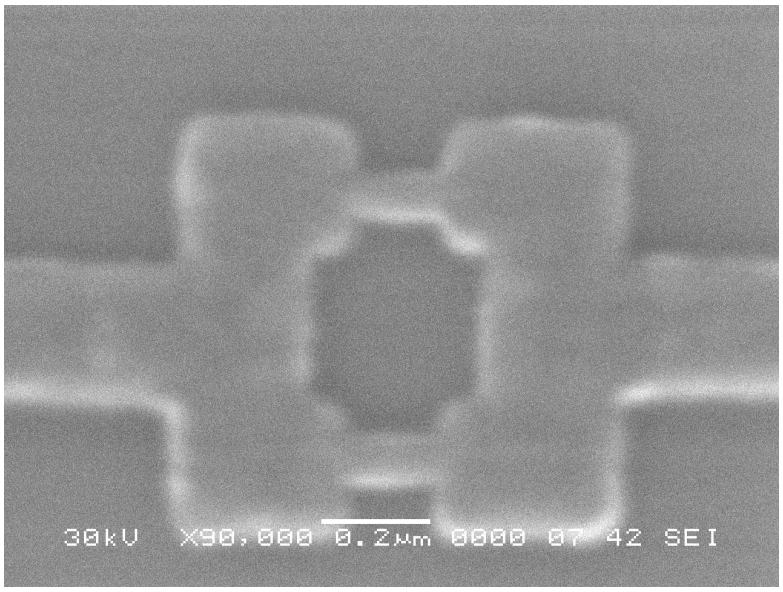

Fig. 14. Micro-SQUIDs Were Successfully Made with Aluminum. Dimensions of the Inner Loop of the Micro-SQUID Are 0.25 μ m x 0.3μ m and Dayem Bridges Are Approximately 40nm - 46nm Wide and 175 nm in Length. (Longer Exposure). Thickness of These Micro-SQUIDs Varied between 20 nm to 50 nm.

connected to each other through collisions as they reach the surface contact area [45]. These initial attachments to the surface are called nucleation sites. As more atoms arrive at the surface, the nucleation sites will fuse together to form islands of deposits and then combine to form a continuous film.

The micro-SQUID formation was tested with three superconductors, Aluminum $T_c = 1.2K$ (Fig. 14), Lead $T_c = 7.2K$ (Fig. 15) and Tin $T_c = 3.72K$, (Fig. 16). The purity of the superconductors varied from 99.9% to 99.9999%. There were 3 variations in the purity of Aluminum (99.9% pellet, 99.999% slug, 99.9999% slug) tested, however the 99.9% purity pellets were the most common for deposition, for tin and lead the purities of 99.999% and 99.9999% were used respectively. The masked samples were coated at rates of approximately 3 Å/sec to 10 Å/sec to achieve a

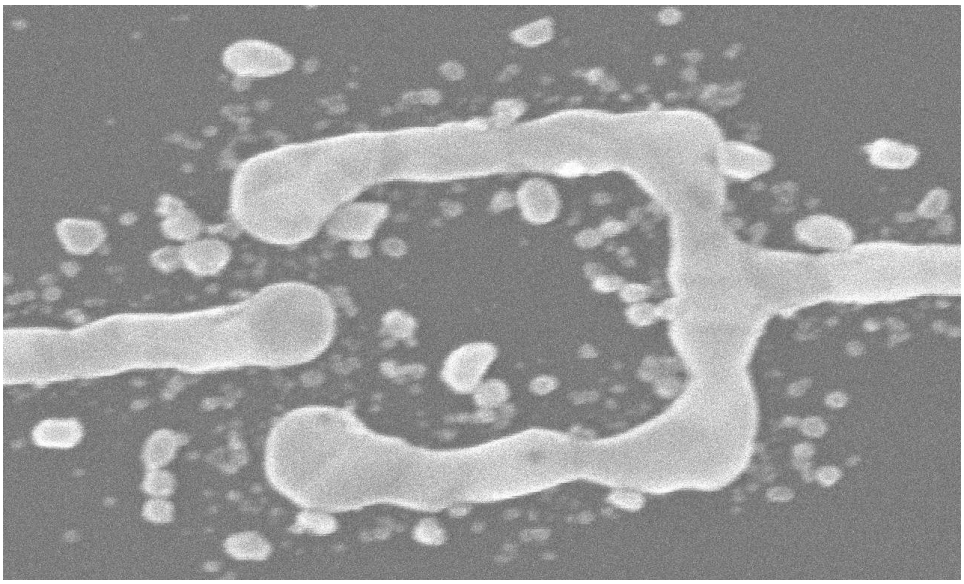

Fig. 15. Junctions Were Difficult to Fabricate with Pb. Dimensions of the Inner Loop of the Micro-SQUID Are 1.0 μ m x 1.0 μ m and Dayem Bridges Are Approximately 50 nm Wide and 250 nm in Length. The Thickness of the Film Is about 50 nm of Lead.

uniform thickness and the vacuum pressure was on average about $4 - 6 \times 10^{-6}$ Torr. An image of a micro-SQUID after the metal deposition process is shown in Fig. 13. The darker regions show the trenches in the PMMA layer formed after penetration of the electron beam. The patterned area was removed by using the MIBK/IPA developer leaving the bare silicon/silicon dioxide surface. The lighter area shows the PMMA layer left intact after development.

The results of the preliminary investigations (see section E of this chapter for fabrication completion overview) indicated that thin films of aluminum could be consistently fabricated with a thickness of 300 Å , while repeated evaporative trials showed that the lead (Fig. 15) and tin (see Fig. 16) films were not electrically continuous for thicknesses below 1000 Åfor the micro-SQUID design. Even though the

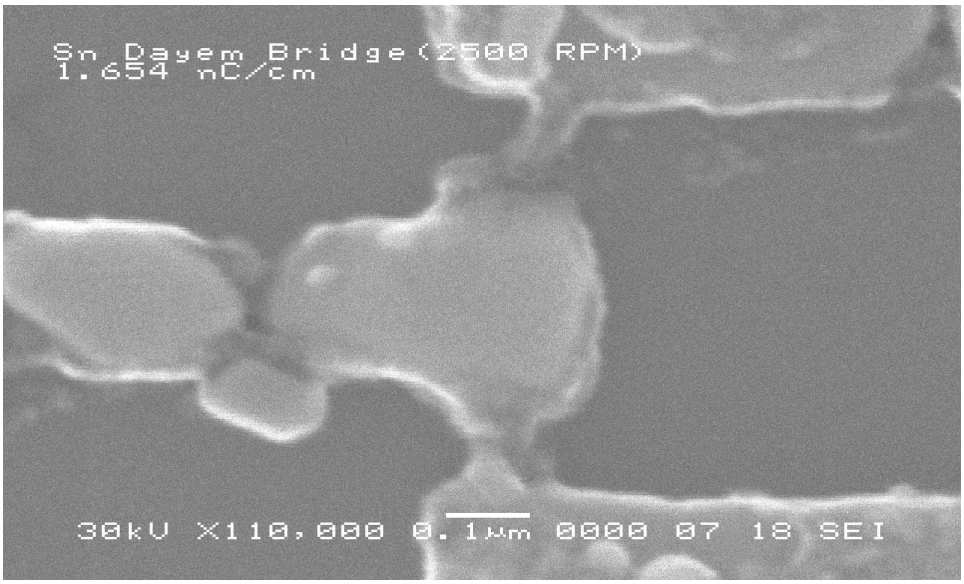

Fig. 16. Thin Film of Sn Micro-SQUID Was Found to Be Non-Continuous. Dimensions of the Inner Loop of the Micro-SQUID Are 1.0 μ m x 1.0 μ m and Dayem Bridges Are Approximately 50 nm Wide and 250 nm in Length. The Thickness of the Film Is About 50 nm of Tin. The Image Also Shows the Spin Speed of 2500 RPM for the PMMA and That a Electron Beam Line Dosage of 1.654 $\frac{nC}{cm}$ Was Used to Create the Dayem Bridges.

aluminum micro-SQUID was easier to fabricate, because of its low transition temperature, it required a complex low temperature apparatus (a dilution refrigerator, see Chapter V for more details) to analyze its properties. This was not ideal for investigating a large sample set of devices because the turn around time for testing could be several weeks.

One alternative for micro-SQUID testing involved the use of an altered aluminum film which had a higher transition temperature than the aluminum micro-SQUIDs tested previously and could be measured in a simpler low temperature measurement device (such as a 1K pot cryostat, see Chapter V for more details). The idea would be to raise its critical temperature by introducing impurities into the metalization (evaporation) process. More precisely, the Aluminum was made "dirty" by introducing a flow of oxygen during heating , this had the potential to increase the critical temperature of the device to values as high as 2.2 K [46]. A low temperature LN_2 evaporator that cooled the sample surface during deposition was also used to examine the film formation of tin micro-SQUIDS. Its primary purpose was to investigate what effect cooling the substrate surface while evaporating had on improving the electrical continuity of the film.

The rectangular CoBr islands were also fabricated using the electron beam lithography, then a thin film layer of CoBr was formed on top of the PMMA surface and then immersed in acetone for the lift off process. Films of about 50 nm thick were formed and viewed under a scanning tunneling microscope. The islands were approximately 100 to 200 nm apart and will eventually be placed on top of a system of micro-SQUIDs for analysis. The system of micro-SQUIDs would be fabricated first on the silicon/silicon dioxide substrate then the islands will be fabricated using the same process of electron beam lithography, evaporation and lift off on top of the micro-SQUIDs.

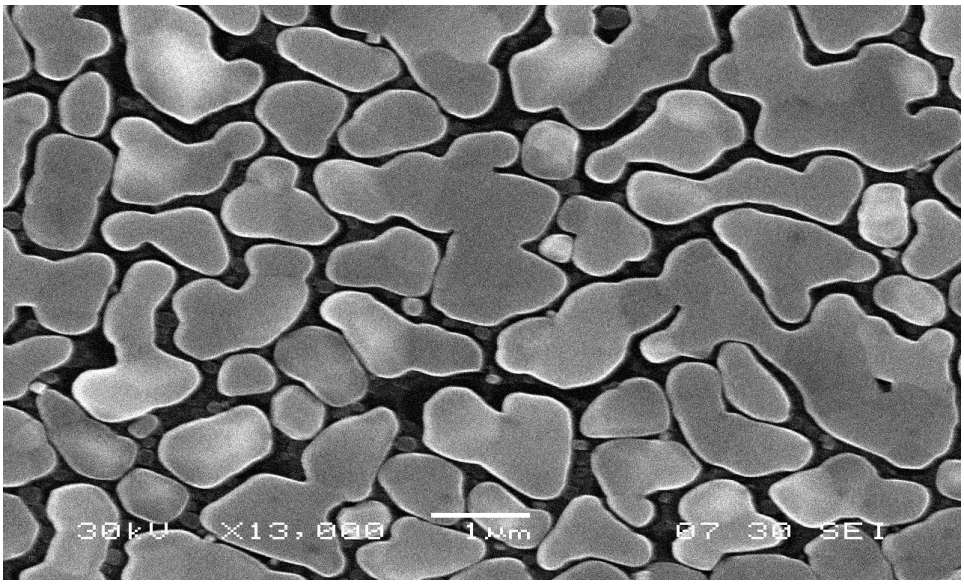

Fig. 17. The Surface of Sn Was Found To Be Non-Continuous Upon Further Investigation

E. Lift-Off and Processing

Once the device is coated to the desired thickness, it is then placed in a bath of acetone which removes the underlying resist and leaves the evaporated material on the silicon dioxide-silicon surface. The sub-micrometer patterned SQUID is then mounted in a dilution refrigerator or a cryostat system and then cooled below its transition temperature where resistance measurements used for experimental observation will be taken. Nano-SQUIDs were created with aluminum and mounted in a dilution refrigerator, very fine junction widths were observed after viewing with a scanning electron microscope.

Systematically reproducible fine features were more common after lift off with aluminum than in both lead and tin. The best discernible features (sharp clearly defined edges, occurred in micro-SQUIDs of loop area close to 300 nm^2. Fig. 14

shows a micro-SQUID of approximately 250 nm wide area by a 300nm long area (note images are widen more than actual dimension due to the imaging process). However, the smallest micro-SQUIDs made with the e-beam lithography system fabricated had a loop area of approximately 150 nm^2.

Lift off of the lead films showed that there seemed to be small clumps of material splashed around the loop (Fig. 15) which indicated adhesion issues. These issues were not observed as often in tin films (Fig. 16) which indicated that it would better adhere to the silicon surface given added adhesion capabilities. Breaks and defects in the film were extremely common, for both lead and tin. Fig. 17 shows the film composition of tin films (approximately 80 nm) deposited at approximately 4.0×10^{-6} Torr, viewed with a scanning electron microscope. It is evident that the film is not continuous and that the possibility of electron transport is small. It was critical that the devices remain planar (two dimensional), so another fabrication method had to be formulated. One method devised was the creation of a thin pre-nucleation layer made from germanium which would act as mechanism for electrical transport(this is discussed further in section F), making it possible to create continuous films for a functional device that would yield reproducible characteristics.

F. Mechanism Implementation

During the fabrication of the tin micro-SQUIDs, several issues consistently showed up after the lift off process. There were conduits along the film causing critical discontinuities along the current transport path. The tin crystallites have to grow to a comparatively large size before they the come in contact with each other [47, 48, 49] because only a relatively small number of nucleation sites are formed on the surface during resistive heating. Therefore, the number of nucleation sites can

be increased significantly by condensing another material on the surface before the tin atoms. In addition, because of their low boiling points, the tin atoms also had a high surface mobility and become electrically continuous at thicknesses of approximately 200 nm [47, 48].

The mechanism chosen to aid in the creation of an electrically continuous thin film was germanium. The germanium atoms had a relatively low surface mobility during deposition, which implied that they had a greater propensity to stay in the location of their original contact with the substrate surface. This produced an area of overlap with the secondary nucleation of the tin atoms, plugging the conduits and creating a path for electron transport in the process. Germanium films within the range of 3nm to 9nm deposited on the silicon/silicon dioxide surface before depositing the tin film at about 4.0×10^{-6} Torr (Fig. 18). With the implementation of the germanium mechanism, the grain size of tin can be controlled by varying the thickness of the germanium film, thus allowing functional tin micro-SQUIDs to be formed at lower thicknesses. As an example, a thin layer of germanium (about 5nm) deposited before the deposition of tin was able to reduce the thickness of the micro-SQUID film from about 200nm to 85nm, with 80 nm being the thickness of tin and 5nm of germanium.

Three different deposition chambers were used to fabricate the Sn-Ge micro-SQUIDs that are analyzed in this dissertation. The micro-SQUID in Fig. 19 was fabricated in a deposition chamber at approximately 4.0×10^{-7} Torr. Measurements consistently showed that the micro-SQUIDS made in the cleanest deposition environments (thin films deposited from 5.0×10^{-6} Torr to 3.6×10^{-7} Torr) had very high critical currents. Over the course of measuring several different samples, it was found that lower critical currents could be achieved with widths of the weak links being fabricated as close to the coherence length of tin as possible.

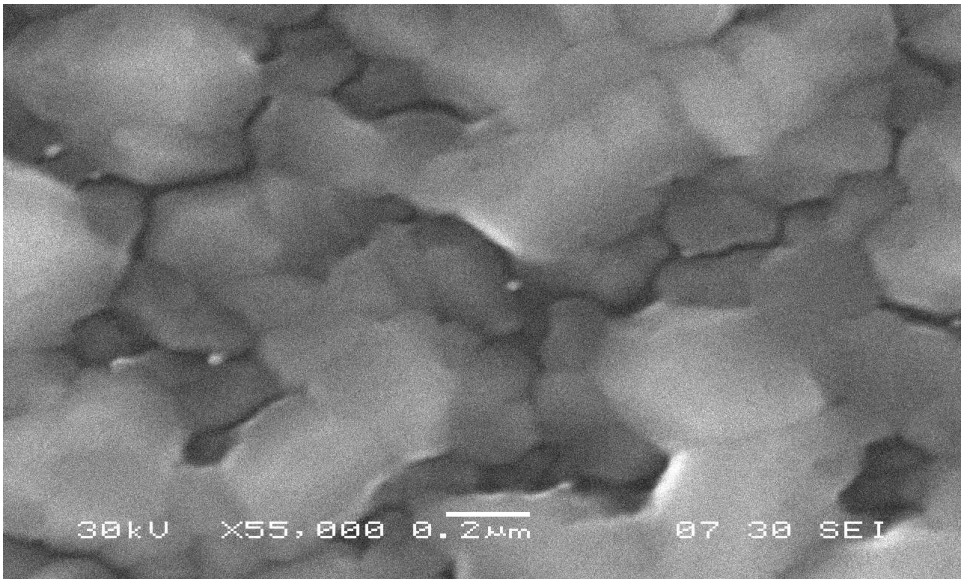

Fig. 18. By Placing a Thin Pre-Nucleation Layer of Germanium before Deposition of Sn Proved to Make the Device Continuous but Not Smooth

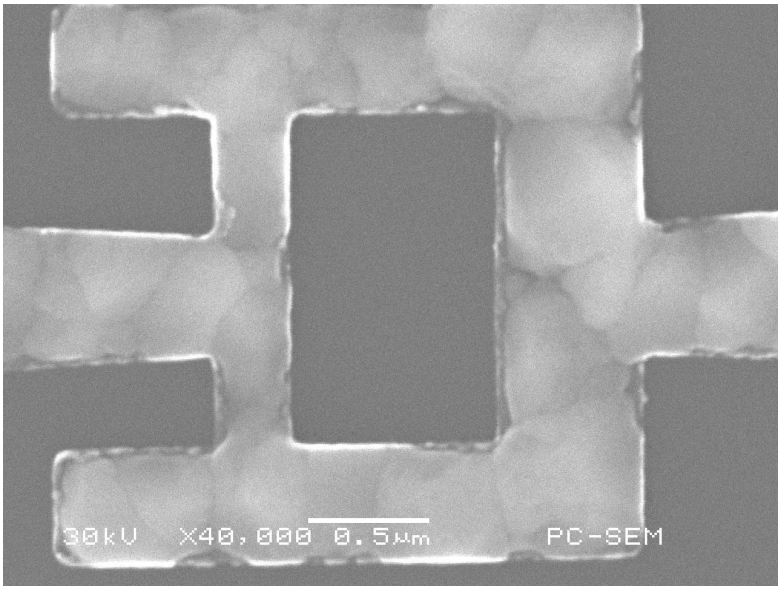

Fig. 19. An SEM Image of a Sn-Ge Micro-SQUID Called 2X (See Chapter VI, Section C for More Details), Showing a Continuous Path for Current Flow. Dimensions of the Inner Loop of the Micro-SQUID Are 1.0 μ m x 1.5 μ m and Dayem Bridges Are Approximately 250 nm Wide and 500 nm in Length. The Thickness of the Film Is About 90 nm of Tin and 9 nm of Germanium.

CHAPTER V

EXPERIMENTAL MEASUREMENTS

The micro-SQUID design incorporates leads (contacts) that were used to make four wire measurements for data analysis, see Fig. 20. Two of the leads were used to pass a current through the device and the other two were used to measure the voltage drop across the weak links and connections. Measurement of the Tin/Germanium micro-SQUIDs were performed using a Physical Property Measurement System (PPMS), and the Aluminum micro-SQUID measurements were performed with a 1K-pot cryostat and a dilution refrigerator. The principle of operation for all three systems are quite similar but more so for the 1K-pot cryostat and the dilution refrigerator which were built in house, the PPMS system is a commercial system built by Quantum Design.

A. Low Temperature Systems

The measurement setup for the 1K cryostat and the dilution refrigerator had the miniaturized SQUID in series with a reference resistor of 100 kΩ or 1 MΩ and an AC lock-in amplifier (7 Hz signal) that was used to supply the voltage that drives the current through the circuit. The current through the circuit was taken to be constant because the reference resistor was large compared to the micro-SQUID (30 Ω - 100 Ω). Once the temperature of the superconducting device was below it's critical temperature, the current was increased from zero to its critical point. The voltage across the device was then sampled for it's corresponding critical current value and the results recorded.

The 1K-pot Cryostat system operates by pumping the vapor above a liquid ^{4}He bath out of the system with a mechanical pump thereby removing the more energetic

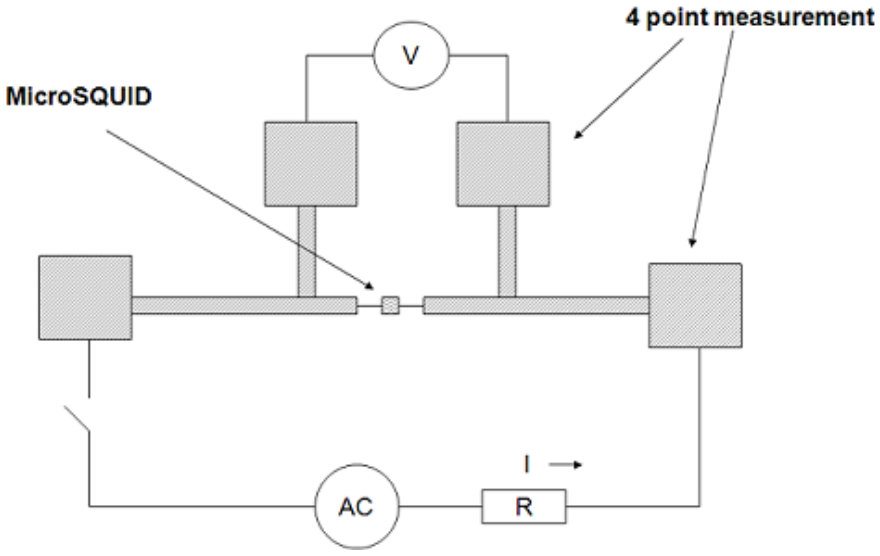

Fig. 20. Diagram of a Basic 4 Wire Measurement Setup. The Micro-SQUID Is in Series with a Reference Resistor and an AC Lock-in Amplifier.

particles from the liquid containment system. As a result, the average kinetic energy of the fluid is reduced and the temperature of the system drops. A small 1K pot is connected to the pumping line that sits inside a vacuum can that is completely immersed in the ^{4}He bath during the cooling process. Liquid ^{4}He is transferred from the bath to the 1K-pot through a tube attached through the top of the vacuum can. Devices are mounted on a sample holder with good thermal conductivity and the holder in turn is connected to the bottom of the pot. The cryostat system has shown (under good conditions) to get to 1.1 K, which is just below the critical temperature of aluminum.

Even though the thin films of aluminum had a slightly higher transition temperature than in bulk form (ranging approximately from about 1.22 K to about 1.27 K) it was just barely low enough to see any temperature transition and was not low enough to observe the necessary critical current - magnetic field modulated charac-

teristics. For this reason, it was necessary to increase the critical temperature of the aluminum film to further the study of these aluminum micro-SQUID devices (This was discussed in Chapter IV, section D as one of the options considered in our testing phase). By introducing oxygen in the evaporation chamber during the aluminum deposition process one can greatly increase the critical temperature of the device. Some studies have shown than it can increase to as high as 2.2 K [36]. micro-SQUIDs that had critical temperatures of 1.4 K - 1.5 K were obtained from these investigations, however, no oscillations of the critical current with applied field was detected using these devices. One reason for this could be that the oscillations were very tiny close to T_c and were not picked up by signal detector.

The dilution refrigerator, in comparison to the 1 K-Pot Cryostat, uses the dilution of ^{3}He in ^{4}He (called a ^{3}He-^{4}He mixture) to cool the system further in addition to the process described above [50, 34, 51]. Successful operation of this system requires a basic understanding of three additional components, the still, heat exchangers and mixing chamber. Each component sits on separate stages below the 1K pot to prevent heat leaks from external systems. The still is attached to the 1K pot by two circulation lines (a pumping line and a return line) called capillaries. The mixing chamber and heat exchangers, which are below the still, are also in direct contact with the still by the capillaries, with the heat exchangers sitting on a stage between the still and the mixing chamber.

For system operation, the ^{3}He gas and ^{4}He gas are mixed and then circulated through a liquid ^{4}He bath. After several circulations, the mixture is liquefied [50, 34]. As its name suggests, the mixing chamber is a container that allows for the mixing or interaction of ^{3}He and ^{4}He. Once the temperature in the dewar drops below 600 mK and the concentration of ^{3}He in ^{4}He in the chamber is greater than 6%, the mixture will separate into two distinct phases [50, 34, 51]. These two phases of

helium, one being the ^{3}He rich phase (almost pure ^{3}He) and the other being the ^{3}He dilute phase (mostly ^{4}He but will contain about 6% of ^{3}He) causes a diffusion process to occur across the phase boundary because the concentration of ^{3}He in the dilute phase cannot be less than 6%. By pumping on the dilute ^{3}He phase, the ^{3}He atoms from the ^{3}He rich phase are forced to evaporate across the phase boundary to restore equilibrium, causing the temperature to be lowered in the process. The ^{3}He atoms are still energetic in the upper phase and diffuse across the phase boundary downward to the dilute phase breaking the bonds between the ^{3}He atoms. As a result, the mixing chamber is cooled and becomes the coldest place in the refrigerator. Energy is taken up from the surrounding environment to allow this evaporation or diffusion process [50, 34, 51]. The heat exchangers aid in the removal of the ^{3}He atoms from the dilute phase and will enable the ^{3}He atoms to diffuse more effectively across the phase boundary. This removal of the ^{3}He atoms reduces the density of the ^{3}He in the dilute phase. The ^{3}He is removed from the still and is then returned to the mixing chamber through a return line in a closed circulating pumped system which keeps the sample continuously cooled when the mixture is circulating.

When a sample was prepared and ready for testing, it was wired to a stage holder and attached to the system. To prevent radiant heating of the sample space, the sample was enclosed inside a radiation shield. It was then subsequently enclosed in a vacuum can that was later immersed in a bath of liquid ^{4}He. This vacuum can was filled with ^{3}He exchange gas to aid cooling of the sample to 4.2 K. A magnet was then attached to the vacuum can, the sample orientation allowed for the applied magnetic field to be perpendicular to the sample plane. After all peripheral systems were attached (i.e. helium fill line extension, level sensors, heater and electronics), a dewar used to facilitate the liquid ^{4}He bath enclosed everything within. The system is first cooled to 77 K by filling the dewar with liquid nitrogen. The liquid nitrogen

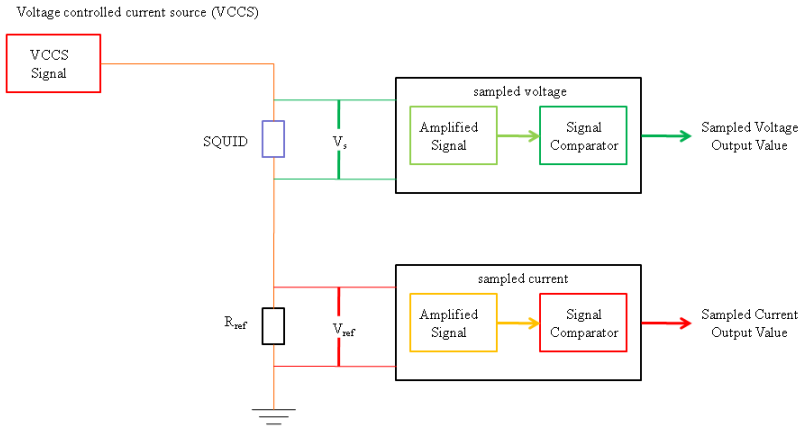

Fig. 21. Circuit Diagram for Critical Box Measurement Across Sample. The Critical Current Box Is an Electronic Device that Captures a Critical Current Value that Corresponds to a Voltage Specified in Its Memory Called the Sampled Voltage Value.

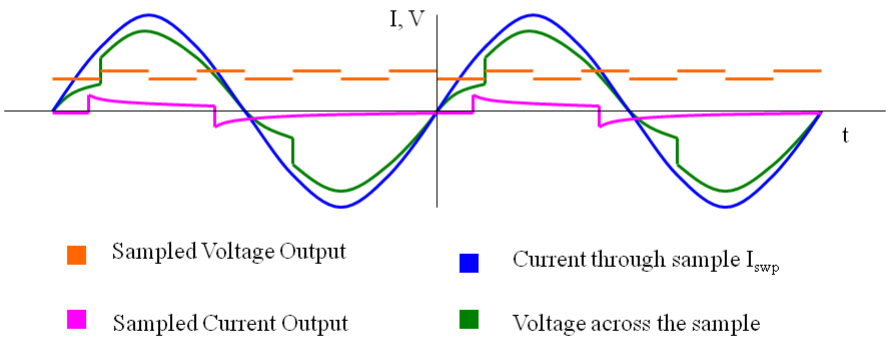

Fig. 22. Current and Voltage - Time Graphs As Seen on an Oscilloscope. The Sampled Output for the Voltage and Current Output Are Linked and Are Acquired Simultaneously. As the Voltage Across the Sample Oscillates it Is Automatically Recorded for Every Instance Where Its Value Corresponds to the Sampled Voltage Value.

was removed by back transfer and the dewar flushed with helium gas. Once the dewar has been properly flushed, liquid ^{4}He was transfered into the dewar. A mechanical pump was then used to pump the vapor that accumulates above the liquid ^{4}He bath out of the system.

Two Princeton Applied Research (PAR) model 124A lock-ins were used to take resistivity measurements for the system. The critical current measurements in the presence of an applied magnetic field were recorded using a critical current box, and Fig. 21 illustrates how the output signal is obtained. The critical current box is an

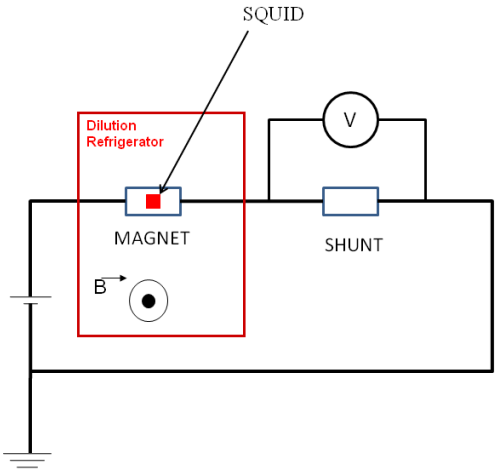

Fig. 23. Magnet-Shunt Resistor Circuit Diagram. The Magnet that Enclosed the Sample for Measurement Is Placed in Series with a Shunt Resistor in the Dilution Refrigerator.

electronic device that captures a critical current value that corresponds to a voltage specified in its memory called the sampled voltage value. As the voltage across the sample changes in response to a magnetic field, the sample voltage value maintained in memory records it and transmits it to a log file to be accessed for analysis later and converted to the critical current value. The four leads of the micro-SQUID (two voltage and two current leads) are connected directly to the box. Current is supplied to the critical current box from the AC lock-in amplifier and the voltage across the sample is viewed on an oscilloscope for monitoring its behavior, see Fig. 22. Once the sample voltage value had been set on the critical current box, the value of the current was automatically recorded for every instance where this voltage value occurred when the magnetic field is applied to the micro-SQUID.

The magnetic field applied to the micro-SQUID was recorded using a shunt resistor. A shunt resistor is a high precision resistor that is used to measure the current flowing through the circuit set up. This circuit simply entails placing the

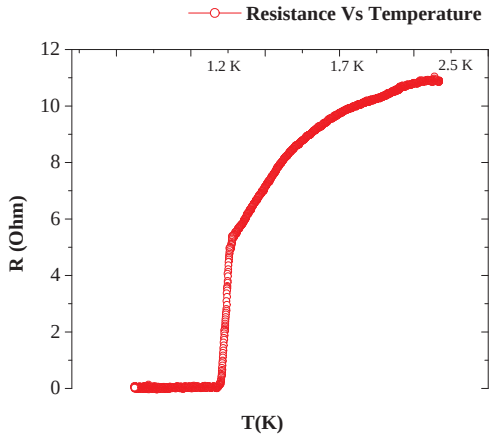

Fig. 24. Measurement of Resistivity with Temperature for an Aluminum micro-SQUID. The Critical Temperature Was Found to be 1.2 K.

magnet in series with this shunt resistor, see Fig. 23. The current flowing through the circuit can be easily found using Ohm's law ($I_{MAG} = \frac{V_{SHUNT}}{R_{SHUNT}}$). The applied magnetic field generated is proportional to the voltage drop across the shunt resistor ($B = \gamma V_{SHUNT}$). For these low temperature experiments, two shunt resistors were used. The first was calibrated such that the voltage drop across it was 50 mV for 15 A ($\frac{1}{300}$ Ω) and the second was calibrated such that the voltage drop across it was 50 mV for 1.5 A ($\frac{1}{30}$ Ω)

The dilution refrigerator system base temperature recorded was about 50 mK. Aluminum becomes superconducting at about 1.2 K. It has been found that the critical current value increases as one lowers the temperature below the critical temperature of Aluminum [1]. For those experiments, the temperature of the Aluminum micro-SQUID was lowered from 1.2 K down to 0.2 K and measurements taken of the critical current as a function of applied magnetic field. The shape of the modulated graphs became sharper and more distinct with the decrease in temperature [1]. Thus,

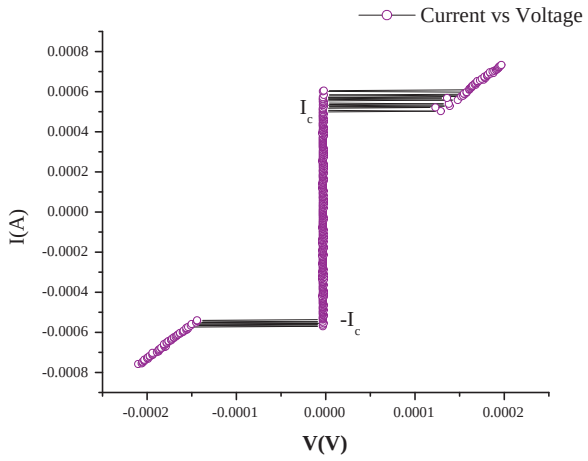

Fig. 25. Graph of Current vs Voltage in Zero Field for an Aluminum micro-SQUID. The Multiple Lines Show the Different Critical Current Values Recorded as the micro-SQUID Transitioned from a Normal State to a Superconducting State.

there was a need for a system that can be systematically cooled to temperatures below 1 Kelvin.

The critical temperature of the aluminum thin film micro-SQUID as shown in Fig. 24 shows the same value as that of bulk aluminum by having its resistance fall sharply to zero at around 1.2 K. This sample had a thickness of approximately 400 Å. For the results shown in Fig. 25, the hysteretic current-voltage characteristic of the micro-SQUID below its critical temperature was in close agreement with the behavior reported by Hasselbach and Wernsdorfer [21, 1]. Here, the current was increased (from zero) past its critical current value I_c, the device goes from a superconducting state to a normal state, producing a normal state resistance. With the generation of this resistance, energy is given off in the form of heat, causing the temperature of the device to be raised. Once the current is decreased the device retains this normal state

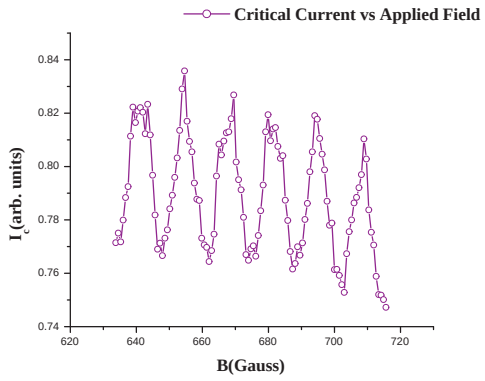

Fig. 26. Critical Current Dependence on an Applied Magnetic Field for a One Micron Loop Aluminum Micro-SQUID. The Modulated Dependence Occurred for Every 13 Gauss.

resistance until it has passed its critical current value I_c.

Fig. 26 shows the critical current dependence on the applied magnetic field for a one micron micro-SQUID loop cooled to a temperature of 0.6 Kelvin. These data were obtained by utilizing low temperature electronics on the dilution refrigerator and the critical current box discussed earlier in this Chapter(also see Fig. 21 and Fig. 22). The modulation repeated at approximately every 13 gauss (making the flux 13 gauss μm^2). However, theory suggests that the modulation repeats at every 20 gauss (giving a flux quantum of 20 gauss μm^2). The discrepancy may be due to field errors created by remanence and flux motion in the superconducting magnet and to the penetration into the inner sides of the loop by the magnetic field, see also Chapter VI.

B. Characteristic Measurements

For our analysis of the tin germanium (Sn-Ge) micro-SQUIDs the resistivity measurements, the non-linear current-voltage characteristics, and critical cur-

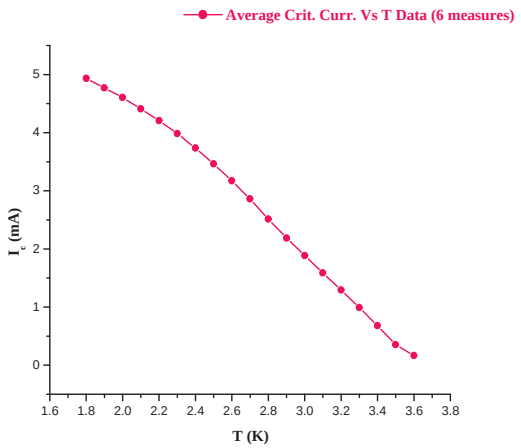

Fig. 27. Measurement of Critical Current with Change in Temperature for a Sn-Ge Micro-SQUID. Six Different Instances of Measurements Were Recorded and Averaged.

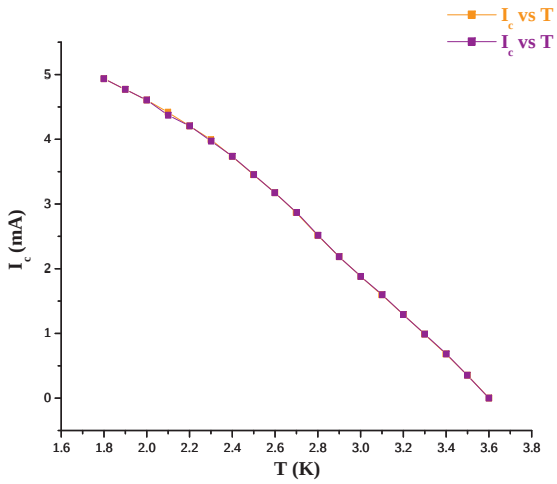

Fig. 28. Values of Critical Current Consistent (Reproducible) for Sn-Ge Micro-SQUID with Dimensions 1.0 μm x 1.5 μm.

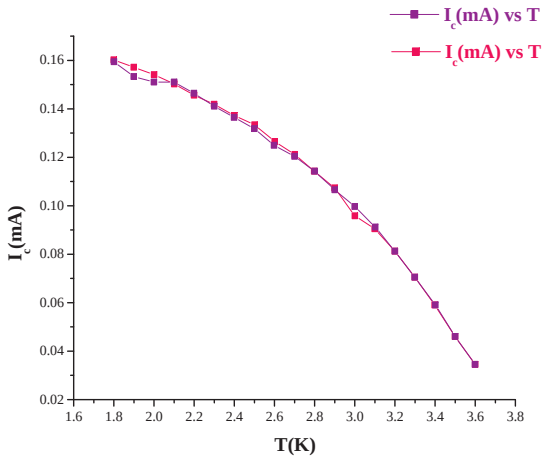

Fig. 29. Values of Critical Current Consistent for Repetitive Measurements and Changing Temperature for Sn-Ge Micro-SQUID with Dimensions 0.5 μm x 1.5 μm.

rent measurements were recorded using the physical property measurement system (PPMS). The tin-germanium micro-SQUIDs showed that the critical current value increased with a decrease in temperature (Fig. 27, Fig. 28 and Fig. 29), and a modulated critical current value with applied field (Fig. 30, Fig. 31).

The resistivity measurement, Fig. 33 was taken from 300 K to 1.8 K for a current of 10 μA. As the temperature gets close 3.65 K for the Sn-Ge micro-SQUIDs there is a sharp drop to zero, which is consistent with the behavior for superconducting films. The sample resistivity $\rho = \frac{VA}{Il}$ can be calculated from Ohm's law. V is the potential drop across the sample and I is the current through the sample. The voltage lead separation varied between 2 μm and 20 μm and the cross sectional area, A was calculated using the cross sectional area dimensions of the Dayem bridges. The critical temperature was on average slightly lower than that of bulk tin (3.72 K). Fig. 32 shows an enhanced view of the behavior of the resistivity just below the

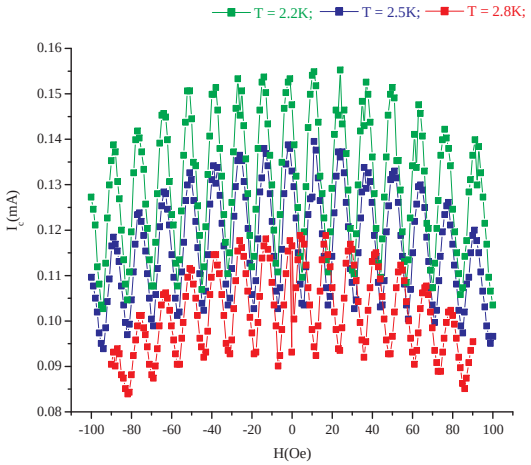

Fig. 30. Critical Current Modulations Were Observed for the Sn-Ge Micro-SQUIDs When a Magnetic Field Was Applied at Temperature Values 2.2 K, 2.5 K, and 2.8 K. The Thickness of Tin was 90nm and for Germanium Was approximately 9nm.

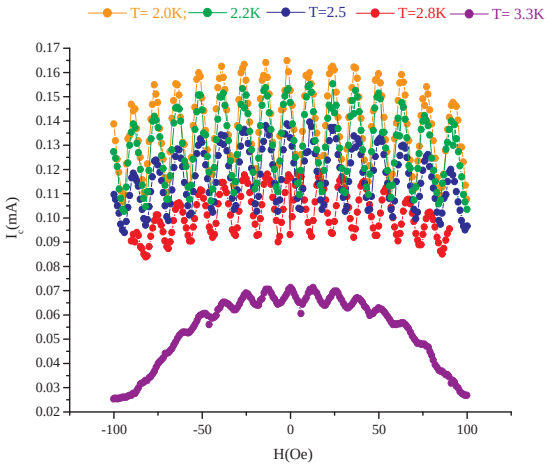

Fig. 31. Critical Current Modulation with Applied Field for Temperatures 2.0 K, 2.2 K, 2.5 K, 2.8 K, 3.3 K. The Thickness of Tin Was 90nm and for Germanium Was Approximately 9nm.

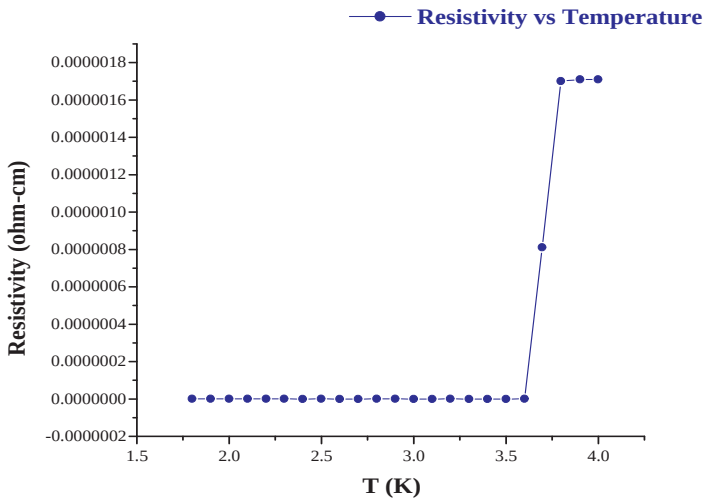

Fig. 32. Enlarged View of Resistivity Behavior Below Transition Temperature

transition temperature. There is a clear distinction in values of resistivity around 3.65 K, which clearly shows that the tin properties overshadow any effects that could be due to any tin germanium interactions.

For critical current measurements, the current through the sample was increased by a digital signal processor (DSP) in small discrete steps to a specified maximum current. As the current is increased (ramped up a little at a time), the voltage across the sample is monitored. When the superconducting material of the device becomes resistive (reaches its critical current limit), a potential difference is generated across the sample. The system averages over this potential difference for a designated period of time to filter out noise that could interfere with the intended signal. Once the current value that corresponds to the sampled voltage point is found the current was shut off and the point where the ramp was stopped was recorded. Critical current measurements were recorded using the shortest response time 40 μs, however it

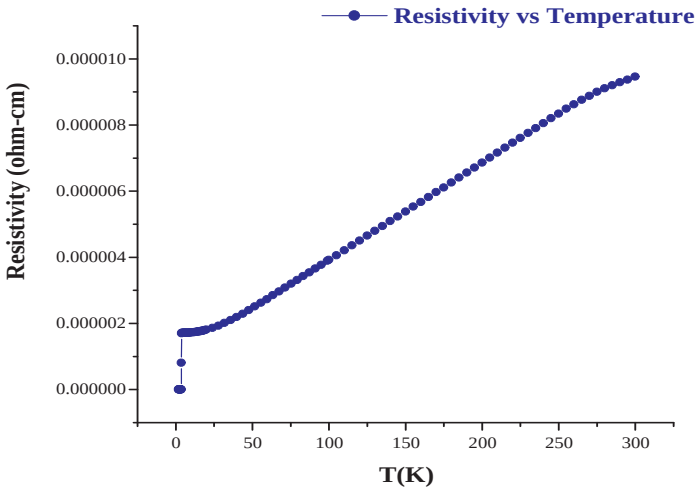

Fig. 33. Resistivity Behavior from 300 K to 1.8 K

was found that the noise contributions of some of the devices could be minimized if multiple measurements of each critical current value were obtained and averaged.

Several Sn-Ge micro-SQUIDs were fabricated with different thicknesses ratios of germanium and tin to test the limits of the device functionality. The micro-SQUID shown in Fig. 34 had a 10:1 ratio of tin to germanium. The electron transport properties of the device was found to be operational even with a very rough surface and was able to generate an observable critical current modulation with magnetic field. It was observed that increasing the thickness of germanium above 9 nm did not improve the smoothness or continuity of the film, the roughness was observed (held at a steady state) for thicknesses of tin, between 80 nm to 150 nm and thicknesses of germanium from 5 nm to 19 nm. The Sn-Ge devices had micro-SQUID loops of approximately 0.675 μm^2. Modulations of the critical current were observed at approximately every 12.0 Oe - 13.5 Oe for various temperatures (see Fig. 30).

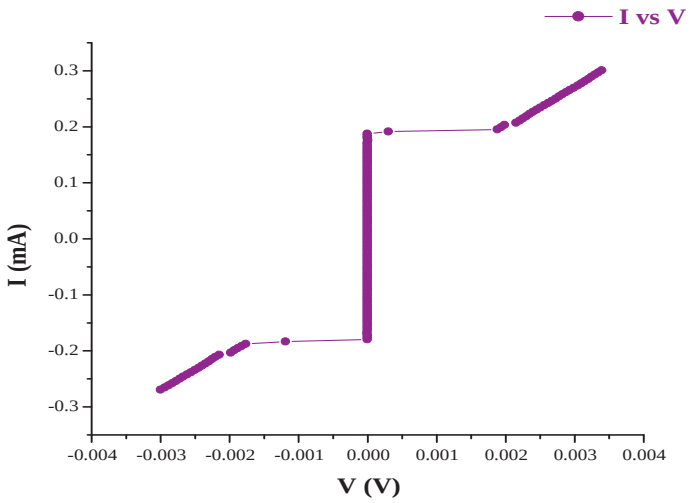

Fig. 34. Current Voltage Characteristics for Tin Germanium Micro-SQUIDs Sn = 90 nm, Ge = 9 nm

For values closer to the transition temperature there was a significant drop off (attenuation) in the critical current modulation (see Fig. 31) faster (smaller changes in field range) than at lower temperatures (Fig. 30). It was observed that for a constant change in temperature ΔT = 0.1 K, the change in critical current ΔI_c grew larger moving away to temperatures below the transition temperature. To investigate this observation further, the critical current was obtained for temperatures below the critical temperature in decreasing increments of 0.1 K, (see appendix A). Fig. 27 also shows 6 averaged measurements for the critical current with respect to temperature. The values were swept from 3.6 K to 1.8 K then from 1.8 K to 3.6 K, three times then averaged. The results were in line with the individual results obtained for the Sn-Ge micro-SQUID which can be seen in appendix A. Other Sn-Ge micro-SQUIDs under testing showed a sharper change in the critical current value for changing temperature (Fig. 29) which could be attributed to optimal conditions being present within the

device, such as their weak links being very close to or slightly lower than the coherence length of the superconductor and having a good deposition film for current transport.

CHAPTER VI

RESULTS AND ANALYSIS

The ultimate goal in the fabrication of a micro-SQUID is to achieve the best sensitivity (critical current response to the changing magnetic field) of the device for measurement. The sensitivity was found to be reduced when the coherence length of the thin film is small. For example, niobium has a small coherence length 38 nm and shows very small modulation depths [1, 21, 19]. The modulation depth is defined as the difference between the maximum point and minimum point of an oscillation. It has been shown that the optimum operating condition for a micro-SQUID is $2LI_c \lessapprox \Phi_0$, where L is the geometrical inductance of the micro-SQUID and I_c the critical current of the two junctions [15, 14, 27, 28].

As we have seen from Chapter V, each micro-SQUID undergoes rigorous testing to ensure that it exhibits typical micro-SQUID like behavior demonstrated in previous experiments [1, 20, 52]. Each micro-SQUID device was tested for evidence of a transition temperature (i.e. its critical temperature, see Chapter V), a current-voltage relationship (Chapter V), its critical current - temperature relationship (Chapter V) and most importantly its critical current - applied magnetic field relationship (Chapter V) since this is the clearest indication of periodic discretized behavior as discussed in Chapter III.

The superconducting material that was the focus of analysis was Tin(as discussed in Chapter IV). The tin micro-SQUIDs utilized a low temperature LN_2 evaporator that cooled the sample surface during deposition. This was done to investigate if the substrate surface cooling would improve the continuity of the thin film (making it less disjointed due to a propensity for clustering). An adhesion layer (pre-nucleation layer) approach was also undertaken to compare with the low temperature evaporation

method. The results obtained by adding the germanium pre-nucleation layer proved statistically more successful than the low temperature LN_2 evaporation method, consistently producing more continuous samples than the low temperature evaporation method, as discussed in Chapter IV. The success rate for fabrication of micro-SQUIDs with an pre-nucleation layer was approximately 57.4%, while that of the LN_2 evaporation method was approximately 16.7%. As a result, the tin germanium (Sn-Ge) micro-SQUIDs became the focus of the experimental analysis.

A. Device Geometry and Inductance

Throughout the course of the investigation, the dimensions of the tin-germanium micro-SQUIDs in the micrometer regime were gradually reduced to the sub-micrometer regime. Table II shows the various loop dimensions that were investigated with the tin germanium pre-nucleation layer with their corresponding areas and estimated theoretical geometric inductances. The geometric inductances for micro-SQUIDs with equal widths and lengths were estimated from

$$L = \frac{5\mu_0}{4}(\frac{P}{4}) \tag{6.1}$$

where P is the inner perimeter of the micro-SQUID [1, 16, 53] and μ_0 is the permeability of free space. Estimations for micro-SQUIDs where the lengths and widths were not equal (rectangular micro-SQUIDs) were found using

$$L = \frac{5\mu_0}{4}(\frac{P_A}{4}) \tag{6.2}$$

where

$$P_A = \frac{l^2 + w^2}{l + w} \tag{6.3}$$

Table II. Dimensions and Geometric Inductances of Tin-Germanium Micro-SQUIDs with the Critical Current Limit for Optimized Sensitivity Estimated from Their Corresponding Dimensions.

Group	Dimensions (μm x μm)	Area (μm^2)	Geometric Inductance (pH)	Critcal Current (mA)
I	10 x 10	100	3.93	0.168
I	3 x 3	9	1.18	0.559
I	2 x 2	4	0.785	0.838
I	1.5 x 1.5	2.25	0.589	1.12
II	1.5 x 1.0	1.5	0.511	1.29
II	1.0 x 1.4	1.4	0.484	1.36
II	0.5 x 1.4	0.7	0.457	1.44
II	0.5 x 1.0	0.5	0.327	2.01
III	0.4 x 1.4	0.56	0.463	1.42
III	0.3 x 1.4	0.42	0.474	1.39
III	0.25 x 1.4	0.35	0.481	1.37
III	0.2 x 1.4	0.28	0.491	1.34
III	0.1 x 1.4	0.14	0.516	1.28
IV	0.5 x 0.5	0.25	0.196	3.35
IV	0.5 x 0.4	0.2	0.179	3.68
IV	0.5 x 0.2	0.1	0.163	4.05
IV	0.5 x 0.1	0.05	0.170	3.87

is the weighted average for the dimensions of the rectangular loop. Note that equation 6.1 can be obtained from equation 6.2 by setting the lengths and widths equal to each other. Each dimension was categorized in one of four groups, ranging from the group with the largest areas (Group I) to the group with the smallest areas (Group IV). The geometric inductances were used to forecast the maximum or threshold critical current that should be generated to optimize the micro-SQUID's sensitivity and avoid magnetic hysteresis within the device. Further analysis [27] into this magnetic hysteresis avoidance constraint would show that there is a slightly stronger bound on the screening parameter,

$$\beta = \frac{2LI_c}{\Phi_0} \leq \frac{2}{\pi} \tag{6.4}$$

limiting the value of the critical current to

$$I_c = \frac{\Phi_0}{\pi L} \tag{6.5}$$

The widths of the Sn-Ge micro-SQUID Dayem bridges ranged from 70 nm to 320 nm and their lengths varied from about 300 nm to 4000 nm. The large variation of the Dayem bridge lengths was done to account for the size of the micro-SQUID loop. There have been discussions suggesting that a reduction in the thicknesses and widths of the bridges lead to a decrease in the mean free path and thus a reduction in the coherence length [1]. However, it has also been shown that small coherence lengths lead to a diminution in the micro-SQUID's sensitivity [1, 52]. We can compensate for this diminution by creating thicker films which would increase the mean free path of the device and thus increase the coherence length and improve the micro-SQUID's sensitivity [1, 19]. The coherence length is an important consideration in the micro-SQUID analysis since the modulation depths are maximized if the bridge lengths are

less than or equal to the coherence length [1, 52, 19].

The thickness of the germanium pre-nucleation layer was also investigated to ascertain the thinnest value that would give the most consistent continuous films results as well as having little or no interaction with the tin thin film. Germanium pre-nucleation layers in the range of 7 nm to 12 nm were able to consistently support continuous tin films for the analysis. Thicknesses of Tin ranged from 85 nm to 140 nm, however the best results were obtained for devices that had thicknesses of approximately 90 nm.

B. Characteristic Analysis

Once the device enters the superconducting regime (in our case below 3.72K for bulk tin), the current-voltage relationship is obtained and the critical current value can be clearly found from the devices I-V Graph. As we have seen from our investigations in Chapter V, the I-V relationship for a Group II micro-SQUID (1.4 μm x 0.5 μm), has a critical current value of about 0.17 mA. Other values of critical currents varied in range from about 0.001 mA to 7.5 mA depending on temperature (the highest values occurring at the lowest temperatures as reported from Chapter V). This demonstrates that these Sn-Ge devices have the capability of carrying very large currents before becoming normal (producing a resistance when it had none before).

As the current is increased from zero, the micro-SQUID moves from the superconducting state to the normal state (a state where ohmic behavior was found). One example of this occurrence is represented in Fig 35, where the critical current occurred at approximately 3.22 mA for a temperature of 2.8 K. The ohmic slopes are generated as a result of the current exceeding the critical current, moving the device more into the normal state. Moreover, these resistive slopes are due to the dissipation

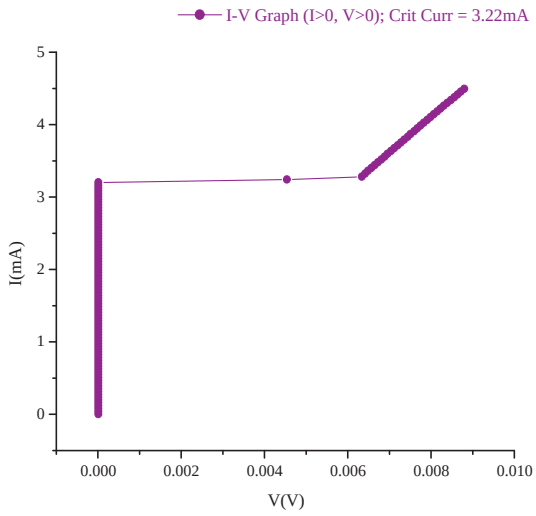

Fig. 35. I-V Graph of a Group II Sn-Ge Micro-SQUID That Has a Critical Current of Approximately 3.22 mA for a Temperature of 2.8 K. Ohmic Behavior Was Found as the Micro-SQUID Moves from the Superconducting State to the Normal State.)

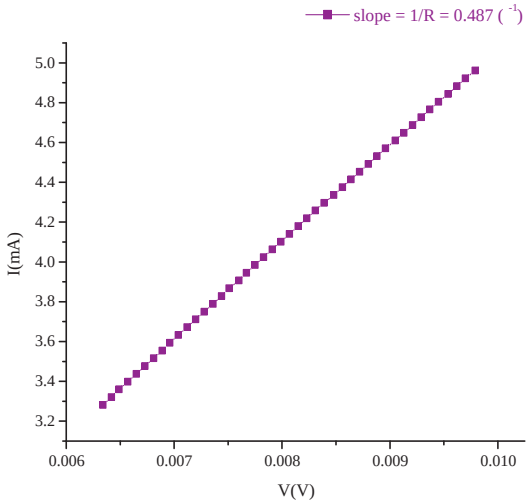

Fig. 36. Normal Resistance Obtained from Gradient of I-V Graph. The Effective Normal Resistance for the Micro-SQUID in Fig. 36 Was Approximately Equal to 2.05 Ω.

of energy in the loop initially caused by the heating of the bridges then the entire loop by gradually increasing the current through the device.

As a consequence of continually increasing the current, a constant voltage step was observed and a critical current value registered, just before the micro-SQUID became resistive ($I > I_c$). Calculation of the normal resistances generated from the resistive slopes of the Sn-Ge micro-SQUID devices showed that they varied between 0.002 Ω and 2.5 Ω. Fig. 36 shows the inverse of the normal resistance ($\frac{1}{R_n}$) calculated from the gradient of the slope of the I-V graph from Fig. 35. The effective normal resistance for the micro-SQUID in Fig 36 was approximately equal to 2.05 Ω.

The Hysteretic I-V characteristic behavior of Sn-Ge micro-SQUIDs can be clearly seen from Fig. 37, which shows the results of a Sn-Ge micro-SQUID whose current was increased from zero to a value past its critical current then back down to zero.

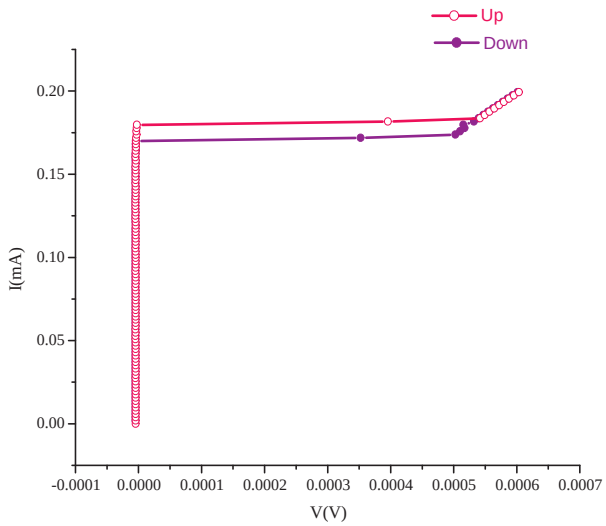

Fig. 37. Hysteresis Found in Micro-SQUID's I-V Graphs. The Current Was Increased from Zero to a Value Past Its Critical Current Then Back Down to Zero.

This showed that there are distinct paths taken when entering the normal state and returning to the superconducting state. We can see that as a corollary of the thermal heating brought on by the micro-SQUID hysteresis, that the value of the critical current upon return to its superconducting state was smaller than the critical current value as it entered the normal state [1].

Observance of the critical current behavior versus temperature in zero field was very essential for micro-SQUID optimization. As one enters the superconducting regime the maximum critical current value that can be achieved will be unknown and will vary with each device. An estimate of this maximum critical current value of the micro-SQUID is usually made at the start of the experimental analysis using the I-V graph and Table II, so that the data can be captured correctly and adjusted if the critical current exceeds the estimate. As we have seen from Chapter V, the

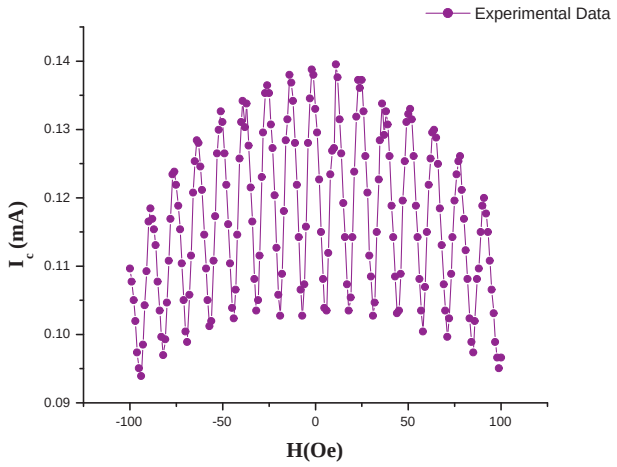

Fig. 38. Experimental Data of the Critical Current Modulation for Group II micro-SQUID Taken at 2.5 K. The Junctions Used for This Device Were Dayem Bridges with Lengths Approximately Equal to 2 ξ_0 and Widths Equal to ξ_0. Dimensions of the Inner Loop of the micro-SQUID are 0.5 μ m x 1.5 μ m and the Thickness of the Film is About 90 nm of Tin and 9 nm of Germanium.

critical current increases with temperature. Devices measured close to but below the transition temperature had average critical current values close to 0.001 mA for most operational micro-SQUIDs (between 3.65K to 3.68K).

The experimental data obtained from the Sn-Ge micro-SQUID devices showed that their critical currents oscillated in response to a changing applied magnetic field. Fig. 38 shows the results for a micro-SQUID that was fabricated with dimensions 1.4 μm x 0.5 μm. The junctions used for this device were Dayem bridges with lengths approximately equal to 2 ξ_0 which are considered long Josephson junctions, see [1, 54]. The triangular shape of the oscillations were a result of the size of the Dayem bridges being approximately equal to the coherence length ξ_0 of tin, that is $\xi_0 = 230$nm. The modulation depth $\Delta I_c = I_{cmax} - I_{cmin}$ was approximately 0.0375 mA. The period of

Table III. Experimental Values for the Inductances and the Screening Parameter of Tin-Germanium Micro-SQUIDs for Critical Current Taken in Zero Field.

Group	Dimensions (μm x μm)	Area (μm^2)	Inductance (pH)	Screening Parameter (no units)
I	1.5 x 1.5	2.25	1.46	14.2
I	1.5 x 1.0	1.5	1.74	12.1
II	1.4 x 1.0	1.4	1.17	17.4
II	1.4 x 0.5	0.7	3.53	6.84
II	1.4 x 0.4	0.56	2.87	15.9
III	1.0 x 0.5	0.5	3.97	9.67
III	1.4 x 0.3	0.42	2.49	19.8
III	1.4 x 0.25	0.35	2.38	12.28

oscillation at various temperatures for this device was found to be about 13.0 Oe. This value was not in agreement with the established theoretical models which predicted the period of oscillation to be closer to 29.5 Oe.

The experimental inductance of the micro-SQUID was estimated using the relation

$$\frac{\Delta I_c}{I_c} = \frac{1}{(1+\beta)} \tag{6.6}$$

where

$$\beta = \frac{2\pi L I_c}{\Phi_0} \tag{6.7}$$

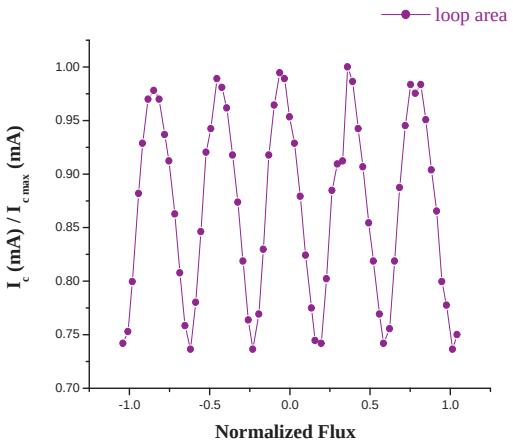

Fig. 39. The Actual Loop Area Normalized Contribution of the Critical Current Modulation Due to the Applied Flux. The Flux Enclosed by the Loop Is Less Than One Half of a Flux Quantum. The Junctions Used for This Device Were Dayem Bridges with Lengths Approximately Equal to 2 ξ_0 and Widths Equal to ξ_0. Dimensions of the Inner Loop of the Micro-SQUID Are 0.5 μm x 1.5 μm and the Thickness of the Film Is About 90 nm of Tin and 9 nm of Germanium.

[20, 52] is the screening parameter. Table III shows some experimental values obtained for the inductance and the screening parameter. The table clearly shows that because $\beta > 1$ the magnetic hysteresis effect will occur [27] in our Sn-Ge micro-SQUIDs.

Normalization of the experimental results in Fig. 38 are shown in Fig. 39 and Fig. 40. This shows that the flux enclosed by the loop is less than one half of a flux quantum. This micro-SQUID was also taken out of the PPMS, left in the open air and then measured 10 days later (Fig. 41). The results were consistent with the measurements performed initially. To normalize the critical current values on the y-axis, the maximum critical current recorded throughout the oscillations was recorded

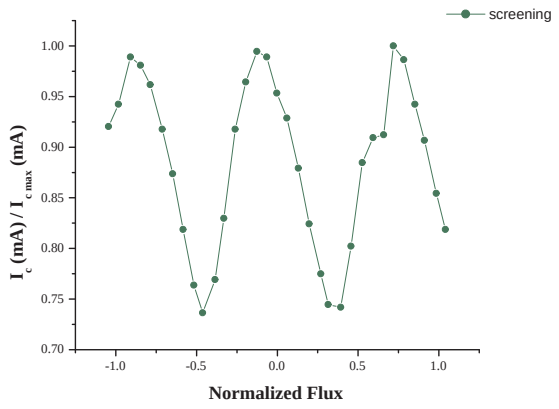

Fig. 40. Normalized Critical Current Modulation Due to Applied Flux Accounting for the Maximum Screening Effects in the Modulated Signal. The Junctions Used for This Device Were Dayem Bridges with Lengths Approximately Equal to 2 ξ_0 and Widths Equal to ξ_0. Dimensions of the Inner Loop of the Micro-SQUID are 0.5 μm x 1.5 μm and the Thickness of the Film Is about 90 nm of Tin and 9 nm of Germanium.

and divided by each critical current value. The flux generated by the externally applied magnetic field Φ_X was also normalized with respect to the flux quantum Φ_0. The Normalized Flux (Norm. Flux) contribution by each micro-SQUID will be represented as

$$\textbf{Norm. Flux} = \frac{\Phi_X}{\Phi_0} \tag{6.8}$$

in this Dissertation.

Each device in our analysis, see Table II, recorded a value lower than its theoretical value. For a more extensive listing of experimental data recorded for the various dimensions, see Appendix A.

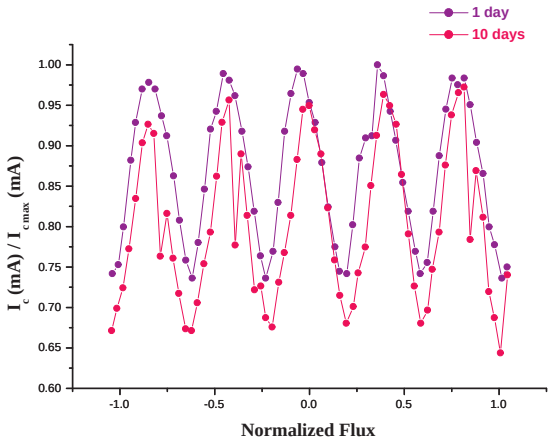

Fig. 41. Tin-Germanium Micro-SQUID Was Still Operational after 10 days in Air. The Junctions Used for This Device Were Dayem Bridges with Lengths Approximately Equal to 2 ξ_0 and Widths Equal to ξ_0. Dimensions of the Inner Loop of the Micro-SQUID Are 0.5 μm x 1.5 μm and the Thickness of the Film Is about 90 nm of Tin and 9 nm of Germanium.

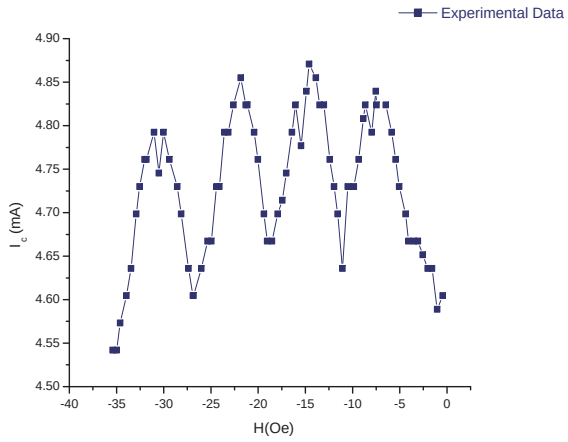

Fig. 42. Experimental Data for Critical Current Modulation for 2X Micro-SQUID Taken at 2.0 K. The Period of Oscillation Was Approximately Twice the Period of Modulation for the 1X Micro-SQUID. The Junctions Used for This Device Were Dayem Bridges with Lengths Approximately Equal to 2 ξ_0 and Widths Equal to ξ_0. Dimensions of the Inner Loop of the Micro-SQUID Are 1.0 μ m x 1.5 μ m and the Thickness of the Film Is about 90 nm of Tin and 9 nm of Germanium.

C. Period

In section B we discussed the results in the Fig. 38 which showed that the expected period of oscillation of the flux enclosed by the loop was lower than the expected value. One example was found by examining a micro-SQUID device (Fig. 42) twice the size of the micro-SQUID in Fig. 38, which was called 1X.

The period of oscillation for the 1X micro-SQUID was found to be about 12 Oe - 13.5 Oe and the 2X (twice the area of 1X) micro-SQUID showed the period to be about 6.0 Oe - 7.5 Oe. Investigation into the periodic intervals of the magnetic field values of the 1X micro-SQUIDs found that they were $50\% - 60\%$ less than their expected value (29.6 Oe) and those of the 2X micro-SQUID were $46\% - 53\%$ less

than expected (14.8 Oe), which gives corroborating evidence that some additional contribution was responsible for the flux quantum value.

The actual areas of the 1X, and 2X micro-SQUIDs were found to be approximately 0.675 μm^2,and 1.325 μm^2 respectively) when viewed with a scanning electron microscope. To ensure that the modulated response was due solely to the behavior of the micro-SQUIDs and not an artifact of the measuring system, three devices were fabricated for each dimension and tested for similar results. The critical current values were observed at 1-5 Oe increments on the I-V curve so that their oscillating behavior could be traced from 0 Oe to 50 Oe. This test was incorporated in the data collecting procedure as a way to provide a quick analysis of the micro-SQUID's response to an applied field.

Once the range of a few oscillating intervals was established, the midway point and the lowest end (called the knee) of the critical current slope was observed and approximately 5 preliminary points where chosen from that interval as possible options for the sampling voltage. The best sampling points were found to be closest to the knee because these sampling voltages were able to capture the total critical response for each device. There was at least 3 common sampled voltage reference points used to record the critical current value for each dimension of the micro-SQUID devices analyzed. As a result of these systematic checks, such as measuring 3 different devices, comparing their periodicity at different temperatures and taking data at several different sampling voltages there was conclusive evidence that the periodicity of the 2X version was on average close to half the periodicity of the 1X micro-SQUID (Fig. 43) which is consistent with theory.

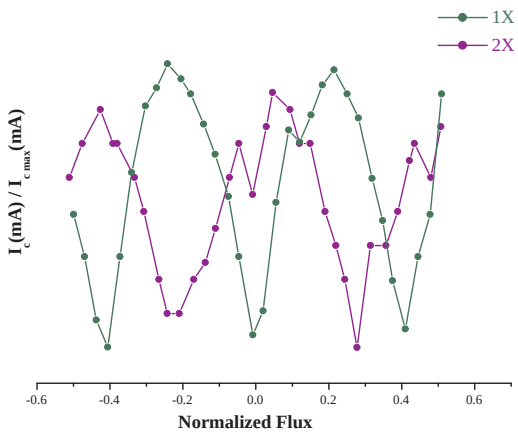

Fig. 43. Period of 1X Micro-SQUID Is Close to Twice the Period of the 2X Micro-SQUID.

D. Miniaturization

The majority of the Sn-Ge micro-SQUID miniaturization analysis was concentrated at dimensions equal to or below 1.5 μm x 1.5 μm. Several micro-SQUIDs were fabricated with Dayem bridge widths below the coherence length of tin (such as 70 nm, 100 nm, 140 nm, 180 nm, 200 nm). However, each device was not able to sustain a 1 μA bias current for very long and was inoperable after a few seconds or broke down immediately. In contrast, Dayem bridge widths above the coherence length of tin (such as, 250 nm, 280 nm, 320 nm) had a greater probability of exhibiting reduced and unstable modulation depths because they had a greater propensity for carrying large critical currents due to the increased mean free path of the junction.

The minimum electrode arm width for the micro-SQUID device to work was found to be approximately 400nm. This significantly limited how small we could make our Sn-Ge micro-SQUID device, since it was established, in section B that our

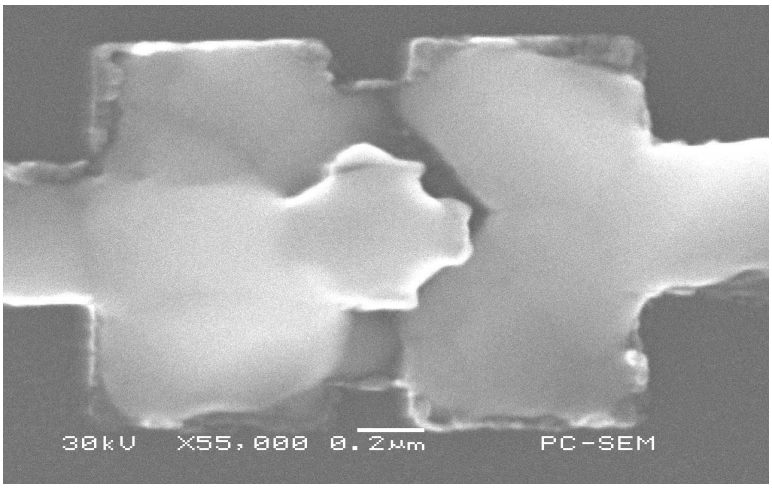

Fig. 44. Minimization of Micro-SQUID Area to 500 nm x 500 nm. The Inner Loop Area Was Connected by a Thin Film of Tin That Could Not Be Sonicated Loose. The Devices Fabricated at Lower Dimensions also Had the Same Result.

devices would automatically screen out the area enclosed up to the midpoint of the electrode arms giving

$$A_{enc} = (X + \frac{400}{2})(Y + \frac{400}{2}) \tag{6.9}$$

where A_{enc} is the actual area enclosed by the loop and $A_{loop} = XY$ is the approximate hole area fabricated using electron beam lithography.

Fabrication of the group IV micro-SQUIDs was done as a series of arrays with each dimension reproduced in rows of five similar devices. The results were observed using a scanning electron microscope (SEM) where it was observed that the hole area A_{loop} could not be well defined using the lift off processing technique, after several attempts were made. Fig. 44 shows an attempt to fabricate an Sn-Ge micro-SQUID with dimension 500 nm x 500 nm. The inner loop area was connected by a thin film

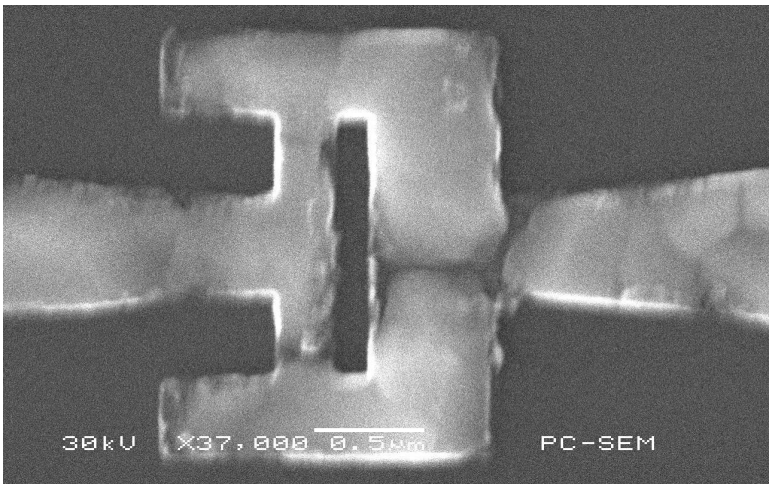

Fig. 45. Minimization of Micro-SQUID Area to 200 nm x 1.4 μm. Able to Carry a Bias Current but Did Not Show a Critical Current Response to a Changing Magnetic Field.

of tin that could not be sonicated loose. The devices fabricated at lower dimensions also had the same result.

The next approach in the device minimization process involved lowering one dimension at a time, that is, either dimension X or dimension Y for analysis. This approach allowed the micro-SQUID to enter the sub-micrometer regime with effective loop areas as low as 140 nm^2. Fig. 45 and Fig. 46 were the lowest areas fabricated which were able to carry a bias current through them. Both devices, however, did not show a critical current response to a changing applied magnetic field. The lowest Sn-Ge micro-SQUID dimensions to achieve an operational reaction was found to be 250 nm x 1.4 μm (see Fig. 47). Furthermore, the modulated signal response had already saturated (broken down) a few hundreds of a nanometer above this point at the 400 nm mark (see Fig. 48).

Observations of the modulated signal close to 400nm x 1.4 μm showed that the

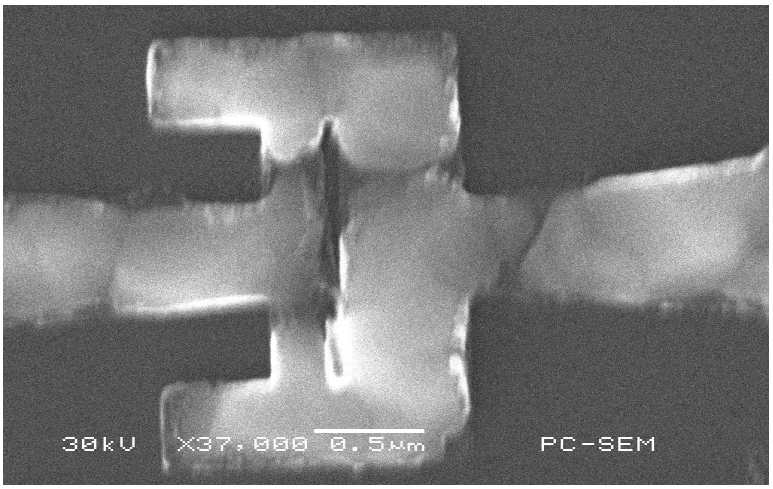

Fig. 46. Minimization of Micro-SQUID Area to 100 nm x 1.4 μm. Able to Carry a Bias Current but Did Not Show a Critical Current Response to a Changing Magnetic Field.

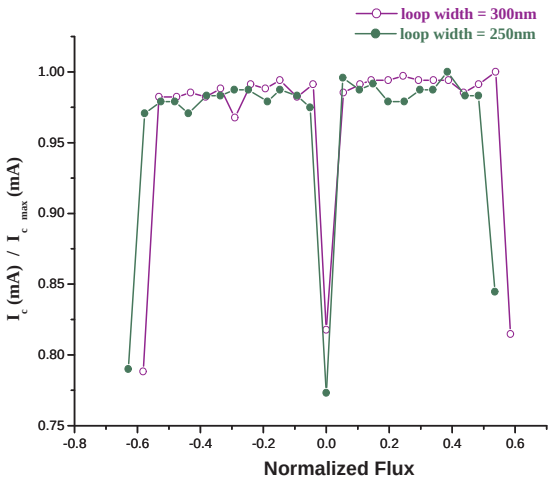

Fig. 47. Normalized Modulation Response of Two Group III Micro-SQUIDs with Widths 250nm and 300nm. Length of Both Micro-SQUIDs is 1.4 μm

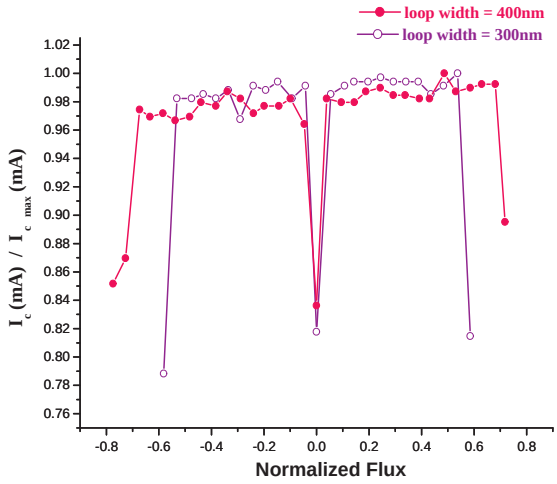

Fig. 48. Normalized Modulation Response of Group III Micro-SQUIDs with Widths 300nm and 400nm. There is a Diminution of Period at Widths Lower than 400nm.

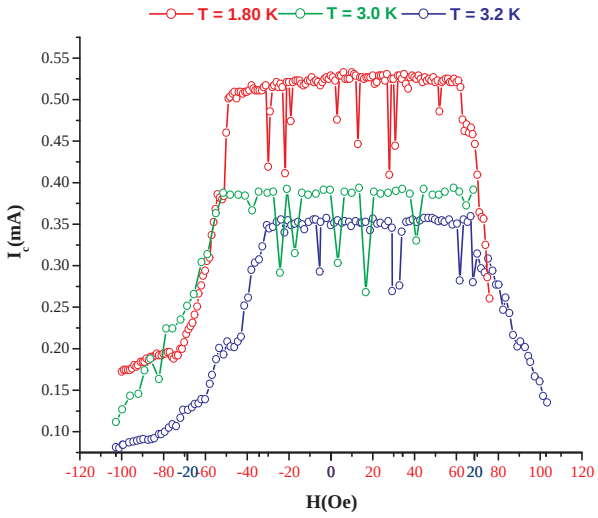

Fig. 49. Saturation of Miniaturized Micro-SQUID Response. Micro-SQUID in Vortex State.

amplitude began to flatten out, that is, become saturated (see Fig 49). Fig. 47 shows micro-SQUIDs with reduced X dimensions 300 nm and 400 nm and that there is a diminished flux response for the 300 nm width micro-SQUID. As the dimension is reduced further, we see that the flux response is also slightly reduced. Further investigations of these micro-SQUIDs showed that the devices in this region (from 250 nm to 400 nm) had similar flux responses with values ranging from 10 Oe to 14 Oe with similar amplitudes and modulation depths to Fig. 47 and Fig. 48. The poor performances of the micro-SQUIDs in this region can be attributed to two factors, the break down in the optimal performance caused by carrying large critical currents which give rise to massive heating of the junctions that create hysteretic behavior and the other being the noise caused by the flux motion due to the thermal activation of loosely pinned vortices that can randomly jump from one site to the other causing a distortion in the signal, the micro-SQUID design or the superconducting film quality [55, 56].

The high critical currents are tied into our fabrication process and will vary from sample to sample. One way to improve the response of these devices is to leave them in air from a week to a month increasing their electrical resistance through oxidation and thus lowering their critical current using time as a variable parameter. Although the device is cooled in zero field to eliminate the vortex pinning sites, there is a tiny residual field (off set value) that is always present due to the magnet's attachment on our low temperature setup which may cause these sites to appear, however this field contribution is extremely small compared to the weakly pinned vortex sites created by the structural defects (holes) in the superconducting film once a magnetic field is applied (magnetic hysteresis). The Sn-Ge surfaces were extremely rough and had irregular defects throughout the film as are evident in Fig. 45, which have been shown to give rise to large pinning forces and high critical current densities

in superconductors [56].

E. Degrading Effects in Micro-SQUID Design

The design of the micro-SQUID for a given operating temperature T follows a relatively standard procedure. The micro-SQUID inductance and junction capacitance are made as small as possible with the fabrication technology available. The minimum junction capacitance that can be achieved by most SQUID fabrication technologies is about 0.5 pF to 1 pF [57]. Once the inductance is chosen, the loop area is designed and the critical current is found experimentally from the critical current - applied field modulation graph or the hysteretic I-V graph. From here the screening parameter can be found. This screening parameter along with the junction capacitance can then determine the shunt resistance and hence the Stewart-McCumber parameter. It has also been found that the $\frac{1}{f}$ noise of SQUIDs scales as $\frac{I_c}{\sqrt{A_J}}$, where A_J is the area of a junction for a SQUID device by Savo and others [57, 58].

The effective area, which was also known as the effective flux capture area of the SQUID was used to determine the magnetic field resolution $B_n(f)$ and we can see that the magnetic field response generated using this effective area would be lower than using the inner loop area of the micro-SQUID device (Table IV and Table V). If we adjusted our experimental modulation calculations to reflect optimized values for the effective area, this would bring our calculations for the period of oscillations to within 10% to 20% of the expected value, when previously the calculations would be between 22% to 33%.

Our Micro-SQUID design does not take into account the flux penetration into thin film structures. London theory predicts a magnetic field would penetrate a superconducting film exponentially to its penetration depth, and would expel weak

Table IV. Actual Area and Experimental Area of Micro-SQUID Loop.

Group	Dimensions (μm x μm)	Actual Area (μm^2)	A_E (Theoretical) (μm^2)
I	1.5 x 1.5	2.25	4.81
I	1.5 x 1.0	1.5	3.22
II	1.4 x 1.0	1.4	3.01
II	1.4 x 0.5	0.7	1.96
II	1.4 x 0.4	0.56	1.84
III	1.0 x 0.5	0.5	1.64
III	1.4 x 0.3	0.42	1.40
III	1.4 x 0.25	0.35	1.18

Table V. Experimental Values for the Period Associated with the Applied Magnetic Field of Different Loop Sizes.

Group	Dimensions (μm x μm)	Actual Area (μm^2)	Φ_X (Theoretical) (μm^2)	Φ_X (Exp.) (μm^2)
I	1.5 x 1.5	2.25	4.30	4.0
I	1.5 x 1.0	1.5	6.42	5.5
II	1.4 x 1.0	1.4	6.87	7.0
II	1.4 x 0.5	0.7	10.55	13.0
II	1.4 x 0.4	0.56	11.21	13.5
III	1.0 x 0.5	0.5	12.59	14.0
III	1.4 x 0.3	0.42	14.76	14.0
III	1.4 x 0.25	0.35	17.53	14.0

magnetic fields (from the interior) at its edges by the Meissner Effect [40]. Thus, the flux sensing area derived from conventional approximations would give unreliable estimates. The experimental uncertainty associated with the magnetic field measurements may be attributed to the field error in the magnet used [59] due to pinned remanent flux escaping from the magnet windings and the effective flux sensing area being enlarged by an uncertainty factor that is dependent on the penetration depth and thickness of the film, see Table IV. Thus, the resulting experimental output for the period would be smaller than theoretical estimates. Hao and others [59], have shown that the penetration depth inconsistencies could create an error in measuring the flux by as much as 10% and random experimental uncertainties in magnetic field by as much as 3%.

By using the effective flux capture area of the SQUID loop used by Hao to optimize the micro-SQUIDs, the period of oscillations would be within 5% to 15% on average of the expected value, see Table V. A correction of 5% to 15% in the period would be consistent with the results seen in other micro-SQUID experiments [57, 52, 19, 20, 26]. The diminished critical current modulation depths was also consistent with the results seen in the other experiments with large critical current values. The degradation of the output of the device was confirmed by the large values obtained for the screening parameters for each loop area investigated which shows that the micro-SQUID is not operating under optimized conditions.

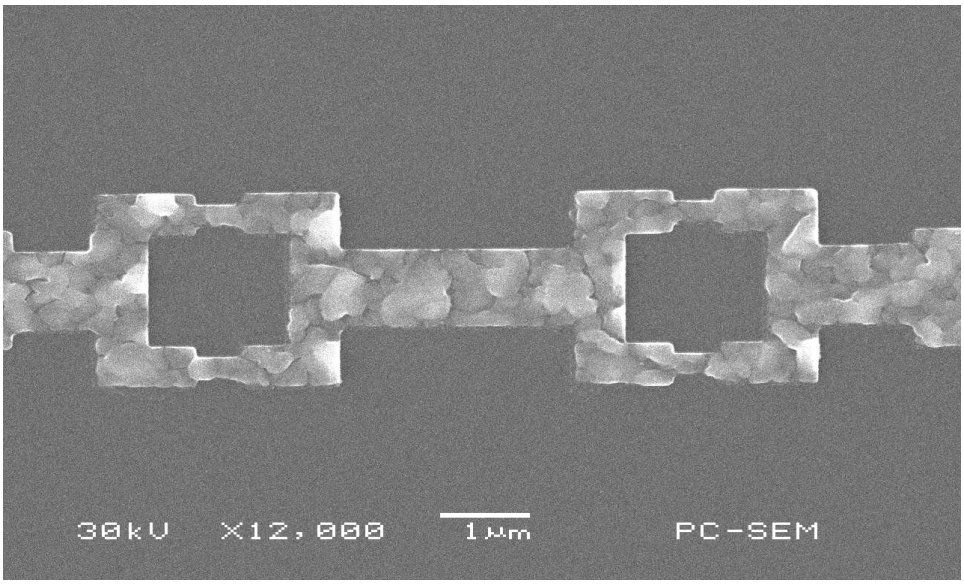

Fig. 50. Two micro-SQUIDs Connected in Series. The Junctions Used for This Device Were Dayem Bridges with Lengths Approximately Equal to 2 ξ_0 and Widths Equal to ξ_0. Dimensions of the Inner Loop of the Micro-SQUID Are 1.5 μ m x 1.5 μ m and the Thickness of the Film Is about 90 nm of Tin and 9 nm of Germanium.

F. Elements in Series

One method investigated to reduce the flux noise response of the Sn-Ge micro-SQUIDs was to increase their modulation depths by connecting them in series (Fig. 50). A simple series circuit, consisting of two micro-SQUIDs of the same dimensions, was fabricated to test for signal improvement. At temperatures close to the critical temperature (see Fig 51), the modulation period of the series system was found to be coherent with that of a single micro-SQUID of the same dimension. However, the amplitude of the critical current became larger in some intervals but remained the same as the single micro-SQUID in other intervals. A reason for this behavior may be attributed to the coupling of the inductances and the interactions of

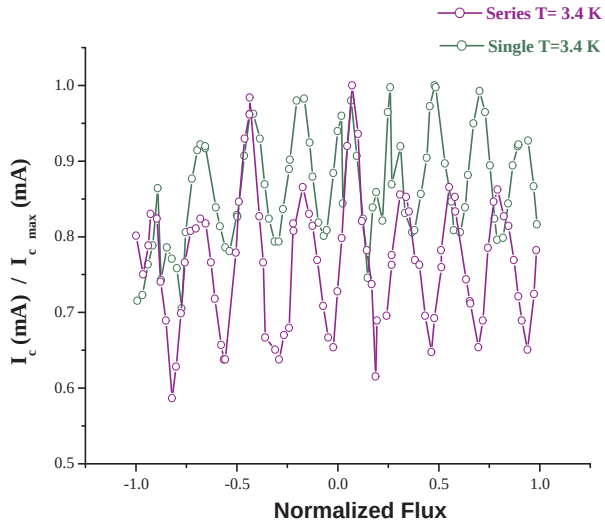

Fig. 51. Normalized Modulation Response of Two micro-SQUIDs in Series Compared to Single Micro-SQUID Response at T = 3.4 K. The Modulated Response of the Series System Was Found to be Coherent With that of a Single Micro-SQUID of the Same Dimension.

the induced circulating currents of the two micro-SQUIDs [31, 60, 32]. The difference in the coupling inductances caused a irregular modulated signal (non-identical signals added together to create one output) to occur in the micro-SQUID system.

As the temperature moves further away from the superconducting critical temperature of the device, the period of modulation for the series system decreased while that of a single micro-SQUID with the same loop dimensions stayed the same (see Fig 52). The amplitude of modulation was also greatly diminished. For example, the critical current value for the series micro-SQUID system was approximately 3.07 mA for a temperature of 3.4 K in comparison to being 0.63 mA at 2.0 K. A survey of the temperatures showed that the signal began to diminish within the temperature range of 2.7 K to 3.2 K. As we have discussed in previous sections, high critical currents

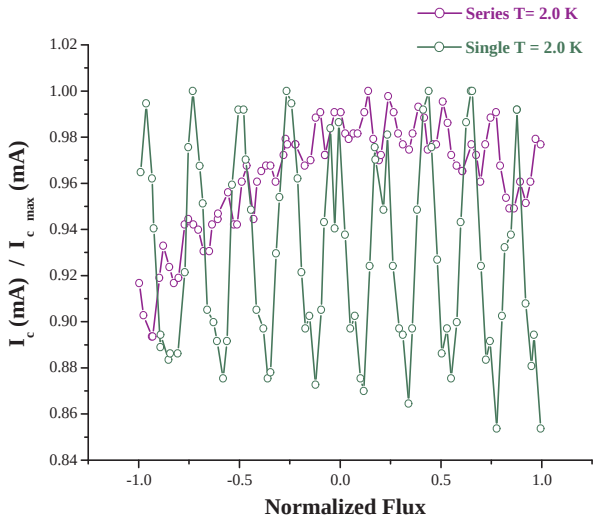

Fig. 52. Normalized Modulation Response of Two Micro-SQUIDs in Series Compared to a Single Micro-SQUID Response at T = 2.0 K. The Induced Currents for the Micro-SQUIDs in Series Were Coupled to Cancel More of the Modulated Signal.

would increase the thermal heating at the junctions and throughout the device, which can cause unstable regions in the modulated signal to occur.

The diminished modulated response provides clear evidence that the critical currents of the two micro-SQUIDs in series are not equal to each other and that their induced currents will be increased at temperatures further away from the critical temperature of the superconducting device, where high critical currents may exist. In addition, Fig 52 shows that the induced currents were coupled to cancel more of the modulated signal, meaning the modulated response for the individual micro-SQUIDs became more incoherent (out of phase with each other) as the temperature decreased.

CHAPTER VII

SUMMARY AND CONCLUSION

For this dissertation, microscopic square and rectangular superconducting quantum interference devices (SQUIDs) made of tin were successfully fabricated and characterized using the electron beam lithography technique and a resistive heating thermal evaporation process. The thickness of the SQUIDs were reduced, by using a pre-nucleation layer of germanium as a mechanism for electrical transport, by a factor of 2. The surface of these tin germanium SQUIDs were found to be rough and uneven with defects such as cracks and holes existing throughout the film, see Fig. 53. These SQUIDs were also found to have critical temperatures (3.65 K) that were slightly lower than the bulk value 3.72 K and further investigations found that the SQUIDs had hysteretic I-V curves, similar to those described by Hasselbach and Wernsdorfer [18, 1] and had a modulated response in critical current to an applied magnetic field. These characteristics were still present in the SQUIDs after weeks of the devices standing in air. The modulated response however was smaller than those observed by Hasselbach and Wernsdorfer due to uncertainties in the effective area attributed to the magnetic field penetration within the device.

Another objective of our experiments was to find the smallest functional geometry that our SQUIDs could still be operational. This was found to be at a dimension of 500 nm x 1.4 μm. The junction length for this device was approximately 500 nm $\approx 2\xi_0$ and 230 nm $\approx \xi_0$ in width. Attempts to reduce these lengths further, such as to 500 nm x 1.0 μm, showed a much more noisy response. In addition, the devices fabricated at this dimension exhibited extremely high critical currents, which implied that the modulated signal could still be buried in the device response. Other SQUIDs fabricated below this functional size also showed very poor performance resulting from

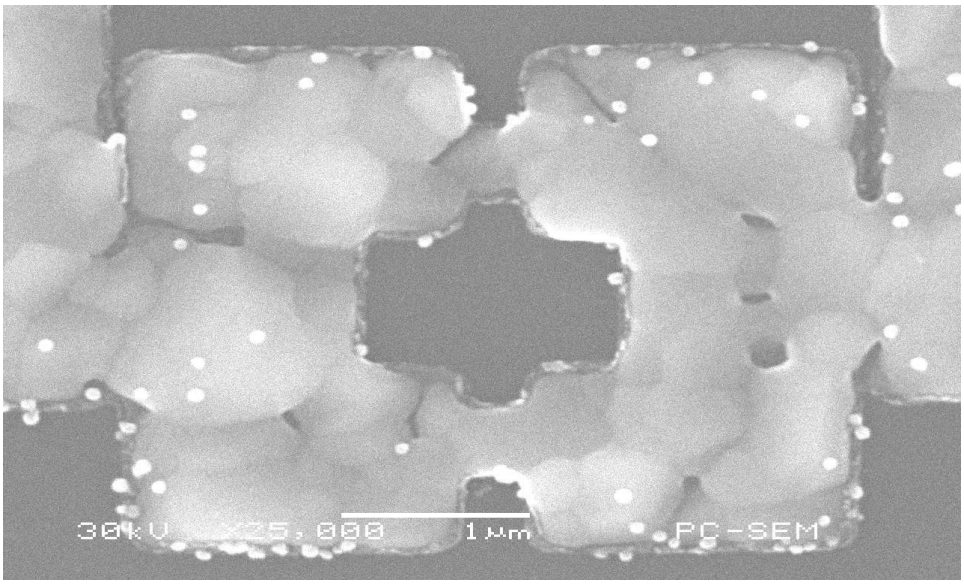

Fig. 53. Film Surface of SQUID Is Rough and Contains Holes and Cracks

noise and hysteresis effects. There was no change in the device response because it was overwhelmed by extremely large critical currents and noise creating a saturated output, see Chapter VI, Fig. 49

If we recall from Chapter III, Section B that the flux-voltage transfer function V_Φ can be approximated by

$$V_\Phi \cong \frac{\Delta V}{\frac{\Phi_0}{2}} \cong \frac{R}{2L} \tag{7.1}$$

and that the voltage modulation depth ΔV can be written as

$$\Delta V \approx \frac{I_c R}{2} \tag{7.2}$$

and we see that the voltage transfer function can be represented in terms of the critical current by

$$V_\Phi \approxeq (\frac{R}{\Phi_0})I_c = kI_c \tag{7.3}$$

where $k = \frac{R}{\Phi_0}$ is a constant. As a result, other than an amplitude change the critical current modulation can be used to predict the behavior of the voltage transfer function in the SQUIDs. With this concept in mind, comparison of our results in chapter VI Fig. 49 with the results obtained by Berdiyorov [29] shows that our results closely corresponds to the weakly pinned interstitial vortices that were prone to move about in the superconductor, confirming that we have reached a limiting geometry due to our SQUID design. Further attempts at minimization should include a SQUID re-design that would minimize the screening currents within the electrode arms, such as the inclusion of a flux pick up loop or introducing a control current to the device.

Preliminary experiments that were performed to assess the enhancement of the SQUID signal with serial connections of micro-devices showed promise at temperatures close to T_c. The oscillating signal of the two directly coupled SQUIDs would superimpose if the critical currents were equal. The current method employed to find equal critical currents is the trial and error approach. Continuously making samples to achieve our enhancement goals would not be an ideal strategy when trying to fabricate reproducible devices, especially with the added complications of very high critical current and surface roughness. Therefore, better methods are needed to control the coherence of the individual SQUID modulations if they are to be utilized as localized detectors.

REFERENCES

[1] K. Hasselbach, D. Mailly, and J. Kirtley, J. Appl. Phys. **91**, 4432 (2002).

[2] R. C. Jaklevic, J. Lambe, A. H. Silver, and J. Mercereau, Phys. Rev. Lett. **12**, 159 (1964).

[3] A. H. Silver and J. E. Zimmerman, Phys. Rev. **157**, 317 (1967).

[4] J. Zimmerman and A. H. Silver, Phys. Rev. **141**, 367 (1966).

[5] J. Zimmerman, P. Theine, and J. Harding, J. Appl. Phys. **41**, 1572 (1970).

[6] J. E. Mercereau, Rev. Phys. Appl. **5**, 13 (1970).

[7] M. Nisenoff, Rev. Phys. Appl. **5**, 21 (1970).

[8] F. London, *Superfluids*, Wiley, New York, 1st edition, 1950.

[9] B. Josephson, Phys. Lett. **1**, 251 (1962).

[10] J. Bardeen, L. N. Cooper, and J. Schrieffer, Phys. Rev. **108**, 1175 (1957).

[11] P. Anderson and J. M. Rowell, Phys. Rev. Lett. **10**, 230 (1963).

[12] B. S. Deaver and W. M. Fairbank, Phys. Rev. Lett. **7**, 43 (1961).

[13] R. Doll and M. Nabauer, Phys. Rev. Lett. **7**, 51 (1961).

[14] J. Clarke, W. M. Goubau, and M. B. Ketchen, J. Low Temp. Phys. **25**, 99 (1976).

[15] C. Tesche and J. Clarke, J. Appl. Phys. **79**, 8783 (1996).

[16] J. Jaycox and M. Ketchen, IEEE. Trans. Magn. **17**, 400 (1981).

[17] H. Koch and H. Lubbig, editors, *Superconducting Devices and Their Applications: Proceedings of the 4th International Conference SQUID '91*, Berlin, Germany, 1992, SQUID '91, Springer-Verlag.

[18] W. Wernsdorfer, D. Mailly, and A. Benoit, J. Appl. Phys. **87**, 5094 (2000).

[19] G. Podd, G. Hutchinson, D. Williams, and D. Hasko, Phys. Rev. B **75**, 1 (2007).

[20] S. Lam and D. Tilbrook, Appl. Phys. Lett. **82**, 1078 (2003).

[21] K. Hasselbach, C. Veauvy, and D. Mailly, Physica C **332**, 140 (2000).

[22] J. Gorman, Science News **164**, 171 (2003).

[23] M. Janawadkar et al., Current Science (India) **77**, 759 (1999).

[24] W. Wernsdorfer, Supercond. Sci. Technol. **22**, 1 (2009).

[25] L. Fong et al., Rev. Sci. Instrum. **76**, 1 (2005).

[26] S. Lam, International Conference of Nanoscience and Nanotechnology 2006. ICONN 06 , 377 (2006).

[27] M. Tinkham, *Introduction to Superconductivity*, Dover Publications, Inc., Mineola, New York, 2nd edition, 1996.

[28] J. Gallop, *SQUIDs, the Josephson Effects and Superconducting Electronics*, Adam Hilger, National Physical LAboratory, 1st edition, 1990.

[29] G. R. Berdiyorov, M. V. Milosevic, and F. M. Peeters, Physica C. **437**, 25 (2006).

[30] C. Jooss, A. Forkl, and H. Kronmuller, Physica C. **268**, 87 (1996).

[31] V. Schultze, V. Zakosarenko, R. IJsselsteijn, J. Ramos, and H.-G. Meyer, IEEE. Trans. Appl. Supercond. **9**, 3279 (1999).

[32] C. H. Wu et al., Supercond. Sci. Technol. **19**, 246 (2006).

[33] H. K. Onnes, *Superconductivity*, Leiden Comm, Leiden, 1st edition, 1911.

[34] G. White and P. Meeson, *Experimental Techniques in Low-Temperature Physics*, Oxford University Press, Oxford, England, 4th edition, 2002.

[35] W. Meissner and R. Ochsenfeld, Naurwissenschaften **21**, 787 (1933).

[36] C. Kittel, *Introduction to Solid State Physics*, chapter 12, pages 333 – 377, John Wiley and Sons Inc., Hoboken, New Jersey, 1996.

[37] P. Tipler and R. Llewellyn, *Modern Physics*, chapter 10, pages 483 – 495, W.H. Freeman and Company, New York, New York, 1999.

[38] R. Serway, C. Moses, and C. Moyer, *Modern Physics*, chapter 12, pages 476 – 527, Saunders College Publishing, Orlando, Florida, 1997.

[39] C. Veauvy, K. Hasselbach, and D. Mailly, Phys. Rev. B **70**, 214513 (2004).

[40] A. Rose-Innes and E. H. Rhoderick, *Introduction to Superconductivity*, volume 6, Pergamon Press Ltd., Oxford, England, 2nd edition, 1978.

[41] L. Hao et al., IEEE Transactions of Applied Superconductivity **17**, 742 (2007).

[42] J. Sun, W. Gallagher, and R. Koch, Phys. Rev. B **50**, 13664 (1994).

[43] M. Keene, N. Exon, R. Humphreys, and N. Chew, J. Appl. Phys. **79**, 8783 (1996).

[44] R. H. Koch, D. P. DiVincenzo, and J. Clarke, Phys. Rev. Lett. **98**, 1 (2007).

[45] J. I. Goldstein et al., *Scanning Electron Microscopy and X-Ray Microanalysis*, Plenum, New York, 2nd edition, 1992.

[46] R. Pettit and J. Silcox, Phys. Rev. B **13**, 2865 (1976).

[47] J. Hill, C. Stoddart, and P. Stuart, J. Phys. D: Appl. Phys. **3**, 1168 (1969).

[48] W. Ruhl and P. Hilsch, Zeitschrift Fur. Phys. B. **26**, 161 (1977).

[49] H. Levingstein, J. App. Phys. **20**, 301 (1949).

[50] R. Richardson and E. Smith, *Experimental Techniques in Condensed Matter Physics at Low Temperatures*, Addison Wesley Longman, Inc., Reading, Massachusetts, 1998.

[51] G. White and P. Meeson, *Matter and Methods at Low Temperatures*, Springer-Verlag Berlin Heidelberg, Bayreuth, Germany, 4th edition, 1996.

[52] G. Hutchinson, H. Qin, D. Kang, D. Hasko, and D. Williams, Supercond. Sci. Technol. **16**, 1544 (2003).

[53] M. B. Ketchen, IEEE. Trans. Magn. **17**, 387 (1981).

[54] K. Likharev, Rev. Mod. Phys. **51**, 101 (1979).

[55] G. C. Tettamanzi, C. I. Pakes, S. K. H. Lam, and S. Prawer, Supercond. Sci. Technol. **22**, 1 (2009).

[56] S. Flament et al., Supercond. Sci. Technol. **17**, 180 (2004).

[57] J. Clarke and A. Braginski, *The SQUID Handbook, Vol I.*, Wiley VCH, Verlag, GmbH, 1st edition, 2004.

[58] B. Savo, F. C. Wellstood, and J. Clarke, Appl. Phys. Lett. **50**, 1757 (1987).

[59] L. Hao et al., J. App. Phys. **99**, 1 (2006).

[60] R. P. Welty, IEEE. Trans. Magn. **27**, 2924 (1991).

APPENDIX A

EXPERIMENTAL RESULTS FOR TIN GERMANIUM SQUIDS

This appendix supplements Chapter V and Chapter VI. It offers additional examples of device transition temperatures (i.e. its critical temperatures), current-voltage relationships, critical current - temperature relationships and its critical current - applied magnetic field relationships.

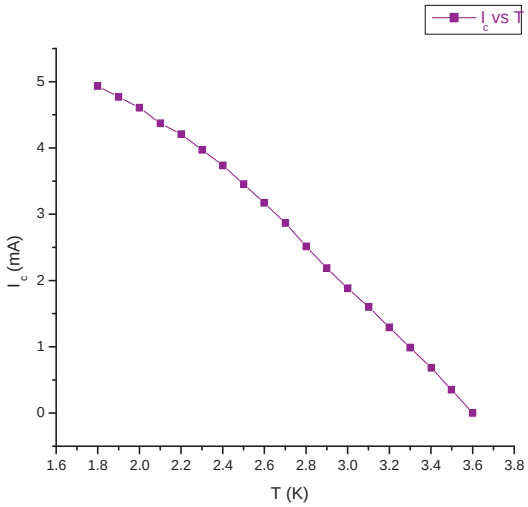

Fig. 54. Critical Current Characteristics for Temperature Change from 1.8 K to 3.6 K for a Group II Tin Germanium SQUID Called 2X. Dimensions of SQUID Were Approximately 1.0 μ m x 1.5 μ m and Used to Understand the Modulated Period. See Chapter VI for a Discussion of the Period of These SQUIDs and Chapter V for a Discussion on the Critical Current-Temperature Relationship.

I-V Curve Measurements Shown in Fig. 59 are Made when a DC Current Through the Sample was Ramped Up or Down in Small Discrete Steps (Usually 64, or 128 Steps

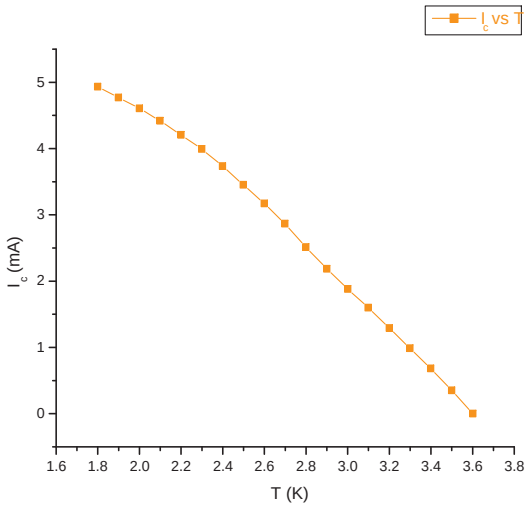

Fig. 55. Critical Current Characteristics for Temperature Change from 3.6 K to 1.8 K for a Group II Tin Germanium SQUID Called 2X. Dimensions of SQUID Were Approximately 1.0 μ m x 1.5 μ m and Used to Understand the Modulated Period. See Chapter VI for a Discussion of the Period of These SQUIDs and Chapter V for a Discussion on the Critcal Current-Temperature Relationship.

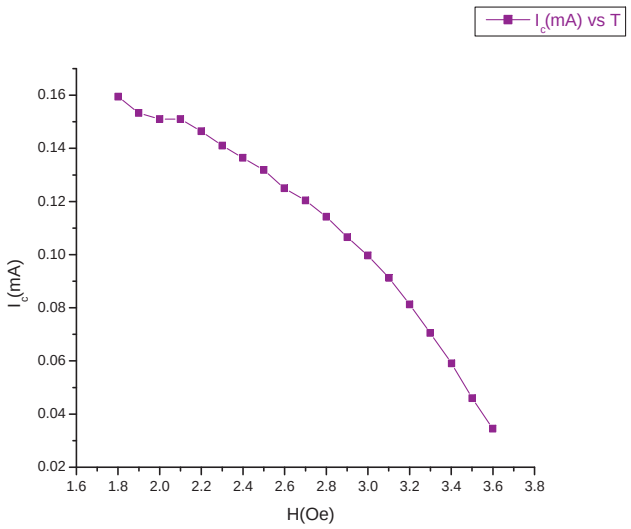

Fig. 56. Critical Current Characterisitics for Temperature Change from 3.6 K to 1.8 K for a Group II Tin Germanium SQUID Called 1X. Dimensions of SQUID Were Approximately 0.5 μ m x 1.5 μ m and Used to Understand the Modulated Period. See Chapter VI for a Discussion of the Period of These SQUIDs and Chapter V for a Discussion on the Critcal Current-Temperature Relationship.

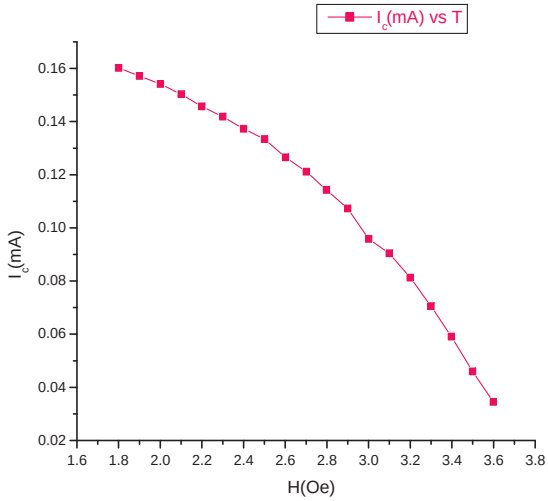

Fig. 57. Critical Current Characterisitics for Temperature Change from 1.8 K to 3.6 K for a Group II Tin Germanium SQUID Called 1X. Dimensions of SQUID Were Approximately 0.5 μ m x 1.5 μ m and Used to Understand the Modulated Period. See Chapter VI for a Discussion of the Period of These SQUIDs and Chapter V for a Discussion on the Critcal Current-Temperature Relationship.

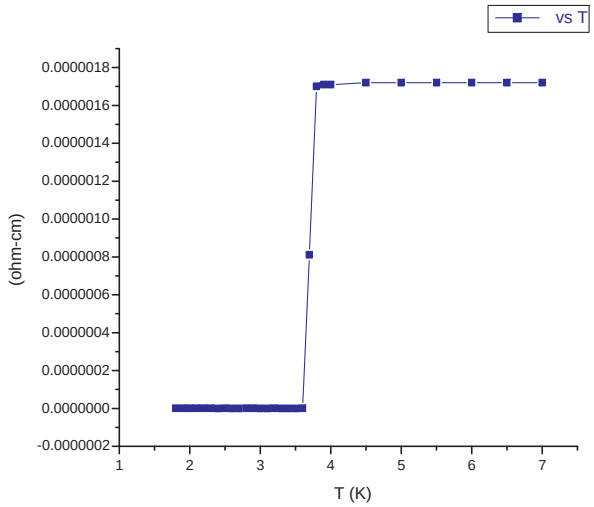

Fig. 58. Enlarged View of Resistivity Behavior Above Transition Temperature.

Per Quadrant). The Current Ramp was Started from a Specified Negative Maximum and Ramped Up to a Specified Positive Maximum ($-I_{max}$,I_{max}). As the Current Increases the Voltage Drop Across the Sample is Measured and Recorded.

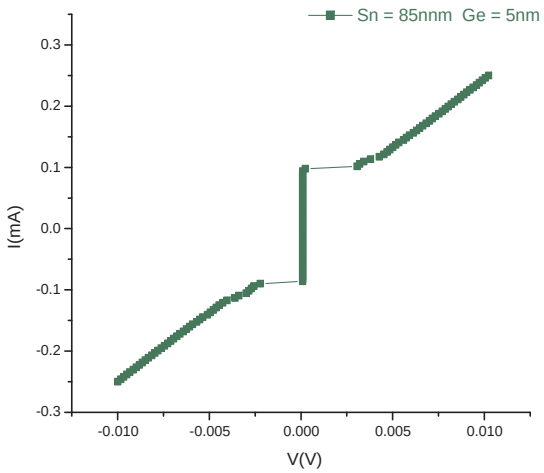

Fig. 59. Current Voltage Characteristics for Tin Germanium SQUIDs Sn = 85nm, Ge = 5nm.

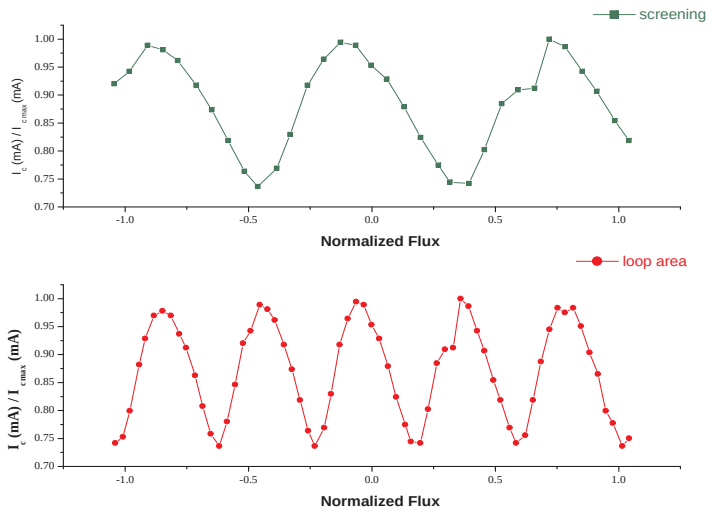

Fig. 60. Additional Fluxon Generated by Screening.

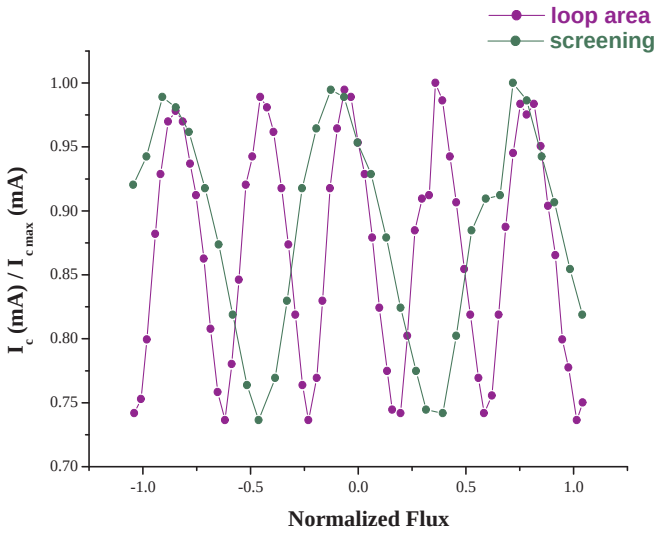

Fig. 61. Superposition of the Normalized Data, Screening Geometry in Line with Theory for Fluxon Generation.

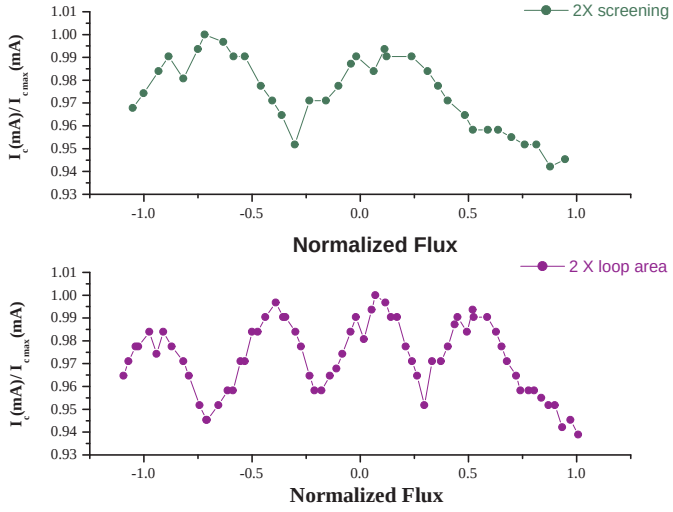

Fig. 62. Additional Fluxon Generated by Screening for SQUID 2X.

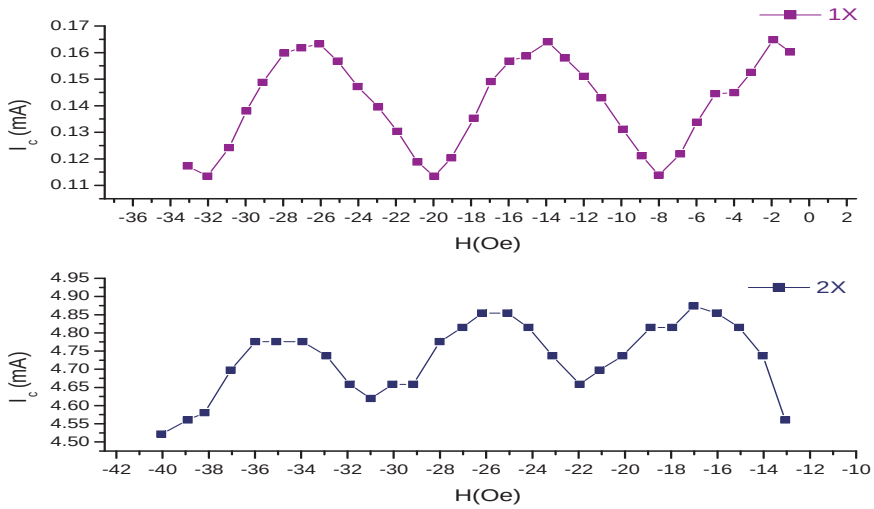

Fig. 63. Period of 2X SQUID Approximately 7.125 Oe.

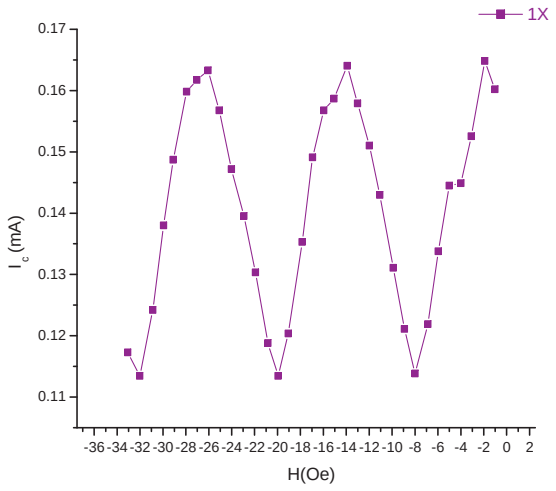

Fig. 64. Period of 1X SQUID Approximately 14 Oe.

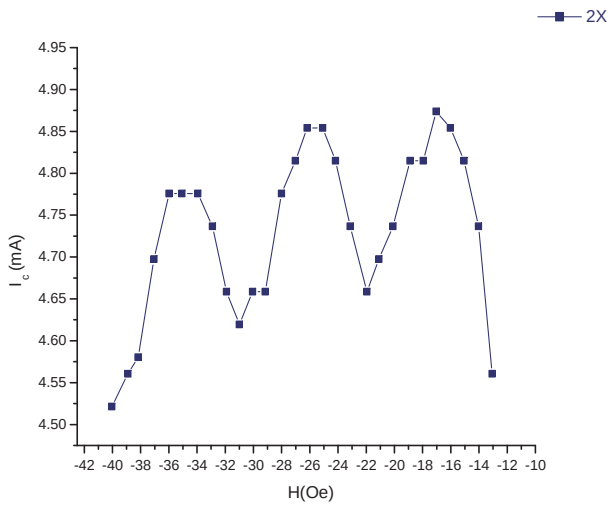

Fig. 65. Period of 1X SQUID is Approximately Twice the Period of the 2X SQUID.

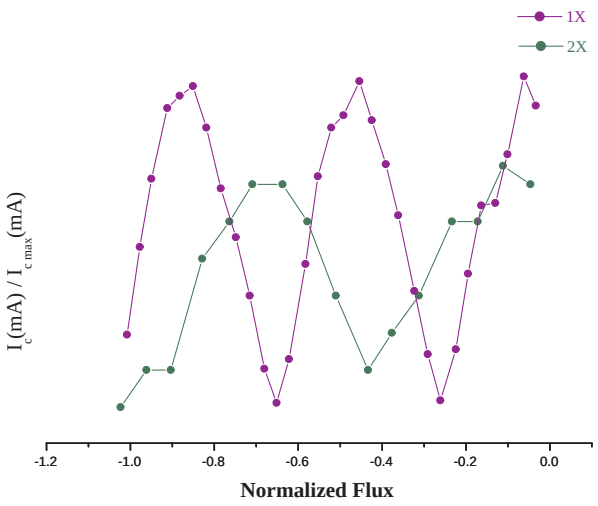

Fig. 66. Variations in Period for 1X Range from 50% to 86% Greater Than That of the 2X SQUID. This Closely Corresponds Because the Area of the 2X SQUID is Closer to 88% of What Its Value Should be.

APPENDIX B

MORE EXPERIMENTAL RESULTS FOR TIN GERMANIUM MICRO-SQUIDS

This appendix supplements Chapter VI and Chapter VII. It shows the individual graphs of the superimposed graphs displayed in Chapter VI.

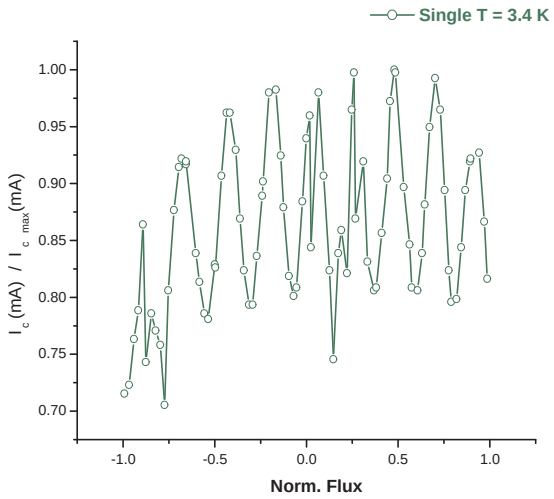

Fig. 67. Normalized Modulated Response of Micro-SQUID at 3.4 K. The Junctions Used for This Device Were Dayem Bridges with Lengths Approximately Equal to 2 ξ_0 and Widths Equal to ξ_0. Dimensions of the Inner Loop of the Micro-SQUID Are 1.5 μ m x 1.5 μ m and the Thickness of the Film Is about 90 nm of Tin and 9 nm of Germanium.

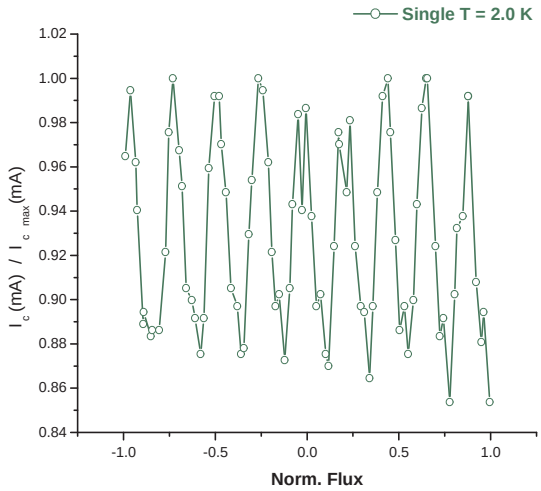

Fig. 68. Normalized Modulated Response of Micro-SQUID at 2.0 K. The Junctions Used for This Device Were Dayem Bridges with Lengths Approximately Equal to 2 ξ_0 and Widths Equal to ξ_0. Dimensions of the Inner Loop of the Micro-SQUID Are 1.5 μ m x 1.5 μ m and the Thickness of the Film Is about 90 nm of Tin and 9 nm of Germanium.

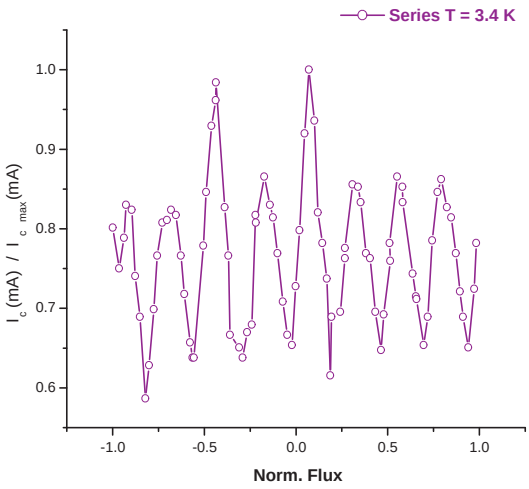

Fig. 69. Normalized Modulated Response of a Micro-SQUID in Series at 3.4 K. The Junctions Used for This Device Were Dayem Bridges with Lengths Approximately Equal to 2 ξ_0 and Widths Equal to ξ_0. Dimensions of the Inner Loop of the Micro-SQUID Are 1.5 μm x 1.5 μm and the Thickness of the Film Is about 90 nm of Tin and 9 nm of Germanium.

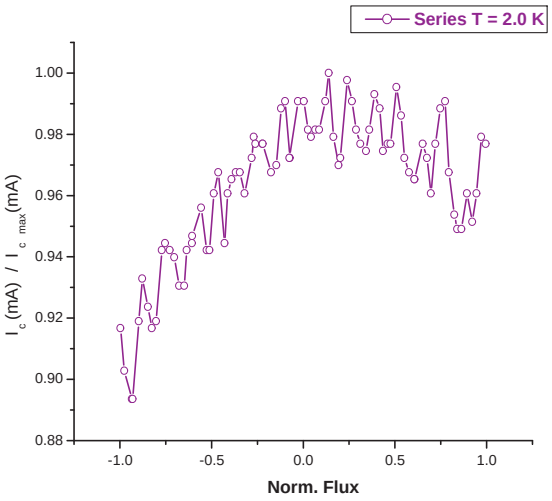

Fig. 70. Normalized Modulated Response of a Micro-SQUID in Series at 2.0 K. The Junctions Used for This Device Were Dayem Bridges with Lengths Approximately Equal to 2 ξ_0 and Widths Equal to ξ_0. Dimensions of the Inner Loop of the Micro-SQUID Are 1.5 μm x 1.5 μm and the Thickness of the Film Is About 90 nm of Tin and 9 nm of Germanium.

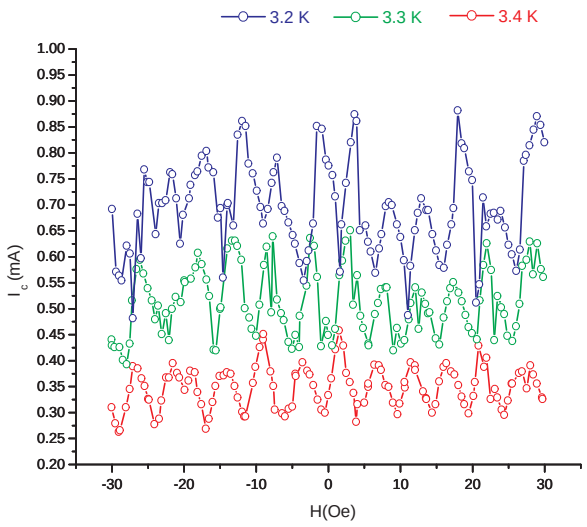

Fig. 71. Experimental Results of Modulated Response of Two Micro-SQUIDs in Series at 3.2 K, 3.3 K and 3.4 K. The Junctions Used for This Device Were Dayem Bridges with Lengths Approximately Equal to 2 ξ_0 and Widths Equal to ξ_0. Dimensions of the Inner Loop of the Micro-SQUID Are 1.5 μm x 1.5 μm and the Thickness of the Film Is about 90 nm of Tin and 9 nm of Germanium.

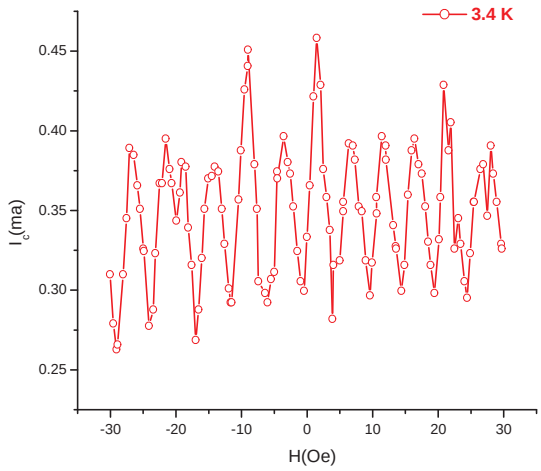

Fig. 72. Experimental Results of Modulated Response of Two Micro-SQUIDs in Series at 3.4 K. The Junctions Used for This Device Were Dayem Bridges with Lengths Approximately Equal to 2 ξ_0 and Widths Equal to ξ_0. Dimensions of the Inner Loop of the Micro-SQUID Are 1.5 μm x 1.5 μm and the Thickness of the Film is about 90 nm of Tin and 9 nm of Germanium.

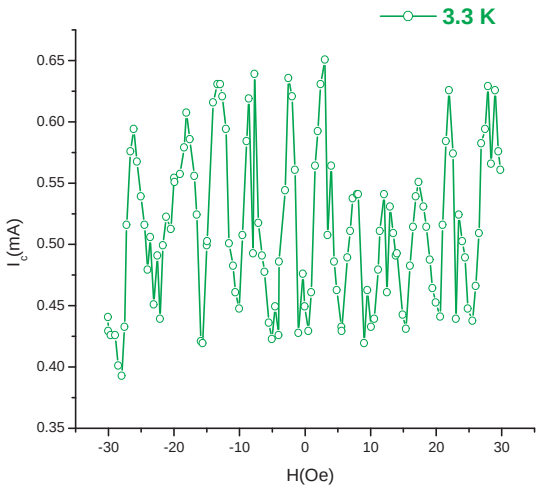

Fig. 73. Experimental Results of Modulated Response of Two Micro-SQUIDs in Series at 3.3 K. The Junctions Used for This Device Were Dayem Bridges with Lengths Approximately Equal to 2 ξ_0 and Widths Equal to ξ_0. Dimensions of the Inner Loop of the Micro-SQUID Are 1.5 μm x 1.5 μm and the Thickness of the Film Is about 90 nm of Tin and 9 nm of Germanium.

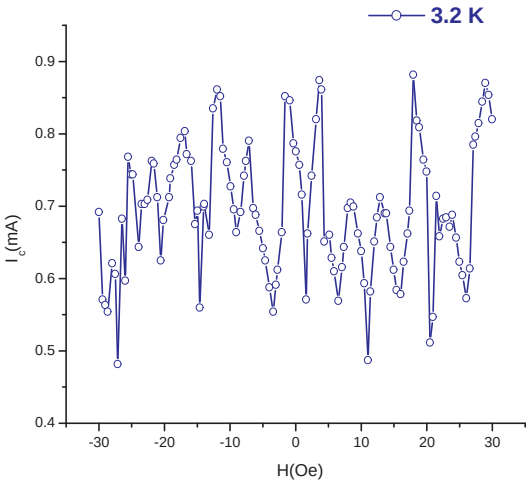

Fig. 74. Experimental Results of Modulated Response of Two Micro-SQUIDs in Series at 3.2 K. The Junctions Used for This Device Were Dayem Bridges with Lengths Approximately Equal to 2 ξ_0 and Widths Equal to ξ_0. Dimensions of the Inner Loop of the Micro-SQUID Are 1.5 μm x 1.5 μm and the Thickness of the Film is about 90 nm of Tin and 9 nm of Germanium.

APPENDIX C

SEM IMAGES FROM DEVICE FABRICATION

This appendix supplements Chapter IV and Chapter VI. It shows selected image results from the fabrication and testing stages of the superconducting quantum interference devices (Micro-SQUIDs) made from Aluminum, Tin, and Lead after lift-off processing. The Micro-SQUIDs were made using electron beam lithography and thermal evaporation.

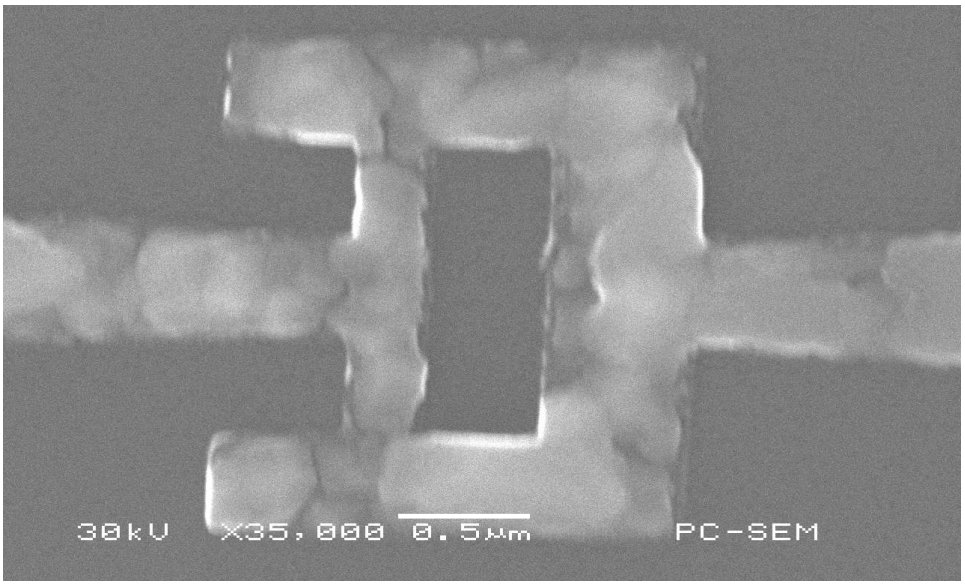

Fig. 75. Micro-SQUID Area called 1X (See Chapter VI, Section C for More Details), Showing a Continuous Path for Current Flow. Dimensions of the Inner Loop of the Micro-SQUID Are 0.5 μm x 1.5 μm and Dayem Bridges Are Approximately 250 nm Wide and 500 nm in Length. The Thickness of the Film Is about 90 nm of Tin and 9 nm of Germanium.

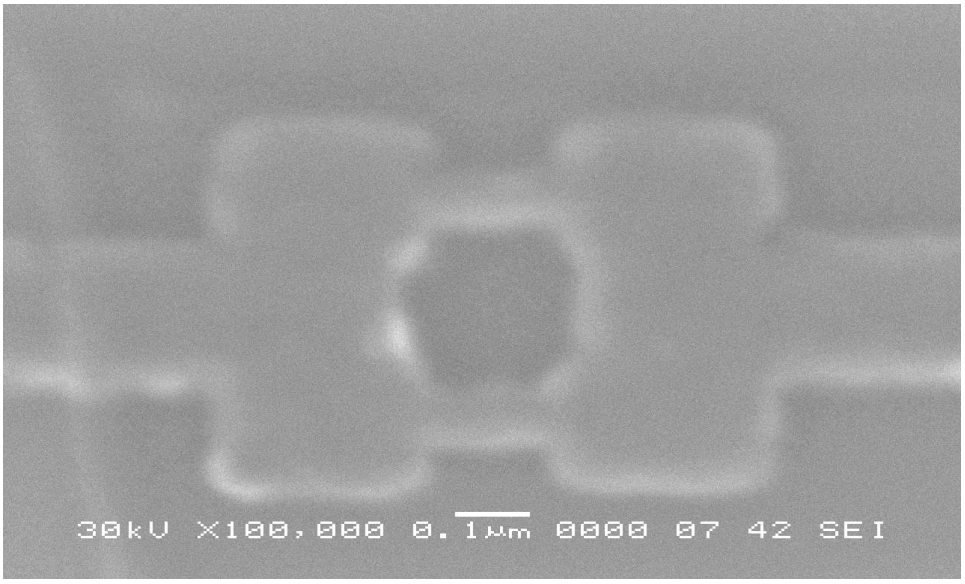

Fig. 76. Aluminum Nano-Micro-SQUIDs with Dimensions of the Inner Loop of the Micro-SQUID Are 0.15 μm x 0.20 μm and Dayem Bridges Are Approximately 40 nm - 43 nm Wide and 125 nm in Length. (Longer Exposure). Thickness of These Micro-SQUIDs Varied Between 20 nm to 50 nm.

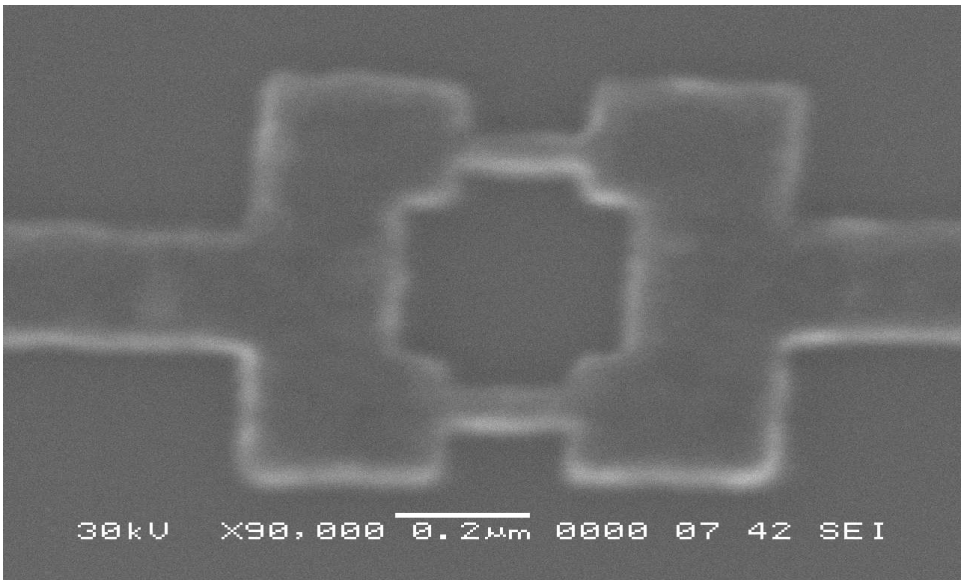

Fig. 77. Aluminum Nano-Micro-SQUIDs with Dimensions of the Inner Loop of the Micro-SQUID Are 0.27 μm x 0.30 μm and Dayem Bridges are Approximately 39 nm - 43 nm Wide and 175 nm in Length. (Longer Exposure). Thickness of These Micro-SQUIDs Varied Between 20 nm to 50 nm.

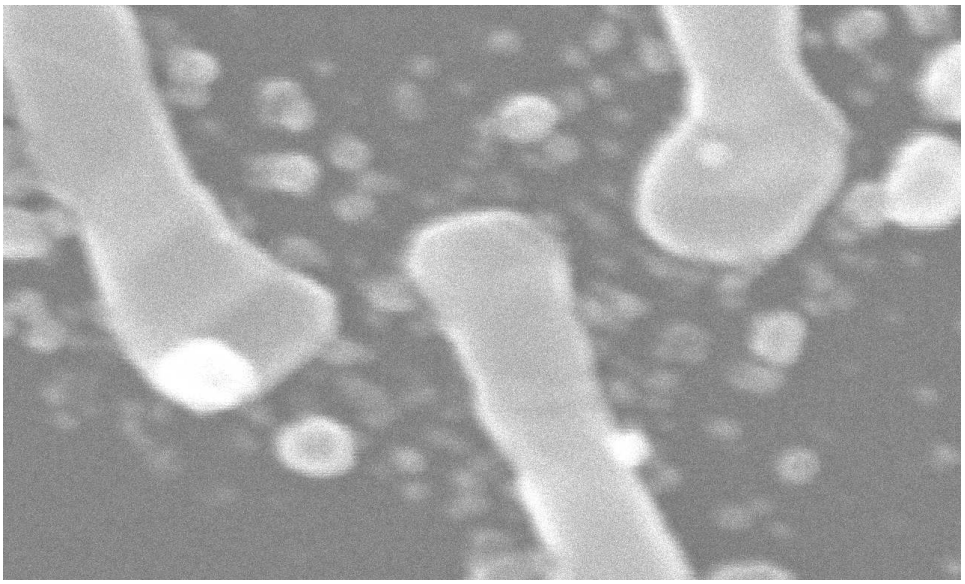

Fig. 78. Enlarged View of Pb Micro-SQUIDs after Thermal Evaporation Process (No Junctions). Thin Film of Pb Micro-SQUID Was Found to Be Non-Continuous. Dimensions of the Inner Loop of the Micro-SQUID Are 1.0 μm x 1.0 μm and Dayem Bridges Are Approximately 50 nm Wide and 250 nm in Length. The Thickness of the Film Is about 50 nm.

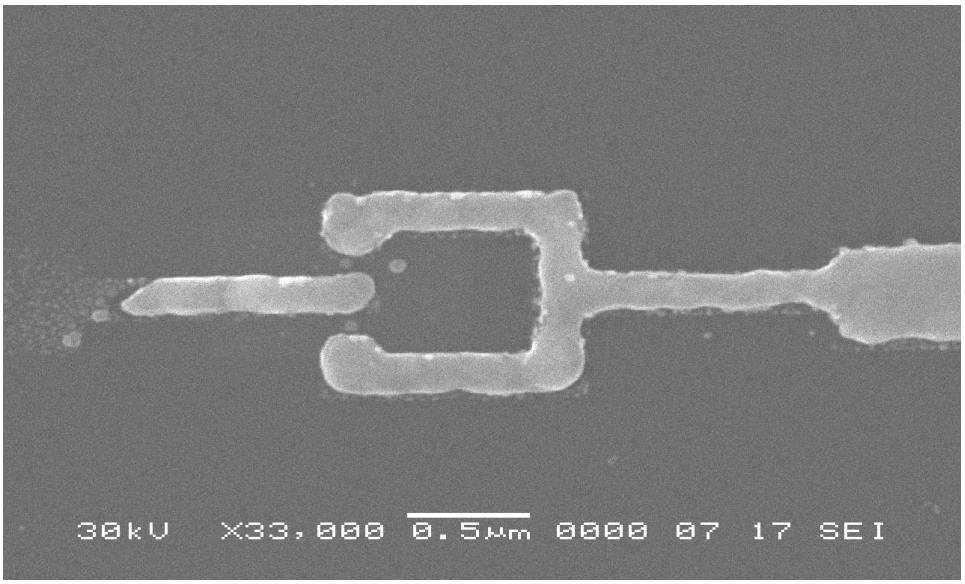

Fig. 79. Defects/Breaks of Leads Common in Pb Lift Off Process. Thin Film of Pb Micro-SQUID Was Found to Be Non-Continuous. Dimensions of the Inner Loop of the Micro-SQUID Are 1.0 μ m x 1.0 μ m and Dayem Bridges Are Approximately 50 nm Wide and 250 nm in Length. The Thickness of the Film Is about 50 nm.

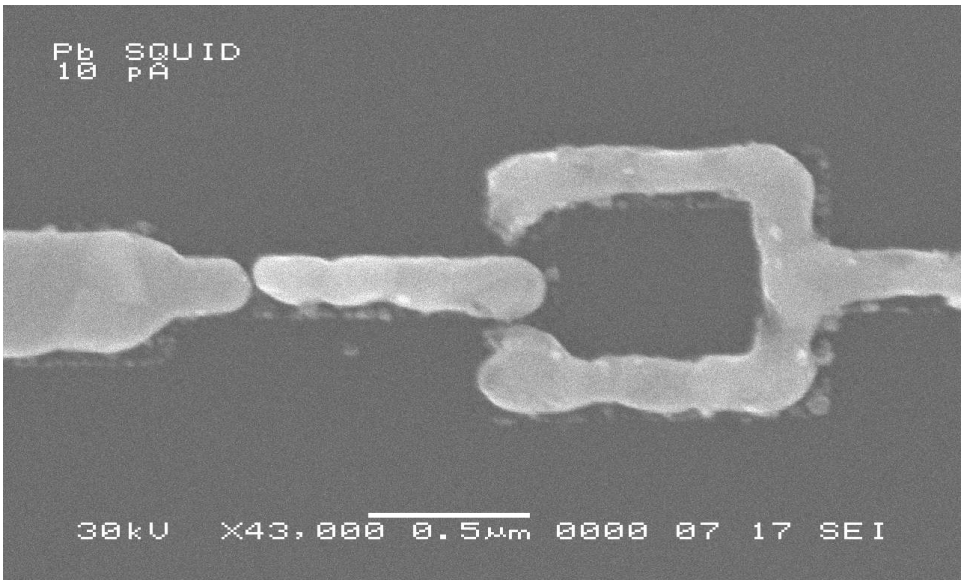

Fig. 80. Pb Thin Film Did Not Adhere Well to Silicon Surface. Thin Film of Pb Micro-SQUID Was Found to be Non-Continuous. Dimensions of the Inner Loop of the Micro-SQUID Are 1.0 μ m x 1.0 μ m and Dayem Bridges Are Approximately 50 nm wide and 250 nm in length. The Thickness of the Film Is about 50 nm. The Image also Shows the Electron Beam Current Used of 10 pA. Current Values between 8pA and 10 pA are Common for Micro-SQUID Development in this Dissertation.

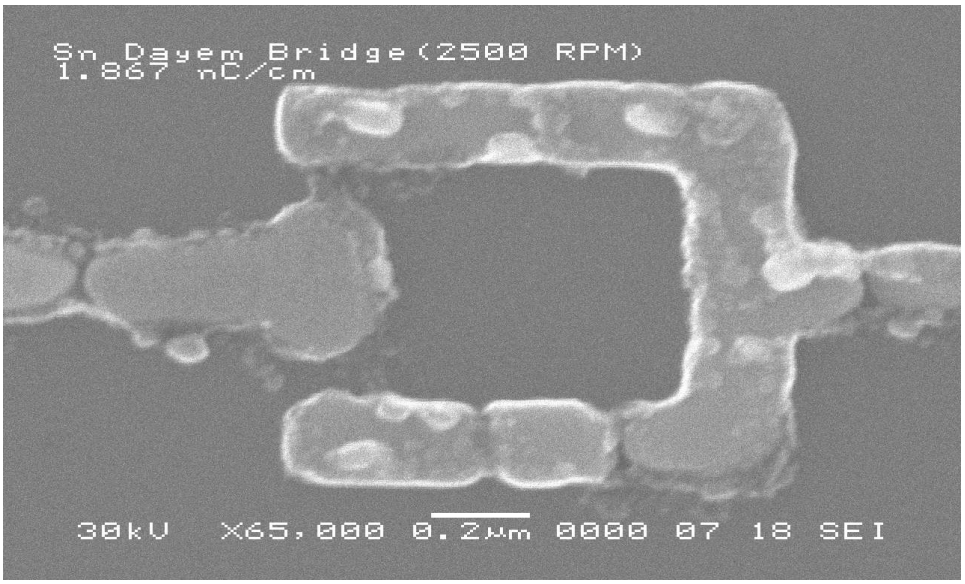

Fig. 81. Dosage level (Amount of Current Supplied Per Length) for Junctions Increased to Investigate Effect on Bridge Creation. Dimensions of the Inner Loop of the Micro-SQUID Are 1.0 μ m x 1.0 μ m and Dayem Bridges are Approximately 50 nm Wide and 250 nm in Length. The Thickness of the Film Is about 50 nm of Tin. The Image Also Shows the Spin Speed of 2500 RPM for the PMMA and That a Electron Beam Line Dosage of 1.867 $\frac{nC}{cm}$ was Used to Create the Dayem Bridges.

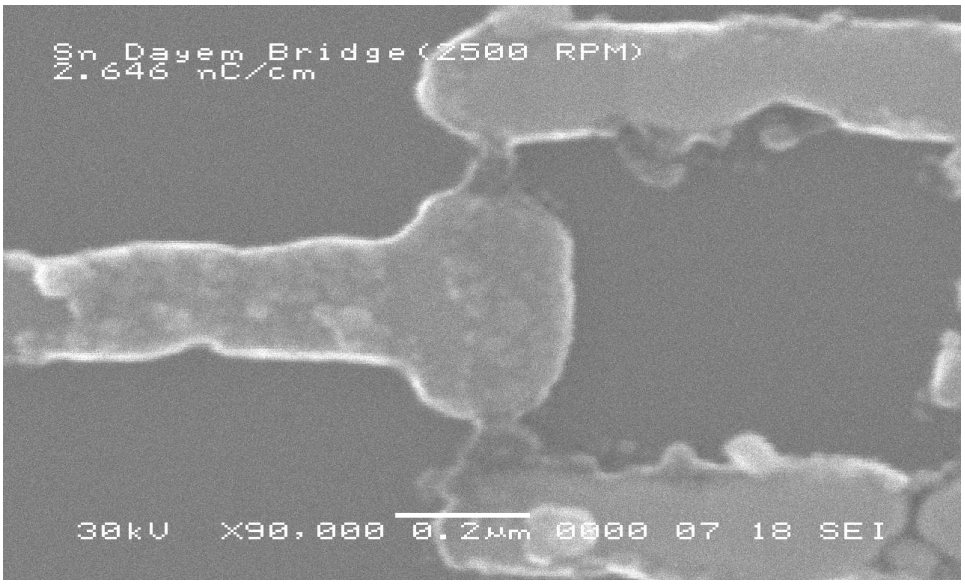

Fig. 82. An Increase in Dosage Level Showed Better Junction Formation but Films Still Not Continuous. Dimensions of the Inner Loop of the Micro-SQUID Are 1.0 μm x 1.0 μm and Dayem Bridges Are Approximately 50 nm Wide and 250 nm in Length. The Thickness of the Film Is about 50 nm of Tin. The Image Also Shows the Spin Speed of 2500 RPM for the PMMA and That a Electron Beam Line Dosage of 2.646 $\frac{nC}{cm}$ Was Used to Create the Dayem Bridges.

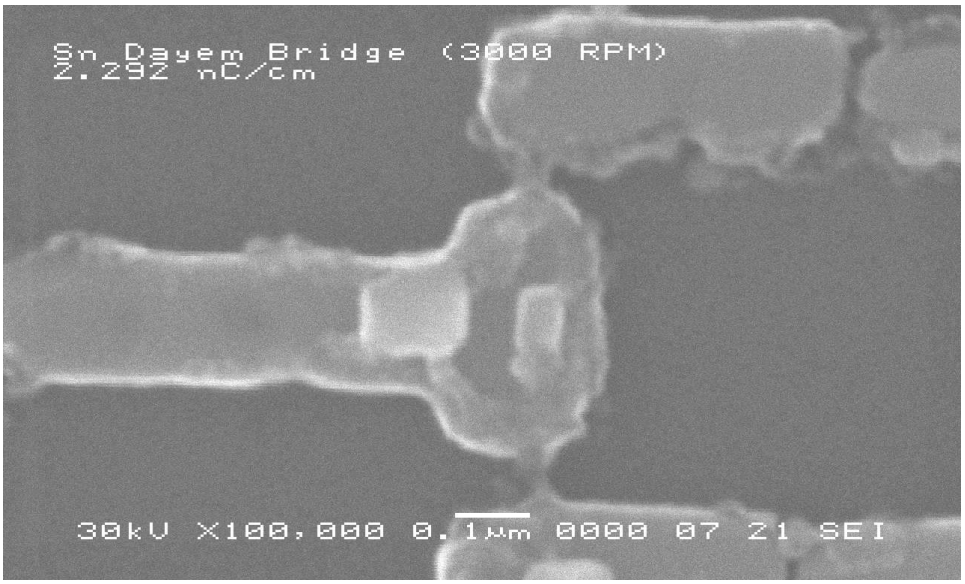

Fig. 83. Further Increases in Dosage Levels Could Not Produce Reliable Bridges. Dimensions of the Inner Loop of the Micro-SQUID Are 1.0 μm x 1.0 μm and Dayem Bridges Are Approximately 50 nm wide and 250 nm in Length. The Thickness of the Film Is about 50 nm of Tin. The Image Also Shows the Spin Speed of 2500 RPM for the PMMA and That a Electron Beam Line Dosage of 2.292 $\frac{nC}{cm}$ was Used to Create the Dayem Bridges.

APPENDIX D

ELECTRON BEAM LITHOGRAPHY (EBL) PROCEDURES FOR DEBEN LASER STAGE

1. Sample Preparation
   (a) Turn on hot plates
      i. 200 C for pre-baking (just for drying Silicon wafer after rinsing)
      ii. 165 C for post-baking (after spin coating of PMMA)
   (b) Cut wafers with carbide scribe
      i. Sample is usually 1 cm x 1 cm
      ii. Use a maximum of 2 cm x 2 cm for samples on top clip mount
   (c) Clean wafers
      i. Sonicate in acetone 2-5 min.
      ii. Rinse with acetone, then with isopropyl alcohol, bake @ 200C
   (d) Coat wafers
      i. Turn on pump and flip switch above spin coater
      ii. Place a few drops of resist (e.g. PMMA) on wafer
      iii. Spin @ 4000 rpm, for about 50 secs, accel/decel = 1 sec
      iv. Bake at 160C for 90 sec
      v. Make a small reference scratch in resist at top edge of wafer
      vi. Turn off pump and wipe off all excess PMMA on chuck with acetone.
      vii. Change gloves before using EBL System (PMMA harmful to body)

2. Loading Sample

   (a) VENT chamber (click on Sample ICON on top bar of SEM Menu)

      i. Light should be blinking orange on SEM when venting

      ii. Unload when light is solid orange

   (b) Exchange sample

      i. Use CAUTION when operating the SEM.

      ii. Unload/Load sample stage with gloved hands gently and carefully.

      iii. DO NOT apply too much force to stage!!! This may break stage motor.

      iv. Attach sample to clips on the top mount next to faraday and gold standard.

   (c) Evacuate chamber

      i. Light on SEM should be blinking green when pumping down

      ii. HT Icon is grey and should say WAIT

      iii. Wait until system beeps (5.5 min., blue HT Ready button activates)

      iv. Wait a minimum of 10 more minutes before proceeding (Caution: the timer is magnetic! DO NOT leave on SEM Table)

3. Scanning Electron Microscope Optimization

   (a) Turn on HT Ready(a neon green light when button is pressed)

   (b) Make sure BEAM STATUS is ON (Deben Beam Blanker Read Out)

   (c) Turn on Piccoammeter (Keithly Multimeter)

      i. Press ZCHK (This should take it out of the zeroed position)

      ii. Press Average (stabilizes current read out)

iii. Click on Gun ICON on SEM Menu at Top of screen.

A. Increase LOAD CURRENT (L. C.) by adjusting the bar in the white region slowly (one click per second) until its just below the middle mark (located in the middle of the white region)

B. Note: One CLICK per second is the usual speed for increasing the current.

(d) Check if Scan Rotation is set at 8.3 (Located in Tools Menu)

i. Tool → Scan Rotation → 8.3

ii. This value corrects the rotation offset by the stage.

(e) Check if Auto Focus Tracer is OFF (Located in Tools Menu)

i. Tools → Auto Focus Tracer → Uncheck Box

ii. Working Distance = 7mm (usually starts out at 8mm when focusing)

iii. Auto Focus Tracer can affect working distance

(f) Saturation of Filament in Faraday Cup (Aperture)

i. Move Stage so that Faraday Cup (round foil with hole = aperture) is in view.

ii. Increase magnification so that the beam is completely enclosed in cup.

iii. Saturation = 1/4 (change in steepest slope) pA

iv. Find steepest slope by bringing up load current (L.C.) slowly

v. Set current value for optimization (i.e. lowest on pattern) by adjusting the SPOT SIZE

vi. Use same current in gun alignment

(g) Gun Alignment (Gun ICON window is open)on Faraday Cup

i. Set TILT(X,Y) by clicking in white part of bar

ii. Current values should be symmetric about maximum

iii. One click to the left of max = one click to right of max

iv. Current maximized is the same as used in saturation

v. Record Current Values and their corresponding Spot Size values necessary to write your pattern.

(h) Gold Standard (100,000X - 150,000X) Optimization

i. Set Focus, clear objective lens using Lens Reset

ii. In Tools Menu at top of screen go to → Tools → Lens Reset

iii. Repeat in range 100,000X - 150, 000X a few times until Lens Reset no longer affects focus.

iv. Picture should be similar to the one viewed before reset.

v. Set Stigmatism

A. Adjust Stigma X and Stigma Y controls (located at top of viewing screen)

B. Clearing condenser lens is optional. This is located in the Tools Menu as Stigma Reset.

C. In Top Menu go to → Tools → Stigma Reset

(i) PRESS WOBB ICON on top of screen to enable wobbler.

i. Set Wobble using nobs on column (careful!)

ii. Vertical or Y Adjustment: Longer Knob

iii. Horizontal or X Adjustment: Shorter Knob

(j) Check Focus and Stigmatism at 200,000X and adjust if necessary

(k) Do not change Astigmatism (same as Stigmatism) after optimization is complete.

4. Sample Optimization

   (a) Focus on scratch on sample

      i. Focus on lower end of the scratch at highest magnification possible (must be over 20,000X to create a good contamination spot)

      ii. Optional: Click SCAN 3 or SCAN 4 and see if image shifts, if so re-optimize.

   (b) Make a contamination spot for fine feature focusing (at 300,000X)

      i. Turn BEAM STATUS to OFF

      ii. Move 100m - 200m (0.10mm - 0.20mm) below scratch

         A. Use Deben Stage controller to move below scratch:

         B. Press →go rel→

         C. At the GoTo XY Prompt, Enter 0 0.20 for the X and Y values respectively.

         D. Note: This is dependent on how your scratch is aligned. You may want to move in to the right of your scratch if you mounted the sample where the scratch is at the side. Therefore, at the GoTo XY Prompt, Enter 0.20 0 for the X and Y values respectively.

         E. See Laser Stage Operation for more details.

         F. Note: Making a spot is optional, not necessary for large patterns.

      iii. Press DAC (0, 0) in the NPGS Custom Command window (EBL Computer) to set the origin for the spot at the current point.

      iv. Flip the blue SEM/NPGS switch to NPGS to write the spot.

         A. Note: The blue switch has a lock on it to prevent it from being knocked into SEM mode accidentally. Pull switch up and over to

the NPGS side to switch into NPGS mode.

B. Turn BEAM STATUS to ON and watch for a drop in current.

C. Note: You may not get a drop in current if you did not focus above 20,000X

D. Focus on spot until it is clearly defined around the edges and there is a dark area in the middle.

E. Repeat again for confirmation (write another contamination spot below the first)

v. Flip the blue SEM/NPGS switch to SEM to observe image

vi. Optional: Turn BEAM to OFF and repeat closer to pattern

5. Pattern Writing

(a) Turn BEAM STATUS (on deben beam blanking controller) to OFF.

(b) Set to SCAN 3 to reduce noise effects.

(c) Move 100m - 200m (0.100mm - 0.200mm) or more below scratch.

(d) Flip the Blue SEM/NPGS switch to NPGS to write pattern.

(e) Make sure you have moved clear of location where you wrote spot

(f) In the NPGS Custom Command Window (on EBL computer) PRESS BEAM OFF

(g) Turn BEAM STATUS to BLANK

(h) Limit vibrations and noise before and during writing.

(i) Under NPGS Commands → PRESS →Process Run File

(j) Follow instructions on screen to write the Pattern, NPGS should indicate the current values and magnification to use.

(k) SET magnification and spot size to correspond to ones indicated on screen.

(l) PRESS space bar to WRITE

(m) At the end of the writing the computer will prompt you to repeat pattern. PRESS →n→ here. You DO NOT want to overwrite your pattern.

(n) Turn the beam blanker, Beam Status to OFF, and move stage off sample if all writing on sample is complete.

i. The EXCH button on the laser stage control panel will move the laser stage an absolute coordinate distance (0, 0)

ii. PRESS →exch→ on the control panel and the display will prompt to move to the exchange location. Press ENTER to move to this location.

iii. Note: You may want to use an absolute coordinate movement in the X direction to move to the edge of the sample that is closest to the faraday cup, before you press exch.

(o) Flip the Blue SEM/NPGS switch to SEM to return to normal state.

6. Retrieving Sample after Pattern Writing

(a) Turn down filament current slowly to lowest position (one click a second)

(b) Move one click per second until load current (L.C.) reaches 26A

(c) Turn off HT (neon green light) and wait 10 minutes before venting.

(d) Magnification = 300,000X ; Spot Size = 25; Accelerating Voltage = 30kV

(e) PRESS ZCHK on Piccoammeter the turn OFF power

(f) Continue to WAIT until the 10 minutes is up.

(g) VENT and retrieve sample gently! (USE GLOVES!)

(h) EVACUATE (keep chamber under vacuum when not in use)

7. Development

   (a) Place sample in beaker filled with developer

   (b) Developer is MIBK:IPA in a 1:3 ratio

   (c) Develop for 60-70 seconds (most samples require only 60 seconds)

   (d) Rinse in Isopropyl Alcohol (Isopropanol), and then dry with Nitrogen gun.

8. System Identification

   (a) SEM Microscope: JEOL JSM 6460

   (b) Pattern Writing Software: NPGS (Nanometer Pattern Generation Software)

APPENDIX E

EVAPORATION PROCEDURES

1. Vent chamber (release vacuum pressure) by open air release valve.
2. Note: Turning valve in the anti-clockwise direction will open the valve and clockwise will close the valve.
3. Mount sample by removing the sample holder from the chamber by loosening the screw that keeps it stationary.
4. Use double sided tape to stick the sample to holder.
5. Attach baskets containing the metals for evaporation to the voltage supply.
6. Place shield between baskets to prevent metal contamination during evaporation.
7. Pump down the chamber
   (a) Close the air release valve
   (b) Close the fore-line valve
   (c) Open the roughing valve
   (d) Monitor pressure with thermocouple (TC) gauge by turning pressure dial to TC1.
8. Close roughing pump valve when it gets to 0.2 Torr to prevent vaporization of oil (oil flowing back into the chamber)

9. Open fore-line valve

10. Fill the Liquid Nitrogen (LN_2) cold trap and wait a few minutes before opening the isolation value (isolates or connects the diffusion pump to the system). This will trap any stray oil vapor that may be floating close to the chamber.

11. Open isolation valve

    (a) Turn presssure dial to thermocouple (TC) gauge to TC2 and what for rise in pressure.

    (b) Do not let pressure go above 0.2 Torr, this may cause oil vapor to back stream into system. The diffusion pump is backed by a mechanical pump through the fore-line valve.

    (c) Wait about 10 minutes before turning on ion gauge. The pressure will drop to a value in the 10^{-4} Torr range and the ion gauge will illuminate at this point. The ion gauge monitor will be used to read the pressure down to the system's base pressure about 2 x 10^{-6} Torr.

    (d) Re-fill the LN_2 cold trap every 15 minutes until the pressure gets down to 5 x 10^{-6} Torr. This could take as long as 90 minutes to 2 hours.

12. Evaporate metal

    (a) Note: Make sure the power connector is attached to the adhesion layer basket, then attached connector to other basket for the second evaporation.

    (b) Turn ON the filament supply switch on the evaporator panel and turn the dial to about 40 (scale ranges from 0 to 100)

    (c) Turn on the frequency monitor and the power supply for the quartz crystal micro-balance(QCM).

(d) Turn the dial on the panel to about 40 (scale ranges from 0 to 100)

(e) Wait until the frequency drops at a steady rate on the frequency monitor before opening shutter.

(f) The required thickness can be found by monitoring the change in frequency Δf and using the formula for the thickness ratio $\rho = \frac{\Delta f}{t}$, where f is the frequency (Hz) and t (Å)is the thicknesss.

(g) Once the desired thickness is reached, turn down the dial for the filament supply and turn OFF the filament supply switch.

(h) Close the isolation valve and wait 15 minutes before venting the chamber.

(i) Return chamber to vacuum state.

13. Lift off process

(a) Immerse metalized sample in beaker filled with acetone.

(b) Wait until the metal surface begins to peel off (into a thin foil) and wash the foil off the surface with acetone.

(c) Repeat process until the outline of the pattern is the only film left on the surface.

(d) Inspect the pattern under a microscope and sonicate sample if there are any unwanted foil pieces still attached to the pattern.

(e) If pattern is fully intact attached by gold wires to the low temperature measurement system.

APPENDIX F

DILUTION REFRIGERATOR COOL DOWN PROCEDURES

This appendix provides a guideline of protocols that was used for successful operation of the dilution refrigerator used in this dissertation.

1. Initial Checks

   (a) Check all electrical leads.

   (b) Put up radiation shield.

   (c) Recheck all electrical leads.

   (d) Leak check the vacuum can.

   (e) Pump on vacuum can for about one hour with diffusion pump.

   (f) Pump with the diffusion on both sides of the circulation system (labeled low side and high side) for approximately one hour.

   (g) Hang superconducting magnet.

   (h) Add V-sense and heater leads to magnet.

   (i) Attach superconducting level meters (labeled high and low).

   (j) Attach heater to bottom of vacuum can.

   (k) Attach liquid helium (LHe) fill line extension.

   (l) Tape all hanging leads to vacuum can.

   (m) Put up dewar and tighten bolts.

   (n) Open 1K Pot fill valve.

(o) Pump out dewar for at least 30 minutes.

(p) When pressure is below 1 psi in dewar, open 1K pot pumping line.

2. Pre-Cool Protocol

(a) Stop pumping on circulation system and vacuum can.

(b) Add ^{3}He exchange gas to vacuum can.

i. Close off diffusion pump valve.

ii. Leave vacuum can open.

(c) Fill the circulation system LN_2 cold trap.

(d) Perform a circulation check of the system.

i. Make sure that the pumping side (low side) of the circulation system is less than 1 milli-Torr.

ii. Put mixture on return side (high side) of circulation system. Circulate through cold trap before opening last valve to circulation system.

iii. Measure rise time for pressure on pumping side of circulation system.

(e) Close valve to 1K Pot pump.

(f) Close 1k Pot fill valve.

(g) Fill dewar with N_2 gas.

(h) Pressurize 1K pot with 16 psi of He gas.

(i) Transfer liquid nitrogen LN_2.

(j) Measure the resistance of the inside and outside C thermometers (labeled C_{IN} and C_{OUT}) show appropriate LN_2 values.

(k) Perform second circulation check to test if the circulation time has improved.

3. Cool Down Protocol

   (a) Back transfer LN_2.

      i. Make sure transfer tube is fully seated in extension.

      ii. Pressurize the dewar with N_2 gas to push out liquid from bottom of dewar.

   (b) Pump out dewar until pressure reaches -30 mmHg.

   (c) Back fill dewar with He gas.

   (d) Transfer LHe until level meter read approximately 70%.

   (e) Pump out vacuum can with diffusion pump.

   (f) Open 1K pot pumping line and pump out 1K pot.

   (g) Open 1K pot fill valve. The pressure should rise then stop.

   (h) Close 1K fill valve when pressure rises again.

      i. Pressure should go down and the vapor pressure will be very low.

      ii. Value of 1K pot resistor will be about 2300 Ω.

   (i) Add mixture to pumping side of circulation system and allow it to condense inside dewar.

   (j) When pressure on pumping side has stabilized, open return side valve and begin pumping to start circulation.

   (k) Once the temperature is below 600 mK, turn on the still heater (0.5 - 1.0 mA)to improve cooling power.

4. Warming Up Protocol

   (a) Close off line that leads to dewar on the return side of the circulation system.

(b) Allow mixture to collect in tanks B (480 Torr) and C (150 Torr).

(c) Close tanks once the Tanks have reached their original pressure.

(d) Pump out the circulation line on pumping side until it has reached its base pressure and close valve once this is done.

(e) Pump out return side of all mixture, closing off the left side of the LN_2 Trap and dumping all mixture on the left side of the trap.

(f) Pump out the dewar and refill 1K pot with helium gas.

(g) Fill dewar with nitrogen gas to increase temperature in dewar.s

5. Electrical Measurement Protocols

(a) Resistance measurements are taken using a standard four wire AC lock-in technique.

(b) At the start of each measurement, adjusted the signal so that the out of phase signal is minimized.

(c) Generate an output voltage of 1.0 V for a frequency of 7.0 Hz through a 10 kΩ resistor below the sample's superconducting temperature. This will give a current output of 100 μA so that critical current oscillations can be observed.

(d) Measure the voltage drop across the sample by attaching the voltage leads to a voltage pre-amplifier which is connected to the multimeter/scanner interface.

(e) Disconnect current and voltage leads of the sample from lock-in and attach the leads to the V+, V-, I+, I- connections of the critical current box.

(f) Attach the signal generating output voltage to I_{SWP} of the AC lock-in to the critical current box and an oscilloscope using a "T" connector.

(g) Attach the sampling voltage and the sampling current ports on the critical current box to an oscilloscope for viewing.

(h) Attach the voltage across the sample port on the critical current box to the oscilloscope. This will be eventually connected along with the sampling current to two multimeters for capturing the data.

(i) Set the mode on the oscilloscope to function vs. time outputs, e.g., V vs t, I vs T etc... for each channel connected from the critical current box.

(j) Increase the current across the sample from zero until a transition is seen on the oscilloscope (V vs t).

(k) Set the sampling voltage value to correspond to the value of the lowest edge of the transition.

(l) Once sampling voltage is set, connect the voltage across the sample (a "T" BNC connection with the multimeter and the oscilloscope will make this easier) and the sampling current to multimeters to record data seen on oscilloscope.

(m) The oscillating critical current values are recorded once the magnet voltage supply is increased.

APPENDIX G

PHYSICAL PROPERTY MEASUREMENT SYSTEM PROCEDURES

This appendix provides a guideline of protocols that were used for successful operation of the physical property measurement system (PPMS) in this dissertation.

1. Initial Preparation

   (a) Attach puck unto user bridge (device used to check electrical continuity).

   (b) Attach 4 gold wires to each channel (Note: there are 3 channels available) of the puck by soldering indium unto the channel's contact pads labeled I+, V+, V-, I-.

   (c) Attach the 4 gold wires to the sample leads by pressing indium unto the gold wire and the sample.

   (d) Check electrical continuity of the 4 wires on the user bridge with a multimeter (2 wire measurements).

   (e) Vent System by pressing "Vent" on PPMS graphical user interface.

   (f) Use extraction tool to mount puck into the PPMS.

   (g) Rotate puck with extraction tool until it drops into slot (grove on puck is used for proper alignment with system).

   (h) Press puck gently into position and then remove extraction tool.

   (i) Check resistivity, by activating the resistivity option and selecting channel.

   (j) Evacuate chamber by pressing "purge/seal", system should begin flushing process and read a pressure of about 1.0 Torr when pumped out.

(k) Press "seal" (seals the environment)

(l) Re-check resistivity, by selecting the channel for measurement using the resistivity option.

2. Liquid Helium Fill Protocol

(a) Attach the helium gas line with balloon to the liquid helium (LHe) dewar.

(b) Insert transfer tube into the liquid helium (LHe) dewar, until cold gas is flowing out the other end, then insert the other end into the PPMS dewar fill line.

(c) Open the graphical user interface for the helium fill line (go to Utilities → helium fill) on the PPMS computer.

(d) A window will open giving the LHe level percentage in the dewar and the fill rate.

(e) Fill the PPMS dewar by forcing helium gas into LHe dewar by using the balloon attached to the dewar. Fill rate should be between 4 - 5 %/min for optimum performance.

(f) Dewar should be filled in about 15 to 20 minutes from a helium level of 0%.

3. Electrical Measurement Protocols

(a) Measurements are taken in two modes, the resistivity mode or the AC transport mode.

(b) To select an option go to the Utilities → option → Activate.

(c) Mode 1 : The resistivity option

i. Go to Utilities → Resistivity → Activate.

ii. This will open up the bridge channel box for channel selection.

iii. Once the channel or channels are selected you can then proceed to select the data fields that you would like to take measurements with, such as temperature, magnetic field, excitation, voltage etc.

iv. Click on the graphical user interface x axis and y axis to show the relationship between any of the data fields selected in the channel box.

v. To deactivate option go to Utilities → Resistivity → Deactivate.

(d) Mode 2 : The AC transport option

i. Go to Utilities → AC transport → Activate.

ii. This will open up the AC transport graphical user interface.

iii. Note: There are only two channels available for measurement in the AC transport measurement option and Channel 3 is the only channel from the resistivity puck that is compatible with this user interface, this will correspond with the Channel 2 settings in this option.

iv. Select the data fields that you would like to take measurements with, such as resistivity, temperature, critical current, magnetic field, excitation, voltage etc.

v. Click on the graphical user interface x axis and y axis to show the relationship between any of the data fields selected in the channel box.

vi. To deactivate option go to Utilities → AC transport → Deactivate.

VITA

Arlene Celeste Ford was born in Antigua in the West Indies. She is the daughter of Ethlyn Thomas and Keith Ford. Arlene graduated with a Bachelor's degree from Midwestern State University in mathematics and physics in 2001. After receiving her degree from Midwestern State University she joined the Physics graduate program at Texas A&M University, where she received her Master of Science in physics in August 2005 and her Doctor of Philosophy degree in May 2010. She can be contacted at aford@tamu.edu or at the Department of Physics, Texas A&M University, TAMU 4242, College Station, TX 77843-4242